BOSTON UNIVERSITY

GRADUATE SCHOOL OF ARTS AND SCIENCES

DISSERTATION

# ADVANCES IN OPTICAL TRAPPING BEYOND BIOPHYSICS: COMBINING FORCE AND OPTICAL SPECTROSCOPIES UNDER DIVERSE CHEMICAL CONDITIONS

by

**DANIEL JACKSON**

B.S., Union College, 2017

Submitted in partial fulfillment of the
requirements for the degree of
Doctor of Philosophy
2024

© 2024 by

Daniel Jackson

All rights reserved

Approved by

First Reader ______________________________

Maria Kamenetska

Professor of Chemistry

Professor of Physics

Professor of Material Science

Second Reader ______________________________

Björn Reinhard

Professor of Chemistry

# ACKNOWLEDGMENTS

I would like to thank my advisor, Masha Kamenetska. Thank you for taking me on as your first student, teaching me so many things, and learning even more things along with me through the last 7 years. Being placed in your lab on my first day was truly one of the luckiest moments in my life. I have found something I truly love to study and learned things I never could have imagined on my own. I greatly appreciate all of the opportunities that I was presented with while working with you and I think it has been a true privilege to study in your lab.

Thank you to my dissertation committee, Prof. Björn Reinhard, Prof. Xi Ling, and Prof. Larry Ziegler for your questions and insightful comments throughout my various projects.

I want to thank everyone that I have had the honor of working with during my time in the Kamenetska Lab: Alona Maslennykov, Alexander Krasnansky, Andrea Rustad, Dr. Brent Lawson, Brian Dawes, Connor Uzzo, Faisal Halabeya, Favian Liu, Freddy Luna, Hanil Chung, Dr. Hannah Skipper, Hiba Pediyakal, Maitreya Rose, Nicholas Miller, Payton Harvill, Regal Jiang, Dr. Xiaoyun Pan, Zelin Miao.

And lastly, I want to thank my family and friends for being there through every step of this process to act as listening ears and shoulders to lean on. Without all of your support I would not have been able to accomplish a single thing during my time in graduate school. I look forward to sharing the next adventure with you.

# ADVANCES IN OPTICAL TRAPPING BEYOND BIOPHYSICS: COMBINING FORCE AND OPTICAL SPECTROSCOPIES UNDER DIVERSE CHEMICAL CONDITIONS

Boston University Graduate School of Arts and Sciences, 2024

Major Professor: Maria Kamenetska, Assistant Professor of Chemistry,

Physics, and Materials Science and Engineering

## ABSTRACT

Optical tweezers (OT) have revolutionized the study of molecular biology as recognized in 2018 by the Nobel prize in Physics to Arthur Ashkin, the inventor of the technique. OT allow selective single particle manipulation and control in solution at the focus of an optical microscope and in combination with other optical spectroscopies. These techniques have been used to apply forces to single molecules in order to measure dynamics and energetics of protein folding, motor protein translocation and RNA structural transitions, to name just a few. Yet, the capacity of OT for molecular mechanistic studies for *chemistry and materials* applications is vastly underexplored. The subject of this thesis is to develop approaches for expanding the capability of OT outside of the biological domain.

In Chapter 2 we discuss address one of the main obstacles to applying OT to study synthetic molecular mechanisms. Standard OT probes made from silica or polystyrene are incompatible with trapping in organic solvents for solution phase chemistry or with force-detected absorption spectroscopies. Here, we demonstrate optical trapping of gold nanoparticles in both aqueous and organic conditions using a custom OT and darkfield

instrument which can uniquely measure force and scattering spectra of single gold nanoparticles (Au NPs) simultaneously. Our work reveals that standard models of trapping developed for aqueous conditions cannot account for the trends observed in different media here. We determine that higher pushing forces mitigate the increase in trapping force in higher index organic solvents and lead to axial displacement of the particle which can be controlled through trap intensity. This work develops a new model framework incorporating axial forces for understanding nanoparticle dynamics in an optical trap. These results establish the combined darkfield OT with Au NPs as an effective OT probe for single molecule and single particle spectroscopy experiments, with three-dimensional nanoscale control over NP location.

Chapter 3 demonstrates an all-optical method using an optical tweezer to perform chemistry on a single particle in solution. Specifically, we controllably and selectively grow high quality zeolitic imidazolate framework (ZIF) nanoshells on the surface of a single gold nanoparticle (AuNPs) and monitor the growth via darkfield spectroscopy. Our single particle approach allows us to localize an individual NP within a microscope slide chamber containing ZIF precursors at the focus of an optical microscope and initiate growth through localized heating without affecting the bulk system. Darkfield spectroscopy is used to characterize changes to the localized surface plasmon resonance (LSPR) of the AuNP resulting from refractive index changes as the ZIF crystal grows on the surface. We show that the procedure can be generalized to grow various types of ZIF crystals, such as ZIF-8, ZIF-11, and a previously undocumented ZIF variety. Utilizing both computational models and experimental methods, we identify the thickness of ZIF layers to be self-limiting to ~50 nm or less, depending on the trapping laser power. Critically, the refractive index of the shells here was found to be above 1.6, indicating the formation of high-density crystals, previously accessible only through slow atomic layer deposition and not through a bulk heating process. The single particle method developed here opens the door for bottom-up controllable growth of custom nanostructures with tunable optical properties.

Chapter 4 of the thesis introduces an approach to studying and controlling gold nanoparticle (AuNP) dimers suspended in solution using optical trapping. The primary objective is to control inter-particle separation in AuNP dimers using OT and to leverage the plasmon scattering resonance signature to measure it in situ. This functionality is crucial for applications in nanophotonics, nanoelectronics, and biosensing, where accurate distance control between nanoparticles can lead to the development of highly sensitive sensors and devices. We use the custom optical trapping instrument described in Chapter 1 that combines an inverted optical microscope with darkfield (DF) illumination, allowing for the manipulation and imaging of metallic nanoparticles. We show that the dimer long axis aligns with the trapping laser polarization, allowing for control of dimers in solution. When the long axis of the dimer is parallel to the excitation polarization, the dimer scattering resonance is maximized, enabling more precise spectroscopic analysis. The shifts in dimer wavelengths with changing inter-particle separation are modeled computationally, leading to the development of a plasmon ruler equation for our system, which allows for conversion between optical wavelength shifts and distance. We form dimers using van der Waals sticking between polymer coated AuNPs. We find that dimers formed with distinct

molecular tethers differening distributions of inter-particle distances which depend on molecule length and structure. Furthermore, by tuning the power of the OT laser, we can modulate the temperature at the dimer surface, causing the release of inter-molecular interactions and a gradual separation of the dimer particles. This experiment is the first demonstration of control over dimer geometry in solution. By tracking the evolution of the plasmon spectra during heating and separation, we are able to distinguish between the classical capacitive coupling regime captured by the plasmon ruler relationship and the charge transfer plasmon (CTP) which arises from quantum tunneling in the dimer gap. The methodology established here provides unprecedented control over dimer geometry which can be leveraged for applications in plasmon-driven catalysis, surface-enhanced spectroscopy and charge transfer studies.

# TABLE OF CONTENTS

ACKNOWLEDGMENTS ........ iv

ABSTRACT ........ iv

TABLE OF CONTENTS ........ viii

LIST OF FIGURES ........ xii

LIST OF ABBREVIATIONS ........ xxii

Chapter 1: INTRODUCTION ........ 1

1.1 MOTIVATION ........ 1

1.2 OPTICAL TWEEZER TECHNIQUE ........ 2

1.2.1 RAY OPTICS TRAPPING MECHANISM ........ 3

1.2.2 POINT DIPOLE TRAPPING MECHANISM ........ 3

1.3 PLASMONS ........ 4

1.3.1 SCATTERING AND DIELECTRIC CONSTANTS ........ 5

1.3.2 HEATING NANOPARTICLES ........ 5

1.4 SPECTROSCOPY ........ 6

1.4.1 FORCE SPECTROSCOPY ........ 6

1.4.2 DARKFIELD MICROSCOPY AND SPECTROSCOPY ........ 6

1.4.3 RAMAN SPECTROSCOPY ........ 7

1.5 THESIS OUTLINE ........ 7

Chapter 2: SIMULTANEOUS FORCE AND DARKFIELD MEASUREMENTS REVEAL SOLVENT-DEPENDENT AXIAL CONTROL OF OPTICALLY TRAPPED GOLD NANOPARTICLES ........ 9

2.1 INTRODUCTION ........ 9

2.2 RESULTS AND DISCUSSION ........ 13

2.2.1 Experimental Design and Instrumentation ........ 13

2.2.2 IDENTIFYING A SINGLE PARTICLE USING OT AND DF ........ 16

2.2.3 HEATING MODEL ........ 20

2.2.4 TRAPPING FORCE DERIVATION ........ 29

2.3 CONCLUSION ........ 34

2.4 EXPERIMENTAL ........ 35

Chapter 3: TUNABLE GROWTH OF A SINGLE HIGH-DENSITY ZIF NANOSHELL ON A GOLD NANOPARTICLE ISOLATED IN AN OPTICAL TRAP ........ 38

3.1 INTRODUCTION ........ 38

3.2 RESULTS ........ 40

3.3 GROWTH OF ZIF ........ 42

3.3.1 CHOOSING PRECURSOR CONCENTRATIONS ........ 46

3.4 RAMAN SPECTRA COLLECTION ........ 46

3.5 PLASMON RESONANCE SPECTRA ........ 48

3.6 Loss of Distinct Peak ... 51

3.7 HISTOGRAMS OF CRYSTAL GROWTH ... 53

3.8 HEATING OF GOLD NANOPARTICLES ... 57

3.9 CONCLUSION ... 59

3.10 EXPERIMENTAL ... 60

3.10.1 Materials ... 60

3.11 PROCEDURE ... 61

3.11.1 PREPARATION OF PRECURSOR SOLUTION ... 61

3.11.2 FUNCTIONALIZING AUNPS WITH PVP ... 61

3.11.3 COMBING GOLD AND PRECURSORS ... 62

3.11.4 SAMPLE PREPARATION ... 62

Chapter 4: SINGLE ENTITY DARK-FIELD AND FORCE SPECTROSCOPY MEASUREMENTS OF NANOPARTICLE DIMERS REVEAL TRANSITIONS FROM THE CLASSICAL TO THE QUANTUM REGIME ... 63

4.1 INTRODUCTION ... 63

4.2 RESULTS AND DISCUSSION ... 64

4.2.1 QUANTIFYING DIMER SEPARATIONS PREPARED USING DISTINCT MOLECULAR LINKERS ... 67

4.2.2 Controlling Dimer Separation Distance through Heating ... 71

4.3 CONCLUSION ........ 74
JOURNAL ABBREVIATIONS ........ 76
REFERENCES ........ 79
CURRICULUM VITAE ........ 97

## LIST OF FIGURES

**Figure 1-1** Basic diagram of a particle displaced from the optical trapping focus. Spring used to illustrate the restoring force back towards center .............................. 2

**Figure 1-2** Illustration of the plasmon resonance of a spherical gold nanoparticle. Green cloud represents the electron cloud oscillating along with the frequency of the incident light wave. ........................................................................... 5

**Figure 2-1** A) Instrument schematic of the custom built optical tweezer and DF microscope used here. B) LSPR scattering spectra of optically trapped 80 nm Au NP in a subset of solvents used here. Black dashed line is a Lorentzian fit for the DMF spectra. Inset: LSPR spectra of a single 80 nm Au NP (dark blue) and two 80 nm Au NP (pale blue) trapped in the OT. The peak in the spectrum shifts towards red and the intensity increases when two particles are trapped. C) DF images of 80 nm gold nanospheres trapped and suspended away from surfaces in different solvent environments. Spectra in (B) were recorded on the same particles as shown in images. ...................................................................... 12

**Figure 2-2** A) Centered raw data output from QPD showing the difference in signal as one 80 nm Au NP enters the trap. B) Histogram of particle displacements (in QPD voltage units) showing the increasing MSD as multiple particles enter the trap. C) Images associated with the shown histogram. From left, empty trap, one particle, two particles, and three particles. Light intensity was reduced for these images to prevent three particle image from saturating the camera. ............ 15

**Figure 2-3** A) Displacements of 80 nm Au NP trapped in the OT (left) and displacement histograms (right) in various solvents. Slow drift has been subtracted from the data. B) PSD of optically trapped 80 nm Au NPs in different solvents determined from displacements in Figure 1D. PSD curves have been smoothed to 10 Hz. Dashed line shows a Lorentzian fit to the DMF data. C) Top plot shows the measured stiffness at 32 mW based against refractive index of the medium. Bottom plot is modelled stiffness at 32 mW of 80 nm Au NP using Equation 2.1. ........................................................................................ 17

**Figure 2-4** Illustration of calculation for total power reaching the particle. Outer edge of laser light is removed from power density calculation due to reflection of light at critical angle at the material boundaries.................................................. 19

**Figure 2-5** Predicted surface temperatures of an 80 nm gold nanoparticle held in an optical trap 200 nm above the focal plane of the laser. ........................................... 24

**Figure 2-6** Measured and calculated viscosities for all solvents used in this experiment. Solid lines represent the viscosities determined based on the measured diffusion values. Dashed lines are the viscosities associated with our calculated temperatures. DMF exceeds its boiling point after 45 mW and so viscosity values are based on an extrapolation from lower temperature viscosities..... 25

**Figure 2-7** (A) Measured stiffness values in the x direction of an optically trapped, 80 nm gold nanoparticle in various solvents as a function of power. Dashed lines represent predicted stiffness based off models for trapping and pushing forces experienced by a particle in an optical trap. B) z direction stiffness values associated with x stiffness values from (A). Inset shows the trend of stiffness against refractive index at 32 mW trapping power C) Calculated trapping force in the transverse plane (top) and the scattering force in the axial direction (bottom). D) Cartoon illustration of particle equilibrium position in the axial direction in various solvents. In water (blue) the particle trapping position remains fixed regardless of power, while in EG50 (black) and DMF (brown) it is displaced towards and away from the focal point respectively................. 26

**Figure 3-1** **A)** Schematic of OT built in an inverted microscope configuration, including DF spectroscopy imaging. Red represents our trapping laser. Gray represents the DF illumination (white light). Green is the input Raman excitation laser (532 nm). Orange is the light scattered back by the nanoparticles. At the objective focus is an optically trapped AuNP coated in a ZIF shell. Insets show a representative plasmon scattering spectra and the associated DF images of the particle. Diagram not to scale. **B)** Mechanism describing encapsulation of optically trapped AuNPs by ZIF-8 to form single-particle, core@shell structures. PVP = polyvinylpyrollidone, 2-Mim = 2-methylimidazole. Diagram not to scale. ........................................................................................ 40

**Figure 3-2** **A**) DF spectra collected following heating of an optically trapped, 80 nm AuNP in ethanol in the presence of ZIF-8 precursors. The gray curve is measured immediately after laser power increase which precipitates heating and the red curve is measured 15 seconds later, with a few intermediate spectra also shown. Gaussian fits to the spectra are plotted in dashed black **B**) Camera images corresponding to the spectra in 2A. **C**) Intensity (green, right axis) and peak wavelength (black, left axis) as extracted from Gaussian fits to the raw spectra plotted against time elapsed since heating onset. Data corresponding to 18 individual AuNP is plotted here and is representative of the full data set collected in ethanol. Data corresponding to curves in 2A is highlighted in orange. ........................................................................................ 42

**Figure 3-3** **A)** Control measurement DF spectra collected following heating of an optically trapped, 80 nm AuNP in the presence of 2-methylimidazole dispersed in ethanol. **B)** Plot of the peak wavelengths (left, back) and associated intensities (right, green) against time. ............................................................................ 44

**Figure 3-4** Plots of a full time sequence for the data presented in Figure 2A and 2C where dark curves represent the initial spectra and red represents the final spectra. Left is the raw data collected by the spectrometer, and the right is the Gaussian fits to those same lines. ....................................................................... 44

**Figure 3-5** Plot of the $Zn^{2+}$ and 2-MIM concentrations used in experiments. Found the best use concentration ratio of the two precursors to be 3:1, Mim:Zn. Green points represent concentrations that yielded steady and reproducible growth of ZIF-8 crystals on the surface of the gold. Yellow points represent concentrations that either resulted in growth that was restrictively slow or had small ZIF-8 crystals form in the solution background. Red represents concentrations where either no growth was observed, or an excessive number of ZIF-8 crystals grew in the background. .................................................. 45

**Figure 3-6** **A)** Control measurement DF spectra collected following heating of an optically trapped, 80 nm AuNP in the presence of in $Zn(NO_3)_2$ ethanol. **B)** Plot of the peak wavelengths (left, back) and associated intensities (right, green) against time. ........................................................................................................ 45

**Figure 3-7** Raman measurement using a 532 nm excitation beam, with a 1 min acquisition time, performed on a single, optically-trapped, 80 nm AuNP in the presence of PVP polymer (green), 2-Mim (blue), $Zn(NO_3)_2$ salt (red), and a ZIF-8 crystal grown on the surface (black). A fully labeled ZIF Raman scattering spectra is presented in **Figure 3-8**....................................................................... 47

**Figure 3-8** Raman spectra of ZIF-8 grown in the optical trap. Peaks identified by comparison to reported values.[5,6] Inset cartoon shows the organic linker, 2-Mim, bound to $Zn^{2+}$ metal ions as would be found in the ZIF-8 crystal. ...... 48

**Figure 3-9** **A)** DF spectra collected following heating of an optically trapped, 80 nm AuNP in the presence of ZIF-8 precursors, 2-methylimidazole and $Zn(NO_3)_2$ in DMF **B)** Plot of the peak wavelengths (left, back) and associated intensities (right, green) against time.......................................................................... 48

**Figure 3-10** **A)** DF spectra collected following heating of an optically trapped, 80 nm AuNP in the presence of ZIF-8 precursors, 2-methylimidazole and $Zn(NO_3)_2$ in DMF exhibiting decreasing intensity. **B)** Plot of the peak wavelengths (left, back) and associated intensities (right, green) against time.......................... 49

**Figure 3-11** **A)** DF spectra collected following heating of an optically trapped, 80 nm AuNP in the presence of ZIF-67 precursors ($Co(NO_3)_2$ and 2-methylimidazole) in ethanol. **B)** Plot of the peak wavelengths (left, back) and associated intensities (right, green) against time. ........................................................ 49

**Figure 3-12 A)** DF spectra collected following heating of an optically trapped, 80 nm AuNP in the presence of $Co(NO_3)_2$ and 4-tertbutylimidazole in water **B)** Plot of the peak wavelengths (left, back) and associated intensities (right, green) against time. ........................................................................................ 49

**Figure 3-13 A)** DF spectra collected following heating of an optically trapped, 80 nm AuNP in the presence of ZIF-8 precursors, 2-methylimidazole and $Zn(NO_3)_2$ in water. **B)** Plot of the peak wavelengths (left, back) and associated intensities (right, green) against time. ............................................................................ 50

**Figure 3-14** Model calculations of the scattering cross section of an 80 nm AuNP in ethanol for different thickness ZIF shells. **A)** Calculation shell with refractive index n=1.58 as listed by Cookney et al. **B)** Calculation shell with refractive index n=1.70 to agree with measured data. **C)** A zoom in of **B** to emphasize the difference in peak shape between thin shell scattering and thick shell scattering. ........................................................................................................... 51

**Figure 3-15 A)** Modelled scattering cross sections for an 80 nm AuNP in ethanol with a ZIF crystal shell. Each curve has a different shell thickness ranging from 0 nm (greenest curve) to 250 nm (reddest curve) for refractive index n=1.58. The black line shows the evolution of the resonance peak as the shell thickness varies. Core@shell particles were modeled using MNPBEM17 toolbox in MATLAB.[107] **B)** The changes in the resonance peak for different ZIF refractive indices and thicknesses. Each point represents the peak location or a given shell thickness and refractive index modelled as in 4A. Dashed black lines show double exponential fits to the data. ................**Error! Bookmark not defined.**

**Figure 3-16** **A)** Chemical structure of the different imidazole compounds used to grow ZIF crystals. (i) 2-Mim, (ii) 4-TBim, (iii) Bim, and (iv) 6-BBim. **(B)** Plot of the peak wavelength **(C)** and intensity against time after laser power increase. Color corresponds to the precursor used and are illustrated in (A). On right are Gaussian fits to histograms of the last 3% of the plotted data for each particle. The histograms for both wavelength and intensity are presented in **Figure 3-18**. ........................................................................................................................ 54

**Figure 3-17** **A)** *Left*: Testing the growth of 4-TBim on an 80 nm AuNP at different trapping laser powers. 30 mW (orange), 40 mW (blue), 50 mW (purple), and 60 mW (green). *Right*: Gaussian fits for histogram of the final wavelength achieved during growth illustrating average final wavelengths 30 mW (568 nm), 40 mW (595 nm), 50 mW (611 nm), and 60 mW (622 nm). Histograms are of the last 3% of data from each particle. **B)** Plotting the shell thickness predicted from plasmon scattering cross section calculations against the radial distance that the particle is predicted to be above 45 $^{o}$C. Inset plots the slope of each fit line against its corresponding refractive index to illustrate which refractive index shell agrees best with our expectation. This occurs at $n \approx 1.7$. ........................................................................................................................ 55

**Figure 3-18** *left*) Histogram of the max wavelengths measured during growth. *right*) Histogram of the max intensities measured during growth. ......................... 56

**Figure 3-19** Showing the temperature decays for temperatures associated with powers used in figure 6 of main paper. Calculation for an 80 nm diameter AuNP in a sharply focused optical trap, located 200 nm above the focal plane in ethanol as the solvent. Black line represents room temperature, or a 0 mW trap. Purple dashed line is 45 $^{o}$C which we claim to be the cut-off temperature for driving growth with this technique. ......................................................................... 57

**Figure 4-1** A) Basic nanoparticle dimer system. Two gold nanoparticles are separated by a distance s and linked together by short polymer chains. B) Structures of the molecules used to dimerize gold nanoparticles. From top to bottom, (11-mercaptoundecyl) tetra(ethylene glycol) (MUTEG), 11-mercaptoundecanol (MUA) and , 2-{2-[2-(2-mercaptoethoxy) ethoxy]ethoxy}ethanol) (MEEE) 63

**Figure 4-2: A)** Shows the transverse plasmon of our optically trapped AuNP dimers. i) Illustration of the DF polarization relative to trapping laser. Transverse plasmon activated when illumination perpendicular to trapping laser. Top-down illustration of the trapped dimer orientated parallel to the laser polarization. ii) Image captured of an optically trapped dimer under conditions described in i). **B)** Shows the longitudinal plasmon of our optically trapped dimers. i) Illustration of the DF polarization relative to trapping laser. Longitudinal plasmon activated when illumination parallel to trapping laser. ii) Top-down illustration of the trapped dimer orientated parallel to the laser polarization. iii) Image captured of an optically trapped dimer under conditions described in i) and ii). **C)** Polarization dependent scattering spectra of a single dimer. Going from black to red, we rotate the polarization of the DF illumination to go from parallel with the longitudinal axis ($0^o$) to perpendicular with the longitudinal axis. ........................................................................ 66

**Figure 4-3** A) Modelled scattering cross sections of a dimer where each curves represents a different particle separation. As the dominant peak blue shifts, the separation between the particles is increasing. B) The peak positions of the modelled curves from A. C) Experimental data of dimer peaks collected using three different linking molecules. Green is MUTEG, orange in MEEE, and purple is MUA. ........................................................................................... 68

**Figure 4-4** A) Experimentally measured scattering spectra of an optically trapped gold nanoparticle. Time is increasing as we go from the darkest curve in the back to the light blue curve in the front. Measurements were collected over a period of 20 seconds with 25 ms acquisition times. B) The black curve shows the peak wavelengths found by fitting a double Lorentzian curve to the measured spectra on the left. The blue curve shows the calculated separations determined from those measured peak wavelength values...................................................... 71

**Figure 4-5** Each plot represents a single optically trapped gold nanoparticle dimer as the laser power is gradually increased. Scans were collected at 20 Hz with 50 ms acquisition times. A) shows a case where the spectra originally peaked at 600 nm, redshifted towards 650 nm, and then fell apart. B) Shows an example where the peak started centered at 600 nm and gradually decayed down to the monomer resonance. C) Shows a case where the resonance originally peaked at 640 nm and gradually blue shifted until separating into the monomers .... 73

## LIST OF ABBREVIATIONS

| | |
|---|---|
| $\langle S \rangle$ | Time averaged pointing vector |
| $\nabla$ | Nabla (differential operator) |
| $\nabla E^2$ | Gradient of the electric field |
| 2-Mim | 2-methylimidazole |
| 4-TBim | 4-tertbutylimidazole |
| 6-BBim | 6-bromobenzimidazole |
| AFM | Atomic force microscope |
| Au NP | Gold nanoparticle |
| Au@ZIF | Gold ZIF core@shell particle |
| AuNP@MOF | Gold nanoparticle – metal organic framework hybrid structure |
| Bim | Benzimidazole |
| c | speed of light |
| $C_{abs}$ | Absorption cross section |
| $C_{scat}$ | Scattering cross section |
| CW | Continuous wave |
| DF | Darkfield |
| DMF | Dimethylformamide |
| e.g. | Exempli gratia (for example) |
| EG | Ethylene Glycol |
| EM | Electromagnetic |

| | |
|---|---|
| $F_{grad}$ | Gradient force |
| FPGA | Field programmable gate array |
| $F_{scat}$ | Scattering force |
| Hz | Hertz |
| I | Intensity |
| IMF | Intermolecular forces |
| k | wavevector |
| LED | Light emitting diode |
| LOD | Limit of detection |
| LSPR | Localized surface plasmon resonance |
| MOF | Metal Organic Framework |
| MSD | Mean square distance |
| n | Refractive index |
| NA | Numerical aperture |
| $n_m$ | Refractive index of medium |
| nm | Nanometer |
| $n_p$ | Refractive index of particle |
| NP | Nanoparticle |
| OT | Optical tweezer/optical trap |
| P | Power of laser |
| PS | Polystyrene |

| | |
|---|---|
| PVP | Polyvinylpyrrolidone |
| QPD | Quadrant photodiode |
| $r$ | Radius |
| RI | Refractive index |
| s | Second |
| SERS | Surface enhanced Raman spectroscopy |
| SOT | Spectroscopic optical tweezer |
| $z$ | axial position |
| ZIF | Zeolitic imidazolate framework |
| $\alpha$ | Polarizability |
| $\delta$ | Interaction skin depth |
| $\Delta\lambda$ | Difference between wavelengths |
| $\varepsilon$ | Dielectric constant |
| $\varepsilon_m$ | Dielectric constant of medium |
| $\varepsilon_p$ | Dielectric constant of particle |
| $\kappa$ | Stiffness |
| $\lambda$ | Wavelength |
| $\lambda_o$ | Resonance wavelength |
| $\pi$ | Pi |
| $\rho$ | Transverse displacement |
| $\omega_0$ | Beam waist |

$\omega_z$……………………………………………………….Beam radius at height z

# Chapter 1: INTRODUCTION

## 1.1 MOTIVATION

Optical tweezers were first built by Arthur Ashkin in 1970 at Bell Labs when he demonstrated levitation of latex beads by a vertically propagating laser beam.[1,2] He would later go on to demonstrate 3-dimensional trapping, with a sharply focused laser beam, of dielectric particles,[3] manipulation of organelles in a cell,[4] and trapping of viruses and bacteria.[5] Jumping forward to 2018, Ashkin was rewarded with the Nobel Prize in physics for his work in developing the optical tweezer technique.

Since Ashkin's early development optical tweezers have been greatly improved, such that they have now been used to trap metallic nanoparticles,[6,7] perform studies on DNA and RNA with base-pair resolution,[8–10] determine protein structure and function,[11–13] and combine single atoms in a trap to make a molecule.[14,15] Excluding atomic trapping, these experiments are performed in water or air, and have been generally applied to study biochemical systems. In order to perform novel single molecule spectroscopy measurements on chemical systems, such as determining polymer structure or kinetically characterizing chemical intermediates in reactions, we need to make optical trapping possible in organic solvent environments.[16] This has proven nontrivial, as the physical properties of conventional optical trapping materials do not allow for trapping in organic environments.

To expand the functionality of optical tweezers beyond the biological, different trapping probe materials have been suggested.[16,17] We have chosen to move away from these custom dielectric material and instead attempt to use gold nanoparticles as efficient optical trapping probes in high index solvents. This thesis presents a technique for optically trapping gold nanoparticles in an optical trap (Chapter 2) and then demonstrates the ability to drive and characterize a chemical reaction using the optically trapped gold probe (Chapter 3).

## 1.2 OPTICAL TWEEZER TECHNIQUE

The optical tweezer technique is based on the use of a conventional optical microscope with a highly focused laser beam coupled into the system. Highly focused light is used to apply forces upon dielectric microparticles and metallic nanoparticles and trap them stably in three dimensions. The potential in an optical trap can be approximated as a harmonic well and so the total trapping force being applied to a particle can be written as

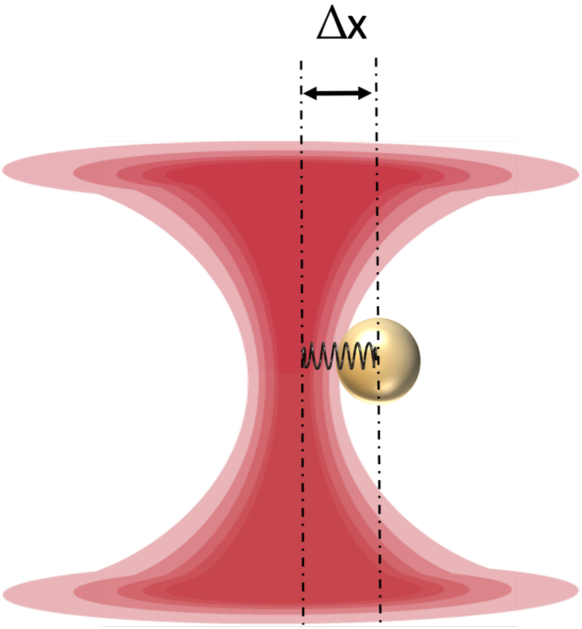

**Figure 1-1** Basic diagram of a particle displaced from the optical trapping focus. Spring used to illustrate the restoring force back towards center

$$F = -\kappa \Delta x$$

Equation 1.1

where F is the force, κ is the trap stiffness, and Δx is the displacement of particle from the trap center.[18]

### *1.2.1 RAY OPTICS TRAPPING MECHANISM*

When the object being trapped larger than, or similar to, the wavelength on the trapping laser in the trapping medium (e.g. 2 μm diameter particle in 1064 nm laser trap)., the dominant trapping mechanism can be described through ray optics.[3,19] When a ray of light passes through the boundary of a material of one refractive index into a material with a different refractive index, the k-vector of the light shifts. In order to conserve momentum, the particle experiences an opposing force opposite to that of the ray of light. An appropriate refractive index mismatch between the trapped particle and the surrounding medium is critical for successful trapping. In order to successfully trap these particles, the refractive index of the particle must be larger than the refractive index of the medium.[3,20,21]

### *1.2.2 POINT DIPOLE TRAPPING MECHANISM*

As opposed to the ray optics regime, point dipole trapping is used to describe particles that are smaller than the wavelength of light (e.g. 100 nm diameter particle in 1064 nm laser trap). Trapping strength in this case primarily relies on the polarizability of the particle in the trapping medium. This polarizability relies heavily on the relative wavelength dependent dielectric constants of the trapped particle and the surrounding medium, and can described by the Clausius-Mossotti relation

$$\alpha_p = 3V_p\left(\frac{\varepsilon_p - \varepsilon_m}{\varepsilon_p + 2\varepsilon_m}\right)$$

Equation 1.2

where $\alpha_p$ is the particle polarizability, $V_p$ is the particle volume, $\varepsilon_p$ is the dielectric constant of the particle, and $\varepsilon_m$ is the dielectric constant of the material. The dependence of trapping forces on the polarizability are explored in depth in chapter 2.

The point dipole approximation is most frequently applied to metallic nanoparticles, which have very high polarizabilities arising from a very high magnitude dielectric constant relative to most solvents. The dielectric value of gold for 1064 nm light is $\varepsilon_p = -48.450 + 3.6i$ in comparison to the dielectric constants for water at $\varepsilon_{water} = 1.77$, which translates to expecting incredibly high polarizabilities and therefore a strong trapping potential.

## 1.3 PLASMONS

Plasmons are a collective oscillation of electrons in a material in response to incident electromagnetic (EM) radiation. Surface plasmon resonance is the wavelength of light for which electrons in a thin metal layer are excited to propagate parallel to the surface.[22–24] In nanoparticles, this is referred to as the localized surface plasmon resonance (LSPR).[25–28] Plasmon resonance in nanoparticles is controlled by the material, size, and shape of the nanoparticle, where larger particle have redder resonance, and asymmetric shapes can result in multiple resonances. These particles can be applied as reaction catalysts,[29,30] used to enhance spectroscopic signals,[31,32] or even act as nanothermometers.[33–35]

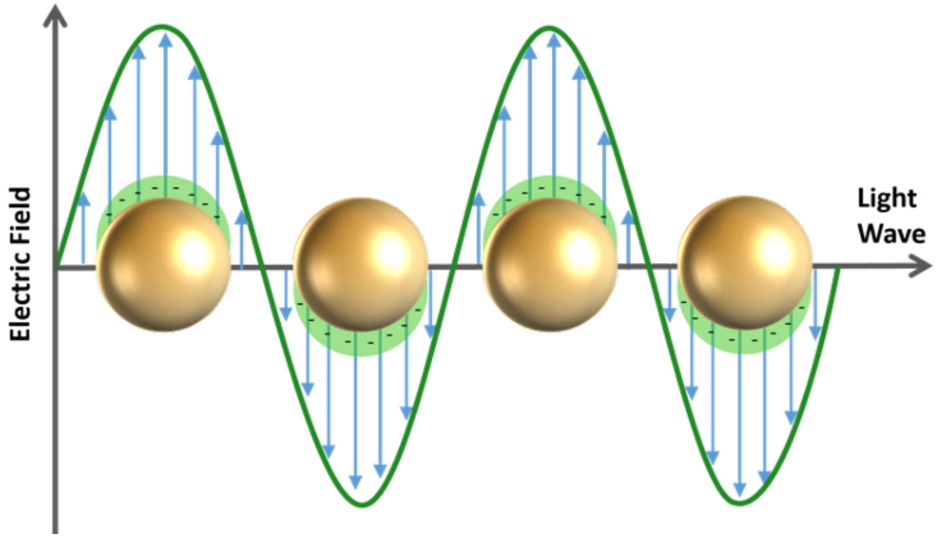

**Figure 1-2** Illustration of the plasmon resonance of a spherical gold nanoparticle. Green cloud represents the electron cloud oscillating along with the frequency of the incident light wave.

### *1.3.1 SCATTERING AND DIELECTRIC CONSTANTS*

The plasmon resonance of a system depends on the wavelength-dependent dielectric constant of the material and the surrounding medium. Even in the same medium, such as water, the peak wavelength will greatly vary for different metals. For example, silver nanospheres tend to have resonance in the region of 400 nm light, while gold nanospheres tend to resonate near 550 nm light.

### *1.3.2 HEATING NANOPARTICLES*

When interacting with light, nanoparticles will absorb some energy and remit it as heat. This heating can be extreme to the point of boiling solutions when optically trapping nanoparticles.[36–38] While heating can be detrimental to biological molecules and some polymers, it offers a benefit of being able to drive thermally catalyzed reactions, making a potential flaw beneficial. Heating will be discussed in Chapter 2, and then an application utilizing the heating of gold nanoparticles will be presented in Chapter 3.

## 1.4 SPECTROSCOPY

Spectroscopy is an optical technique that allows a researcher to study the electronic and vibrational properties of a material. When coupled into an optical tweezer to make a spectroscopic optical tweezer (SOT) we are able to optically study a wide range of microscopic and nanoscopic materials found in suspensions such as living cells, organelles, and metallic nanoparticles.[39]

### *1.4.1 FORCE SPECTROSCOPY*

Force spectroscopy is technique that uses small applied forces from an instrument to study to characterize physical properties of molecules, such as studying the binding strength between two individual molecules, probing folded protein structures, or observing the melting of double stranded DNA.[17,40,41]

### *1.4.2 DARKFIELD MICROSCOPY AND SPECTROSCOPY*

Darkfield is an optical imaging technique that is used to observe subdiffraction sized features and particles.[42,43] This technique uses a highly focused annular beam to illuminate a material, and then back scattered light is collected to observe, in our case, an optically trapped nanoparticle. A major benefit of darkfield arises from the annular characteristic on the excitation beam. An annular beam is a hollow beam which results in a cross section resembling a donut. When focused on a material, light is scattered backwards to be collected by the camera or spectrometer while the excitation light does not return backwards, hence a “darkfield” background for the particle.

### *1.4.3 RAMAN SPECTROSCOPY*

Raman spectroscopy is a spectroscopic technique designed to measure the vibrational modes of molecules and crystals.[44–46] This technique can couple well with optical tweezer technique and has been used to differentiate and sort biological cells,[47,48] characterize dielectric microparticles,[49–51] and identify single molecules.[52,53]

## 1.5 THESIS OUTLINE

This thesis present experiments to develop an optical trapping technique for work in organic solvents as well as demonstrates an application for nanoparticles trapped in organic solvents.

Chapter 2 focuses on optical trapping in high refractive index solvents as we begin moving away from purely aqueous systems into organic systems. We studied how the behavior of trapped gold nanoparticles changed as the index of the surrounding medium was gradually increased. We use computational models to predict relevant trapping forces in an attempt to explain the behavior that we observed. We then apply a separate model to show how heating of a trapped gold nanoparticle becomes drastically far more significant in low thermal conductivity solvent like dimethylformamide (DMF). While many groups had previously suggested the shape of a force curve was affected by local heating of the nanoparticle, we presented a new theory that the trend of the trap stiffness with trapping laser power is actually affected by changes to the particle equilibrium trapping position with increasing laser power. This work was published in J. Phys. Chem. Lett. in 2023.[54]

Chapter 3 presents a novel technique for synthesizing zeolitic imidazolate framework (ZIF) crystals on the surface of optically trapped gold nanoparticles. The technique takes advantage of the fact that gold nanoparticles will reach high temperatures when optically trapped to catalyze the growth of the crystals on the nanoparticle surface. We present computational models of plasmon scattering cross sections to illustrate how we expect the particles will look as the crystal grows. This work was published in RSC Nanoscale in 2024.[55]

Chapter 4 summarizes the final projects being worked on prior to the publication of this thesis. This work is focused on creating dimerized nanoparticles and studying their behavior in an optical trap. We will present a plasmon ruler formula generated from scattering cross section computation models, and apply it to experimental measurements to predict the separation of two coupled nanoparticles. Currently we are researching the effect of increasing laser powers, and thereby increasing temperatures, on the separation and destruction of coupled nanoparticles.

# Chapter 2: SIMULTANEOUS FORCE AND DARKFIELD MEASUREMENTS REVEAL SOLVENT-DEPENDENT AXIAL CONTROL OF OPTICALLY TRAPPED GOLD NANOPARTICLES

## 2.1 INTRODUCTION

Optical tweezers (OT) have become an essential tool for mechanistic investigations of molecular processes in aqueous conditions,[56,57] providing insight into atomistic structure and energetics of biological machines and polymers. OT have higher force resolution of other force probes, such as the atomic force microscope (AFM), and function optimally in solution. The breakthroughs afforded by OT technology in biophysics and molecular biology were recognized by the 2018 Nobel Prize in Physics. Despite this demonstrated potential for studying single molecules and interactions, the OT technique has not been utilized in non-aqueous conditions to probe the structure, mechanics and energetics of non-biological polymers, molecular machines and solution-based chemistry. This gap is a result of incompatibility of most existing OT probes with organic solvent environments.[16,58,59] A lack of appropriate probes has also prevented OT from being applied to the growing field of chemical imaging using force-detected absorption spectroscopy, which has so far been almost exclusively performed with AFM at lower force resolution.[60–62] Here, we demonstrate optical trapping in common organic solvents using gold nanoparticles (Au NPs). We leverage our instrument's unique ability to trap, image and detect force of noble metal NP simultaneously to characterize, for the first time, and explain solvent-dependent trapping effects and dynamics of Au NP. We discover that modulating laser power can enable axial control of particle positions in organic solvents. Our work opens the possibility of in situ tracking of chemical transformations on the single molecule level using OT and of leveraging the unparalleled force resolution of the OT for force-detected absorption spectroscopy using plasmonics Au NPs.

The core of the OT instrument is an optical microscope combined with a laser beam focused at the sample plane. The beam focus applies a restoring force on dielectric microscopic particles and can confine them in 3-dimensions in solution. Commonly used dielectric probe materials, such as silica and polystyrene, are not suitable for tweezing in organic solvent environments or for force-detected absorption spectroscopies. A requirement for achieving stable trapping is a sufficient refractive index (RI) mismatch between the higher index dielectric particle and the lower index trapping medium.[3,41] Silica $(n_{silica} = 1.45)$ lacks the high RI mismatch with many organic solvents $\left(\text{typical } n_{organic} > 1.4\right)$. In contrast, a commonly used higher index material, polystyrene (PS) $(n_{PS} = 1.57)$, has a sufficient RI mismatch but breaks down in common organic solvents. Recent studies have used synthetic approaches to increase the effective RI of silica microspheres through the inclusion of a polystyrene or zinc oxide core.[16,58] However, these non-metallic probes are still not appropriate for force-detected spectroscopy where high polarizability is necessary.

An alternative trapping probe material for OT proposed here is a noble metal, such as gold or silver.[63] Gold nanoparticles (Au NP) have been shown to trap efficiently in water due to the high polarizability of metals.[6,19,64,65] The large magnitude of the dielectric constant of gold indicates that it will stably trap in the majority of available solvents. Gold is inert, but also functionalizable, in most solvent environments, and has the potential to serve as a universal OT probe material in both aqueous and organic solvent conditions. Furthermore, trapping of highly polarizable metal NP has applications in force-detected absorption spectroscopies.[17,60,61,66,67] However, only *nano*scale Au particles less than ~200 nm in diameter can be stably trapped using a 1064 nm trapping beam due to excessive scattering forces which grow with increasing particle size.[64] Using sub-diffraction sized Au NP for trapping in conventional OT systems is challenging because they are not visible under standard bright field illumination.[43] In most prior work, integrated darkfield spectroscopy allowed imaging of the NP, but blocked the trapping laser detection channel, preventing particle displacement and force measurements.

Here, we demonstrate an instrument which overcomes these difficulties by combining an OT with a custom darkfield (DF) microscope and spectrometer module. With the addition of DF, we detect the trapped Au NPs through their plasmonic scattering. Unlike virtually all other reported setups, ours can record NP displacements and DF spectra in parallel, allowing correlative force and DF spectroscopy measurements.[68] This unique capability allows us to not only confine NP, but also characterize their diffusion and trapping efficiency to compare across solvent environments. This study is the first to demonstrate stable optical trapping of single Au NPs in organic solvent conditions, including in dimethylformamide (DMF), a common organic solvent compatible with solution phase chemistry, and to characterize the heating and dynamics of single particles. Using these measurements, we expand existing understanding of solvent-dependent optical trapping which can be leveraged for new application of single molecule and single particle spectroscopies. We find that trapping in DMF, while stable, is not as efficient as expected from standard models of trapping force which predict most efficient trapping of Au NP in high RI solvents. In contrast, our measurements show that trapping stiffness, which characterizes trapping efficiency, is lowest for DMF compared to other solvents in the transverse direction, (*x* direction in **Figure 2-1**A), and highest in the axial direction (*z*

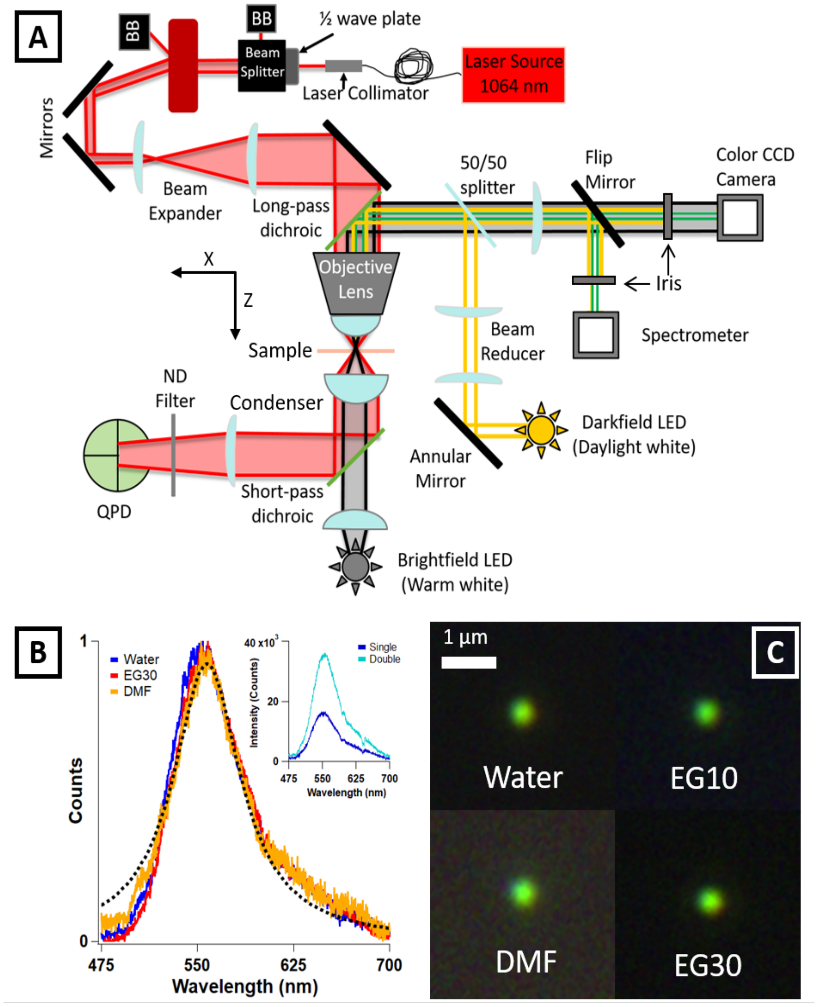
A
BB
BB
½ wave plate
Beam Splitter
Laser Collimator
Laser Source 1064 nm
Mirrors
Beam Expander
Long-pass dichroic
50/50 splitter
Flip Mirror
Color CCD Camera
Iris
Spectrometer
Objective Lens
X
Z
Sample
Beam Reducer
ND Filter
Condenser
Darkfield LED (Daylight white)
Annular Mirror
QPD
Short-pass dichroic
Brightfield LED (Warm white)
B
Water
EG30
DMF
Counts
1
0
475
550
625
700
Wavelength (nm)
40 x10³
Intensity (Counts)
20
0
Single
Double
C
1 µm
Water
EG10
DMF
EG30

**Figure 2-1** A) Instrument schematic of the custom built optical tweezer and DF microscope used here. B) LSPR scattering spectra of optically trapped 80 nm Au NP in a subset of solvents used here. Black dashed line is a Lorentzian fit for the DMF spectra. Inset: LSPR spectra of a single 80 nm Au NP (dark blue) and two 80 nm Au NP (pale blue) trapped in the OT. The peak in the spectrum shifts towards red and the intensity increases when two particles are trapped. C) DF images of 80 nm gold nanospheres trapped and suspended away from surfaces in different solvent environments. Spectra in (B) were recorded on the same particles as shown in images.

direction). By combining measurements of trap stiffness with standard models of heating, trapping, and scattering, we demonstrate that forces pushing particles out of the trap, which also depend on the RI, determine trapping efficiency trends across solvents. Specifically, the balance between the trapping and the pushing forces establishes the equilibrium *z* bead position downstream of the trap focus. We show that in DMF, this trapping equilibrium is furthest from the focus when compared to other solvents, resulting in the weakest transverse trap potential. By adjusting power, we can control not only the transverse direction stiffness, but also the axial position of the trapped particle. Overall, this work establishes Au NPs as promising OT probes across multiple solvent conditions with applications in single molecule and single particle optical and force spectroscopy measurements of non-biological polymers and small molecules.

## 2.2 RESULTS AND DISCUSSION

### *2.2.1 Experimental Design and Instrumentation*

**Figure 2-1**A depicts our combined optical tweezer and DF microscope setup. Briefly, we achieve stable OT using a collimated 1064 nm continuous wave Gaussian laser beam (IPG Photonics #YLR-5-1064-LP) which fills the back focal plane of the objective (Nikon #MRD01991) and is focused at the sample. We detect particle displacement in the trap using a standard back focal plane interferometry technique where the quadrant photodiode (QPD) (Mouser Electronics #718-QP154-QHVSD) images the back focal plane of the condenser.[69] To enable DF, we use a white light emitting diode (LED) (Thorlabs #SOLIS-3C) and a custom annular mirror to generate a hollow, collimated,

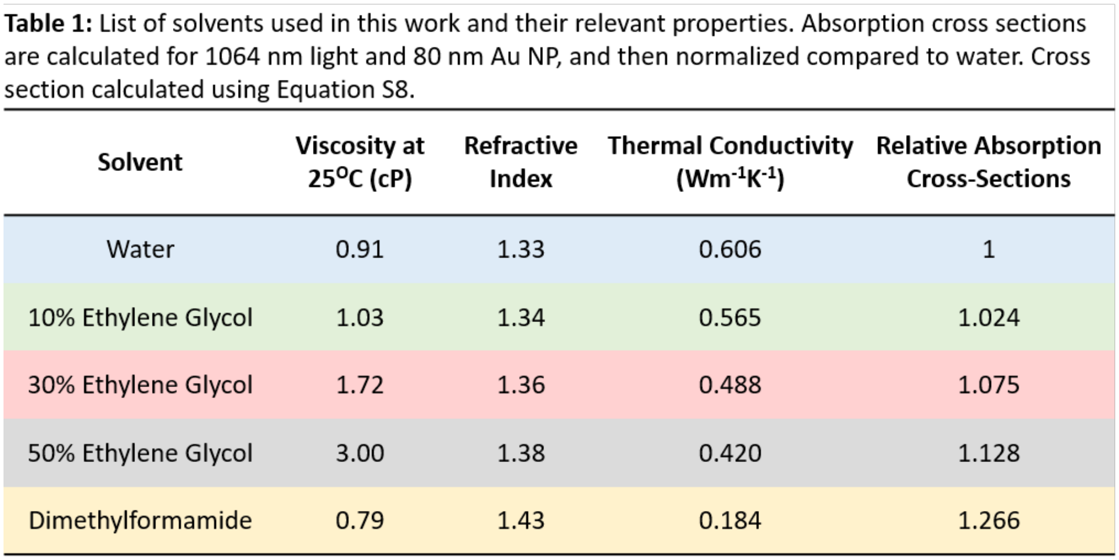

**Table 1:** List of solvents used in this work and their relevant properties. Absorption cross sections are calculated for 1064 nm light and 80 nm Au NP, and then normalized compared to water. Cross section calculated using Equation S8.

| Solvent | Viscosity at 25$^{O}$C (cP) | Refractive Index | Thermal Conductivity (Wm$^{-1}$K$^{-1}$) | Relative Absorption Cross-Sections |
|---|---|---|---|---|
| Water | 0.91 | 1.33 | 0.606 | 1 |
| 10% Ethylene Glycol | 1.03 | 1.34 | 0.565 | 1.024 |
| 30% Ethylene Glycol | 1.72 | 1.36 | 0.488 | 1.075 |
| 50% Ethylene Glycol | 3.00 | 1.38 | 0.420 | 1.128 |
| Dimethylformamide | 0.79 | 1.43 | 0.184 | 1.266 |

excitation beam expanded to fill the back of the trapping objective; this system replaces a standard DF condenser which blocks the trapping beam from the QPD. The scattered light from the Au NP is collected in an epi configuration by the same objective. An iris in the back focal plane acts ensures that only the scattered localized surface plasmon resonance (LSPR) signal is detected for analysis of trap contents.

The strength of our combined OT and DF setup is that it allows simultaneous trapping, spectroscopic imaging and force sensing of the nanoparticles in various solvent and chemical environments. We use DF to see the Au NP in the far field in our microscope, which makes the trapping experiment possible. Additionally, we direct the collected DF signal into a spectrophotometer to detect the LSPR spectrum, which is highly sensitive to the particle size, shape, and material.[70,71] In parallel, we measure the particle diffusion and force using the QPD signal.

The solvents used in this work are listed in Table 1 along with their relevant physical properties. Water has the lowest RI of 1.33. We combine water and varying fractions of ethylene glycol (EG) to produce mixtures containing 10%, 30%, and 50% EG, denoted as EG10, EG30, and EG50 respectively. These mixtures are characterized by increasing RI values and decreasing thermal conductivity when compared to water. We also use DMF, which has the highest RI of 1.43 and by far the lowest thermal conductivity of solvents in our experiments.

Representative spectra and DF images of single Au NPs stably trapped in water, EG10, EG30 and dimethylformamide (DMF) are shown in Figure 1B and C respectively. In all solvents, we are able to catch an Au NP in the OT by tracking it in the DF, and collect a DF color image and LSPR spectra to differentiate single trapped particles from doubles or clumps (Figure 1B inset). The spectra of single Au NPs in Figure 1B fit well to a single Lorentzian line shape, as shown with a dashed line for DMF. The fits reveal maximum scattering at 555-560 nm, which is consistent with predicted scattering of single spherical

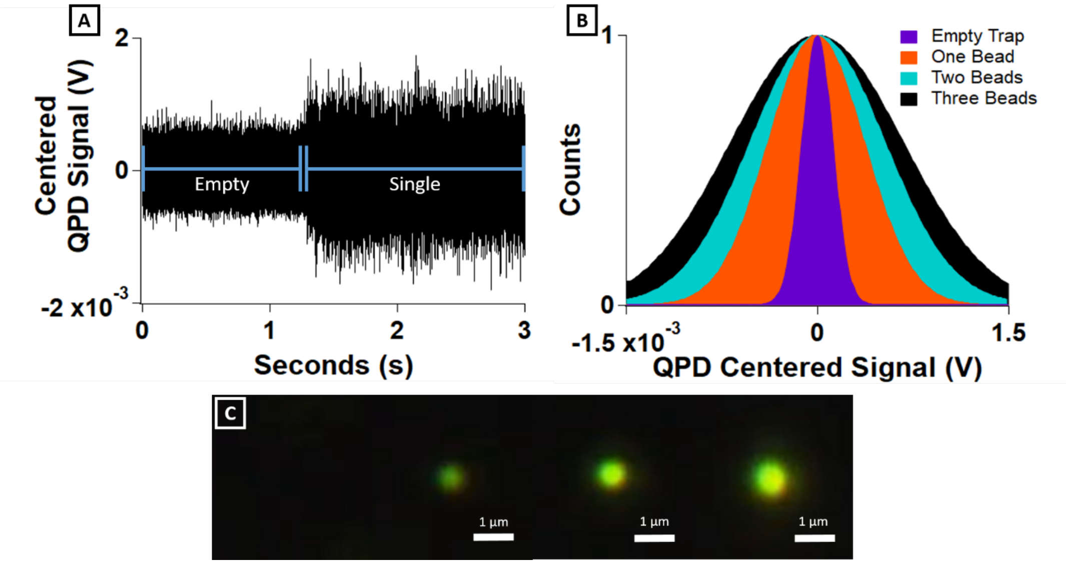

**Figure 2-2** A) Centered raw data output from QPD showing the difference in signal as one 80 nm Au NP enters the trap. B) Histogram of particle displacements (in QPD voltage units) showing the increasing MSD as multiple particles enter the trap. C) Images associated with the shown histogram. From left, empty trap, one particle, two particles, and three particles. Light intensity was reduced for these images to prevent three particle image from saturating the camera.

80 nm Au particles (see SI for more details). Importantly, the presence of two or more particles within the trap results in higher LSPR intensity, red-shifted spectra, and distinct particle displacements as shown in the inset of **Figure 2-1**B and **Figure 2-2**.

### *2.2.2 IDENTIFYING A SINGLE PARTICLE USING OT AND DF*

Identifying a single particle using OT and DF. Raw displacement data of an 80 nm Au NP entering the trap is presented in **Figure 2-2**A. The black line is the raw data collected at 400 MHz directly from the QPD in mV. The first ~1.25 sec of data is of an empty trap. At ~1.25 seconds, there is a sharp spike in the signal and a subsequent increase in the displacement signal indicating that a particle has entered the trap. The raw data is smoothed using a boxcar method and the smooth average was subtracted from raw data to center it and to remove low frequency drift for calculations of, the mean square displacement (MSD).

Once a single Au NP is trapped and detected in the DF, we can track the position of the particles undergoing Brownian motion relative to the trap focus, which is defined as zero displacement.[72] We use an established calibration procedure to determine a conversion between QPD voltage signal and distance units.[69] The resulting NP displacements along the x direction indicated in **Figure 2-1**A, recorded at 400kHz over 3 seconds with a trapping laser power of 32 mW, are plotted as a time course and binned in a histogram in **Figure 2-3**A, left and right panels respectively. We observe that for all solvents, the particle displacements are normally distributed as expected for a quadratic confining potential, which indicates stable trapping in all solvents.[73] We note that Au NPs can remain dispersed in all solvents for days and even weeks without deteriorating, demonstrating true stability in both aqueous and organic conditions.[58]

We can now compare trapping efficiency of Au NPs across varying solvent conditions. According to standard models, it is expected that trapping of noble metal nanoparticles should be more efficient in organic solvents, which have a higher RI than water. The restoring trapping force, $F_{grad}$, is due to the gradient of the electric field intensity, $I$, and scales with the particle polarizability, $\alpha$, which depends on the dielectric constant mismatch:

$$F_{grad} = \frac{|\alpha|}{4}\nabla \mathrm{I}\ , \qquad \alpha = 3V_p\left(\frac{\varepsilon_p-\varepsilon_m}{\varepsilon_p+2\varepsilon_m}\right)$$

Equation 2.1

In Equation 2.1, $\varepsilon_m$ is the medium dielectric constant, $\varepsilon_p$ is the particle dielectric constant, and $V_p$ is the particle volume (see the SI for more details).[3,6] Dielectric constant relates to RI by $n = \sqrt{\varepsilon}$. Based on Equation 2.1, we expect trapping efficiencies at small

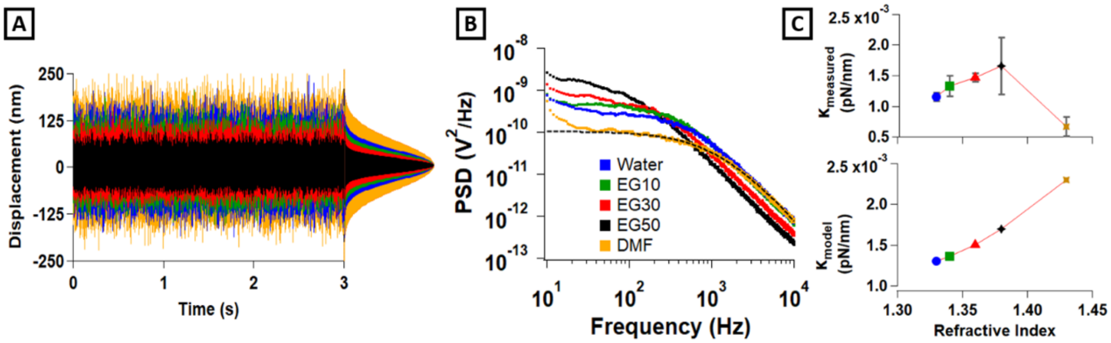

**Figure 2-3** A) Displacements of 80 nm Au NP trapped in the OT (left) and displacement histograms (right) in various solvents. Slow drift has been subtracted from the data. B) PSD of optically trapped 80 nm Au NPs in different solvents determined from displacements in Figure 1D. PSD curves have been smoothed to 10 Hz. Dashed line shows a Lorentzian fit to the DMF data. C) Top plot shows the measured stiffness at 32 mW based against refractive index of the medium. Bottom plot is modelled stiffness at 32 mW of 80 nm Au NP using Equation 2.1.

displacements to scale linearly with trapping beam power for Gaussian beams as derived in Equation 2.30. Furthermore, we see that for particles with a large imaginary component of $n_p$, such as Au NPs, $\alpha$ and thereby $F_{grad}$, increase with $n_m$. Following this reasoning, we expect an increase in trapping stiffness with increasing solvent RI.

To characterize trapping efficiency experimentally, we use the measured displacements to construct PSDs of particle motion, as shown in **Figure 2-3**B. In all solvents, the PSD shows a characteristic Lorentzian shape, indicating stable trapping. We observe that both Lorentzian fit parameters—the cut-off frequency, $f_c$, and the amplitude *A*—depend on the solvent environment. Specifically, $f_c$ is greatest for DMF and least for EG50, while *A* shows the reverse trend. Both of these parameters reflect the varying solvent conditions, such as viscosity and heating in the trap, as well as potentially real changes to trapping efficiency, characterized by stiffness, in the various media.[69] Stiffness $\kappa$ is related to $f_c$ through

$$\kappa = 12\pi f_c \eta R$$

Equation 2.2

Here $\eta$ is the viscosity of the solvent and *R* is the particle radius. The Lorentzian amplitude *A* can be related to the diffusion constant, *D*, of the particle in each solvent.[69] According to Einstein's diffusion equation, D is related to solvent viscosity $\eta$ through

$$D = \frac{k_B T}{6\pi\eta R}$$

Equation 2.3

We note that the viscosities, $\eta$, of the solvents in this study, listed in Table 1, vary by a factor of three. Thus, we cannot related measured differences in $f_c$ between solvents

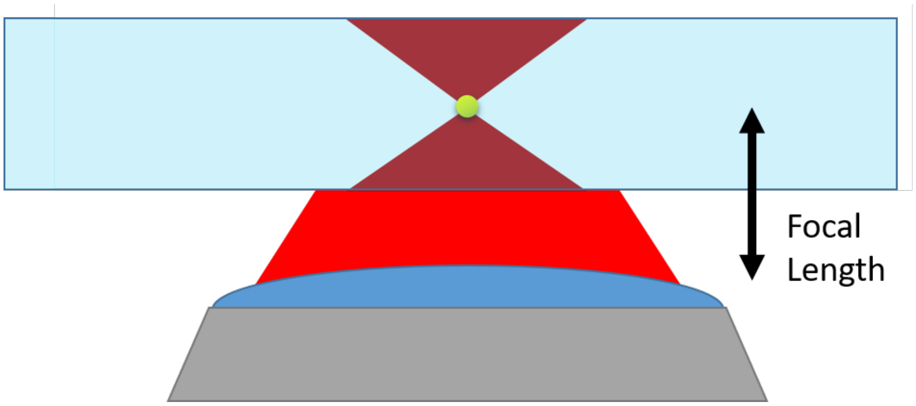

**Figure 2-4** Illustration of calculation for total power reaching the particle.

directly to stiffness values using Equation 2.2 as is often done for aqueous conditions. Furthermore, gold absorbs the 1064 nm trapping laser illumination, leading to significant heating around the trapped particle.[7] The expected surface temperatures of Au NP under 1064 nm illumination in different solvents are calculated below. The temperature increase in organic solvents like DMF is expected to be higher than in aqueous conditions due to higher particle polarizability in high RI media and lower thermal conductivity, leading to a further divergence of their viscosity values.

We account for these differences in solvent environments and for heating effects by determining $D$ directly from our measurements and extrapolating $\eta$ using Equation 2.3 before solving for stiffness.[7] First, we use a heating model, detailed in the SI, to calculate the temperature in the immediate vicinity of the trapped particles. The model accounts for the absorption cross section of Au NPs in various solvents, the power density of the laser at the trapping point as shown in **Figure 2-4**, Equation 2.5 and Equation 2.8, and the thermal conductivity of the solvent. This model has been previously shown to accurately predict temperature around Au NP in water.[6,7] The calculated temperature values are shown in **Figure 2-5**.

### *2.2.3 HEATING MODEL*

To gauge whether extreme heating can account for the deviations from the expected stiffness trends, we use a heating model developed previously.[6,7] The model accounts for the absorption cross section of Au NPs in various solvents, the power density of the laser at the trapping point, and the thermal conductivity of the solvent.[6,7] The rate of temperature increase at the particle surface per unit of additional trapping power is proportional to the polarizability of the Au NPs and inversely proportional to the thermal conductivity of the solvent. For example, in DMF the model predicts a temperature over 100ºC at 32 mW of power, which is almost four times the temperature in water. This trend is in qualitative agreement with our expectations that the lower thermal conductivity and higher polarizability of organic solvents leads to more extreme temperatures. We note that the level of heating in organic solvent is significant and may be a useful experimental tool for future applications to drive temperature dependent reactions. We concluded however that the increase in temperature at higher power, while notable, does not explain the deviations from expected linear dependence of stiffness on power or on RI.

In order to predict the magnitude of heating of our particles in an optical trap, we model the amount of infrared light absorbed and the conduction of the resulting heat into the surrounding environment. To begin, we determine the amount of 1064 nm light incident to the particle based on the focal angle of the microscope objective lens.

$$\Theta = \frac{NA}{n_{oil}}$$

Equation 2.4

$\Theta$ is the divergence angle of light in radians, NA is the numerical aperture of the objective lens, and $n_{oil}$ is the refractive index of objective immersion oil. At material boundaries, there is reflection for high angle light resulting in a reduction in beam radius and power reaching the sample. The reduction in radius is based on the critical angle at the material boundaries. The angle is reduced until it falls below the critical angle. All future calculations are performed using this angle. Due to a reduction in the total beam reaching the sample, the true power is calculated using[74]

$$P(r) = P_{\infty}\left[1 - e^{\frac{-2r^2}{\omega_0^2}}\right]$$

Equation 2.5

The beam radius at the focal point will be determined by:

$$\omega_0 = \frac{\lambda}{\pi\Theta}$$

Equation 2.6

$\omega_0$ is the beam radius at the focal point and $\lambda$ is the effective wavelength of the trapping beam (1064 nm) in the trapping media (e.g. water). The Rayleigh length $z_R$ is the distance away from the beam waist, along the propagation direction of a beam, where the area of the cross section has doubled. [75]

$$z_R = \frac{\pi\omega_0^2}{\lambda}$$

Equation 2.7

$$\omega(z) = \omega_0 \sqrt{1 + \left(\frac{z}{z_R}\right)^2}$$

Equation 2.8

$\omega(z)$ is the beam radius at a position $z$ away from the trapping laser focal point. By definition, when $z = z_R$, $\omega(z) = \sqrt{2}\omega_0$ and the Gaussian beam cross sectional area is double that of the area at the beam focal position. The average intensity of the light sampled by the particle as it diffuses in the trap is described by:

$$I(z, \rho) = I_z e^{\frac{-2\rho^2}{\omega_z^2}}$$

Equation 2.9

$$P_\infty = I_z \int_0^{2\pi} \int_0^{\infty} \left[ e^{\frac{-2\rho^2}{\omega_z^2}} \rho \right] \mathrm{d}\rho \mathrm{d}\theta$$

Equation 2.10

$$P_\infty = 2\pi I_z \int_0^{\infty} \left[ e^{\frac{-2\rho^2}{\omega_z^2}} \rho \right] \mathrm{d}\rho$$

Equation 2.11

$$P_\infty = 2\pi I_z \frac{\omega_z^2}{4}$$

Equation 2.12

$$I_z = \frac{2P}{\pi \omega_z^2}$$

Equation 2.13

Where $P$ is the trapping laser power and $I(z)$ is the intensity of the light at the z position.

$$P_{abs} = \sigma_{abs} I_z$$

Equation 2.14

$P_{abs}$ is the total power being absorbed by the trapped particle. $\sigma_{abs}$ is the absorption cross section of the trapped particle calculated for the effective wavelength on the trapping laser. The cross section relies heavily on the refractive indices of the particle and the trapping medium, as shown below.

$$\sigma_{abs} = \frac{2\pi n_m}{\lambda} Im\left[3V_{eff}\left(\frac{\varepsilon_p - \varepsilon_m}{\varepsilon_p + 2\varepsilon_m}\right)\right]$$

Equation 2.15

$\varepsilon_m$ is the dielectric constant of the trapping media and $\varepsilon_p$ is the dielectric constant of the trapped particle. The dielectric constant is related to the refractive index of the material by the equation, $\varepsilon = n^2$. All constants used are specifically for 1064 nm light. V is the volume of the trapped particle, and r is the radius of the particle. Just as in gradient force calculations, the volume is adjusted for the interaction skin depth of the particle material.

$$V_{eff} = 4\pi \int_0^a r^2\, exp\left[\frac{(r-a)}{\delta}\right] dr$$

Equation 2.16

An effective volume, $V_{eff}$, is used to account for the interaction skin depth, $\delta$, of the particle. For gold, $\delta \approx 23\ nm$. The final temperature is predicted by:

$$T = T_\infty + \frac{P_{abs}}{4\pi RC}$$

Equation 2.17

$T_\infty$ is the bulk temperature of the trapping medium and is set to 25$^{O}$C for this model, $C$ is the thermal conductivity of the solvent, and $T$ is the calculated temperature of the solvent at a distance, R, from the surface of the trapped particle.

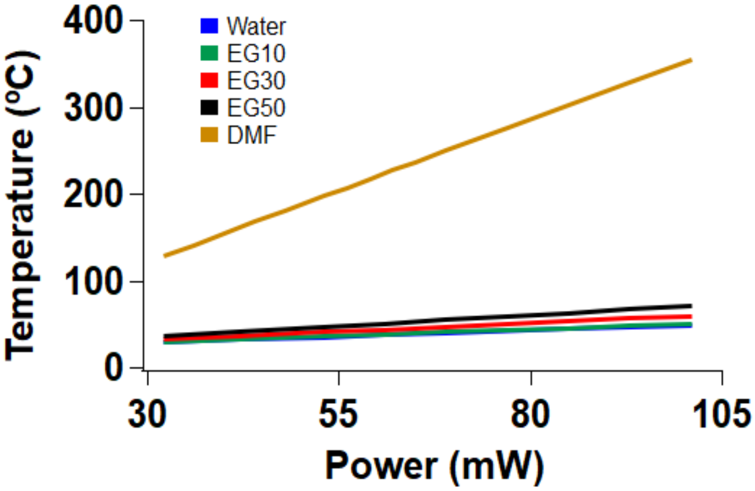

**Figure 2-5** Predicted surface temperatures of an 80 nm gold nanoparticle held in an optical trap 200 nm above the focal plane of the laser.

Next, we measure the diffusion constant value $D$ from the $A$ fit parameter and input the calculated temperature from **Figure 2-5** into Equation 2.3 to calculate a viscosity which is input into Equation 2.2 to determine the stiffness.[69] For each power setting and solvent, we average viscosity and stiffness values determined from at least 10 different Au NPs with a recorded displacement trajectory lasting at least 20 seconds. We note that the resulting viscosities plotted in **Figure 2-6** match the expected viscosity at the calculated temperatures, confirming that our results are self-consistent and properly account for heating effects.

The average stiffness values determined at 32 mW trapping laser power are plotted against the RI of the solvent in **Figure 2-3**C (top) and compared to the model stiffness

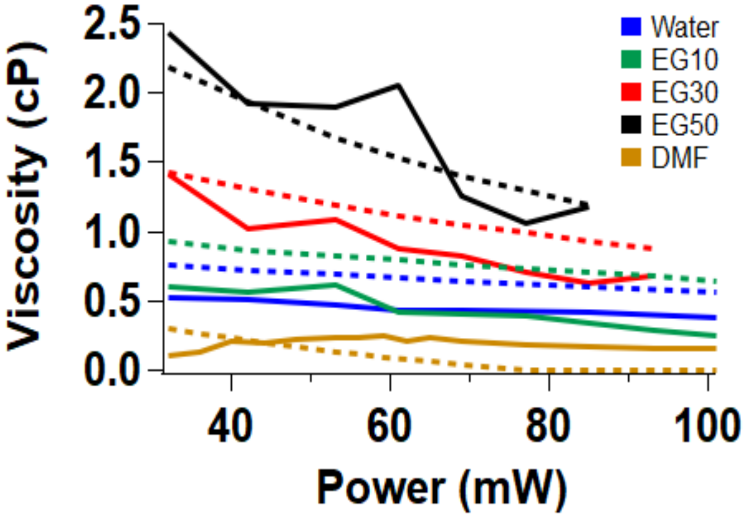

**Figure 2-6** Measured and calculated viscosities for all solvents used in this experiment. Solid lines represent the viscosities determined based on the measured diffusion values. Dashed lines are the viscosities associated with our calculated temperatures. DMF exceeds its boiling point after 45 mW and so viscosity values are based on an extrapolation from lower temperature viscosities.

predictions (bottom). We observe the expected increase in trapping efficiency with RI for water and EG mixtures. Surprisingly, we find that DMF has the lowest stiffness of the solvents in our sample, contradicting the model prediction in Equation 2.1.

**Figure 2-7**A shows the effect of increasing laser intensity on stiffness in all solvents. We observe that in water and EG10, the increase in trapping efficiency is linear, in agreement with Equation 2.1. In all other solvents we observe a significant deviation from expected linear behavior, particularly in EG50 and DMF.[7,76] We note that the deviation from linearity increases concomitantly with the increase in RI of the solvent and becomes more apparent at high trapping laser powers. In EG50 and DMF, there is a dramatic acceleration of stiffness increase just above and below 50 mW of power, respectively. Previously, such superlinear increases of stiffness with laser power have been attributed to unaccounted heating in the trap.[7] However, heating effects are fully corrected for in our measurements here as described above. Furthermore, in DMF where the temperature is highest (**Figure 2-5**), the stiffness becomes supralinear as power increases further. Notably, the stiffness observed in DMF remains below that of lower RI solvents at all powers.

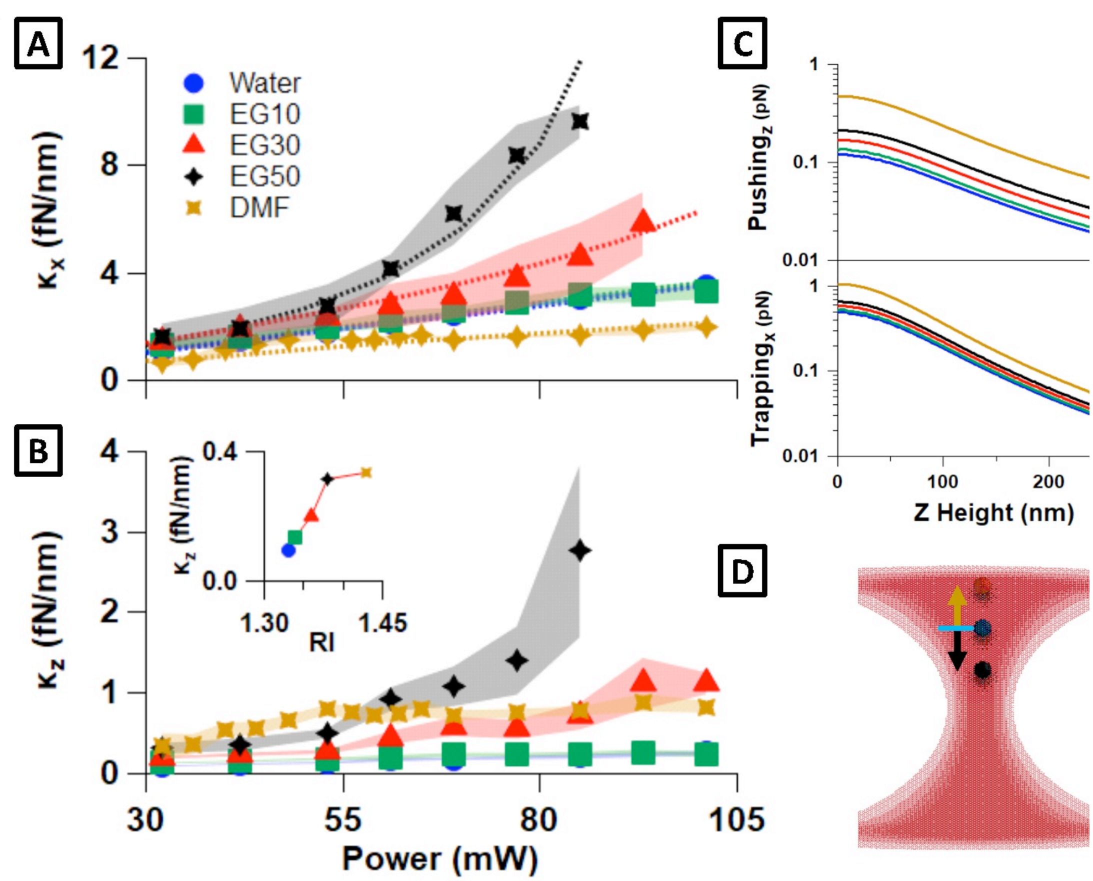

**Figure 2-7** (A) Measured stiffness values in the x direction of an optically trapped, 80 nm gold nanoparticle in various solvents as a function of power. Dashed lines represent predicted stiffness based off models for trapping and pushing forces experienced by a particle in an optical trap. B) z direction stiffness values associated with x stiffness values from (A). Inset shows the trend of stiffness against refractive index at 32 mW trapping power C) Calculated trapping force in the transverse plane (top) and the scattering force in the axial direction (bottom). D) Cartoon illustration of particle equilibrium position in the axial direction in various solvents. In water (blue) the particle trapping position remains fixed regardless of power, while in EG50 (black) and DMF (brown) it is displaced towards and away from the focal point respectively.

Trapping along the laser propagation direction, z in **Figure 2-1**A, is expected to be less efficient due to the pushing forces the particle experiences from backscattering and absorption of laser light.[77] Yet the trapping stiffness along the z direction, $\kappa_z$, should also scale with RI according to Equation 2.1, with high RI solvents showing the most efficient trapping.[78] We measure $\kappa_z$ values and compare to the trends in $\kappa_x$. We construct PSD spectra of particle z-displacements, fit a Lorentzian to extract the corner frequency and use Equation 2.2 to determine the z-direction stiffness, with the diffusion constant, $D$, and temperature, $T$, determined as described above.

The resulting $\kappa_z$ values are plotted in **Figure 2-7**B. We note that trapping efficiency in the z-direction is ~10-fold lower than in the x-direction. In both cases, the stiffness increases with increasing power. For $\kappa_z$, the trends in EG50 and DMF are superlinear and supralinear, respectively. Importantly, $\kappa_z$ scales with RI according to Equation 2.1 as is emphasized in the inset of **Figure 2-7**B which plots $\kappa_z$ measured at 32 mW in all solvents. We observe that $\kappa_z$ in DMF has the highest value, in contrast to the trend in $\kappa_x$.

These results affirm that trapping in high RI solvents like DMF can be more efficient, as predicted. However, many variables vary across solvent conditions and are not accounted for in Equation 2.1. We already showed that varying temperature across solvents cannot explain the trends observed here. Another solvent dependent variable is the pushing force, which is the sum of the scattering and absorption forces on the particle in the trap. It increases with the RI of the medium as shown in Equation 2.31. In water, it was previously reported that the equilibrium between the trapping and pushing forces results in the particle being trapped ~200 nm downstream along the positive $z$ axis from the laser focus.[7,75] We hypothesize that the balance of the trapping and pushing forces may be different depending on the solvent environment and the trapping power.

We calculate both the z-dependent axial pushing and the transverse trapping forces for 32 mW of power as plot them in **Figure 2-7**C, top and bottom respectively. We note that both forces decrease as the distance from the focus along the propagation direction, z, grows. At all z locations, both forces are greatest for DMF as expected. However, the difference between solvents is most pronounced in the pushing force, where DMF shows the highest value by a factor of at least 2. These results suggest that Au NP in DMF may be trapped further away from the laser focus than in lower RI solvents due to increased pushing. Consulting **Figure 2-7**C (bottom), we observe that a particle trapped in DMF at ~300 nm along the z direction would indeed trap more weekly than a particle in water at ~200 nm, in agreement with the trends measured in **Figure 2-7**A. As the power grows, the trapping and pushing forces increase at different rates, resulting in changes in the equilibrium trapping position.

To test these assumptions, we fit Equation 2.30, which describes the z-dependence of the transverse trapping stiffness, to our measured $\kappa_x$ data. Specifically, we use the z-distance as the fit parameter and allow it to change linearly with laser power. We adjust the proportionality constant between laser power and z-distance until good agreement between the model and our stiffness data is achieved at every power setting. The resulting calculated stiffness values are plotted in dashed lines alongside measurements in **Figure 2-7**A. We find excellent agreement of the model with our data for all solvents when z-value changes are incorporated. For water and EG10, no change in z-position is required to achieve a good fit to the data and z=200 nm at all powers as found previously.[7,75] As a result, the stiffness grows linearly with intensity. In contrast, in EG30 and EG50, we find that allowing the particles to move closer towards the focal plane with increasing power produces a superlinear trend matching our observations. Specifically, in EG30 and EG50, the best fit is obtained if the particles start at z=200nm and 210nm, shifting to lower z values at a rate of 0.2 nm/mW and 1 nm/mW, respectively. Finally, in DMF, the particle starts at z=275 nm and shifts *away* from the focus by 1 nm/mW, resulting in a supralinear dependence of stiffness on power, matching the trend in our measurements. We note that predictions fall inside the standard error (shaded regions) with minor exceptions at intermediate power for DMF.

### *2.2.4 TRAPPING FORCE DERIVATION*

The trapping force in an OT scales with refractive index mismatch between the solvent and the material according to:[6]

$$F_{grad} = \frac{|\alpha|}{4} \nabla E^2$$

Equation 2.18

$$\alpha = 3V_{eff}\left(\frac{\varepsilon_p - \varepsilon_m}{\varepsilon_p + 2\varepsilon_m}\right)$$

Equation 2.19

$\alpha$ is the particle polarizability, $\varepsilon_m$is the medium dielectric constant, $\varepsilon_p$is the particle dielectric constant, and $V_{eff}$ is the volume of the particle. The formula, $\varepsilon_m = n_m^2$, relates the dielectric constant to the refractive index.

$$V_{eff} = 4\pi \int_0^a r^2\, exp\left[\frac{(r-a)}{\delta}\right] dr$$

Equation 2.20

An effective volume, $V_{eff}$, is used in Equation 2.19 to account for the field interaction skin depth, $\delta$, of the particle material. For gold, $\delta \approx 23\ nm$. Converting $\nabla E^2$ to a field intensity:

$$\nabla E^2 = \frac{2\nabla I}{c\varepsilon_m}$$

Equation 2.21

$$F_{grad} = \frac{|\alpha|}{2}\frac{2\nabla I}{c\varepsilon_m}$$

Equation 2.22

The intensity for a Gaussian beam is given by

$$I = I_z e^{\frac{-2\rho^2}{\omega_z^2}}$$

Equation 2.23

where ρ is the transverse displacement and $\omega_0$is the beam waist. Taylor expanding the Gaussian around small displacements ρ we get

$$I = I_z\left(1 - \frac{2\rho^2}{\omega_z^2}\right)$$

Equation 2.24

To get the $\nabla I$, differentiate:

$$\nabla I = \frac{d}{d\rho}\left(I_z - \frac{2I_z\rho^2}{\omega_z^2}\right)$$

Equation 2.25

$$\nabla I = -\frac{4I_z\rho}{\omega_z^2}$$

Equation 2.26

Plugging back into the equation for the gradient force at the focus were $z=0$:

$$F_{grad} = -\frac{4|\alpha|I_z\rho}{c\varepsilon_m\omega_z^2}$$

Equation 2.27

We also have that the intensity in the z direction scales with beam waste as:

$$I_z = \frac{2P}{\pi\omega_z^2}$$

Equation 2.28

Where P is the power through the objective. We identify $z = 0$ as the beam focal plane. We calculate a z-dependent beam radius, $\omega_z$, as given in Equation 2.8. Plugging into Equation 2.18:

$$F_{grad} = -\left(\frac{8|\alpha|\rho}{c\varepsilon_m\omega_z^2}\right)\left(\frac{\mathrm{P}}{\pi\omega_z^2}\right)$$

Equation 2.29

$$F_{grad} = -\left(\frac{8\mathrm{P}|\alpha|\rho}{c\pi\varepsilon_m\omega_z^4}\right)$$

Equation 2.30

The light intensity expressions in the gradient force equation are now in terms of the z-height relative to the focal plane, and the distance from z-axis in the transverse plane.

The scattering force is given by:

$$F_{scat} = \frac{n_m \langle S \rangle C_{scat}}{c}$$

Equation 2.31

$\langle S \rangle$ is the time-averaged Poynting vector and c is the speed of light.

We can define the Poynting vector as

$$\langle S \rangle = \frac{2I}{cn_m}$$

Equation 2.32

$$C_{scat} = \frac{k_m^4 |\alpha|^2}{4\pi}$$

Equation 2.33

$C_{scat}$ is the scattering cross section of the particle and $k_m$is the wavenumber whose magnitude is given by:

$$k_m = \frac{2\pi n_m}{\lambda}$$

Equation 2.34

$\lambda$ is the effective wavelength of the trapping laser in the trapping medium.

Resulting in

$$F_{scat} = \left(\frac{C_{scat}}{c^2}\right)\left(\frac{2P}{\pi\omega_z^2}\right)$$

Equation 2.35

$$F_{abs} = \frac{n_m \langle S \rangle C_{abs}}{c}$$

Equation 2.36

The absorption force is given by:

$$F_{abs} = \frac{2IC_{abs}}{c^2}$$

Equation 2.37

$$F_{abs} = \frac{C_{abs}}{c^2}\left(\frac{2P}{\pi\omega_z^2}\right)$$

Equation 2.38

To finally obtain a stiffness of the trap at a given z-height

$$\kappa_\rho = \frac{F_{grad}}{\rho}$$

Equation 2.39

With $\rho$ representing the distance from the central axis in the transverse direction. To evaluate the stiffness plotted in **Figure 2-7**A as a dashed line, we evaluate Equation 2.39 with Equation 2.30 at a value of $\rho = \omega_0/10$.

The summary of these solvent-dependent effects is shown in the cartoon in **Figure 2-7**D. We find here that the equilibrium trapping position along the z-direction is a solvent-dependent parameter affecting measured stiffness in the transverse plane. In low RI solvents like water, Au NPs remain fixed at a near constant distance from the focus as the power increases (blue dot), resulting in a linear increase of stiffness with power. In medium RI solvents, the increase in the trapping dominates the increase in the pushing force, leading to a reduction in z and a superlinear increase of stiffness with power as the particle becomes more strongly trapped as a result of two simultaneous effects (black dot). Finally, in high RI solvents like DMF, the pushing overtakes the trapping force and expels the particles further away from the focus where the beam is more diffuse and trapping is weaker (brown dot). This shift counteracts the effects of higher power on trapping and results in a plateauing of stiffness.

## 2.3 CONCLUSION

In conclusion, using a custom instrument with uniquely combined DF and OT capabilities, we characterize, for the first time, trapping trends of spherical Au NPs in a variety of dispersion media, including the organic solvent DMF, which is commonly used for solution phase chemistry. Our work lays the foundation for single molecule solution phase chemistry experiments and force-detected absorption spectroscopy using OT. We use DF spectroscopy to measure the LSPR fingerprint of individual NPs to determine, unambiguously, that we have trapped only a single NP in various solvents. We find that trap stiffness generally increases with increasing RI of the medium, as predicted by standard models of gradient forces on a dipole in an electric field, but deviates from this trend for DMF. We model the temperature of the solvent near the trapped NP to establish that the temperature increases rapidly with power in organic solvents, where the particle polarizability is high and thermal conductivity low. Nevertheless, these effects alone cannot account for the deviations from expected behavior in our stiffness data. Instead we find that pushing forces resulting from scattering and absorption of the laser light by the trapped NP scale with RI and power and may shift the equilibrium trapping location relative to the focus of the beam. Good agreement with the data is achieved in the model when we allow the particle axial trapping location to vary with solvent and with power in higher RI solvents. These results suggest that differences between solvents may have effects on particle behavior in OT that are not well explained by simple theories of trapping.

We provide a more comprehensive model of trapping than previously used which incorporates both trapping and pushing forces to explain the observed trends. Future work is needed to test these proposals in a wider range of solvent conditions. Overall, our work suggests that Au NPs are effective optical trapping probes in a variety of conditions and opens the possibility of controlled heating and nanoscopic 3D manipulation of metallic NPs in organic solvents. The advances in instrument design and modeling we outline here establish foundations for single molecule force spectroscopy and force-detected absorption spectroscopy for solution phase chemistry experiments using optical trapping and Au NP.

## 2.4 EXPERIMENTAL

We performed all experiments using a 1064 nm Nd:YAG continuous wave (CW) laser for trapping. A white light annular beam illuminates the sample for darkfield (DF) imaging. All parameters are set, and data recorded, using a National Instruments Field Programmable Gate Array (FPGA) device programmed using custom written LabVIEW code. Trapping powers are controllable between 10 – 2500 mW, and the max range for experiments here is between 10 – 110 mW. A high numerical aperture (NA = 1.49) apochromatic oil immersion objective from Nikon (MRD71970) is used to focus the laser for trapping, and the transmitted light is collected by a NA=1.1 condenser and directed towards a quadrant photodiode (QPD) detector. Fluctuations in the QPD signal are recorded at 400 kHz to determine the motion of the trapped nanoparticle (NP) in real time. NPs are imaged using back scattered DF and a 50/50 splitter separates the excitation from the scattered signal, the latter of which is collected by a color camera and spectrometer. To reliably identify and trap single Au NP, we visualize and optically fingerprint them using

DF microscopy and spectroscopy. Au NPs readily scatter light in the visible range based on their localized surface plasmon resonance (LSPR). The LSPR of Au NP is a result of optically excited collective electron oscillation, and is highly sensitive to the particle size, shape and material.[79] By measuring the LSPR of the trapped object, we can confirm the presence of specific particles and discriminate between single and multiple Au NP in the trap (**Figure 2-1**B inset). Under DF illumination, the white excitation light impinges on the sample at wide angles and is scattered by the nanoparticles in all directions.

We use the darkfield spectra to identify and differentiate single particles from doubles or clumps. This capability allows us to unambiguously determine the trapping efficiency of single Au NP with changing media environment. To determine trapping efficiency of the single Au NPs in various solvent environments we measure particle displacements in the z direction according to standard techniques and construct PSD spectra to extract the $f_c$ parameter and determine a diffusion coefficient.

Spherical $80 \pm 3$ nm gold nanoparticles (AuNP), with citrate and polymer functionalization for aqueous and organic environments respectively, are purchased from Nanopartz (#AC11-80-CIT-DIH-100-1 and #E11-80-NPO-META-2.5-0.25).[80] Dispersed citrate-coated NP in water and ethylene glycol (EG) mixtures, and polymer-coated NP in DMF for experiments. Sample chambers are made by adhering a glass cover slip (0.13-0.16 μm) to a glass slide using two strips of parafilm. The chamber is heated to melt the parafilm. After injecting the solution containing NP into the sample chamber, the open edges are sealed with vacuum grease. We observed dissolution of parafilm by DMF, but it is slower than the timeframe of a single experiment. Measurements are performed away from chamber edges and slide surface to prevent edge effects from affecting experiments.

During a given experiment, we performed measurements in each solvent on ten unique particles at a variety of powers. As trapping laser power was increased, irregularities begin to appear, and some outliers were removed. The reported average values include a minimum of five data points. Measurements are frequently performed in water and these averages have as many as twenty points included.

Beginning with the lowest, trapping power is incrementally increased until the particle is naturally ejected from the trap. At each power the trap stiffness is calibrated, and new plasmon scattering spectra are collected. Spectra are used to ensure that only a single particle is in the trap. Stiffness calibrations are performed by oscillating the nanopositioning stage at a set driving frequency (25 Hz), similarly to previous confirmed procedures.[69] Custom analysis code transforms position data to produce power spectral density plots with a characteristic 25 Hz peak. Fitting a Lorentzian curve lets us determine the stiffness of the trap.

# Chapter 3: TUNABLE GROWTH OF A SINGLE HIGH-DENSITY ZIF NANOSHELL ON A GOLD NANOPARTICLE ISOLATED IN AN OPTICAL TRAP

## 3.1 INTRODUCTION

Gold nanoparticle – metal organic framework (AuNP@MOF) hybrid structures have gained popularity in recent years as surface-enhanced Raman spectroscopy (SERS) substrates,[1,2] drug delivery particles,[3,4] gas sequestration systems,[5–7] reaction catalysts,[8–11] and low limit of detection (LOD) sensors.[12–15] In order to push these technologies forward new high precision techniques for controlled growth and characterization of particle structures, optical properties, and physical properties are required. Many synthetic procedures for zeolitic imidazolate frameworks (ZIFs), a widely studied and highly stable class of MOFs, generally achieve crystal growth by heating a reaction mixture in ovens or water baths.[14,16–18] Procedures for encapsulation of gold nanoparticles in ZIF shells, with ZIF-8 as one of the most common, follow similar heating methods and typically result in low density crystals with a high porosity and a greater quantity of interparticle pores, due to small crystals conglomerating to form larger particles.[1,2,8,19,20]

Optical trapping has been demonstrated to be an effective method to isolate and optically characterize nano- and micro-particles in a range of solvent environments.[21,22] In our previous work, we have shown that optical imaging and force signatures of trapped gold nanoparticles can serve as probes of the local chemical environment.[21,22]

Furthermore, gold nanoparticles experience significant heating when in an optical trap (OT) due to absorption of the trapping laser by the nanoparticle.[21–24]

In this report we demonstrate targeted growth of high-density ZIF crystals on the surface of a single, 80 nm diameter, AuNP driven by the high temperatures generated in an OT. We find that by heating AuNPs directly in our OT, we can controllably, selectively, and reproducibly grow ZIFs on the surface of a single AuNP on the scale of seconds. Growth of the crystal is monitored through spectral measurements of the plasmonic darkfield scattering signal and Raman spectroscopy of a single, optically trapped AuNP during the course of growth. We find that the growth of the ZIF crystals is self-limiting to ~50 nm beyond the gold nanoparticle surface due to the temperature gradient surrounding the trapped nanoparticle, and thinner shells can be grown by adjusting the laser power. Our measurements, and modeling, indicate that the refractive index of the grown ZIF-8 crystals is ~1.7. This corresponds to high-density, low-porosity ZIF shells which are not accessible using bulk synthesis methods.[19,25] Finally, we show that our procedure for selective single ZIF shell growth is general and can be applied to a variety of ZIF structures, including ZIF-8,[16] ZIF-11,[16] a ZIF-95 isomorph,[25] and a novel ZIF compound, which are grown with 2-methylimidazole (2-Mim), benzimidazole (Bim), 6-bromobenzimidazole (6-BBim), and 4-tertbutylimidazole (4-TBim) respectively. We also achieved growth with a variety of metallic ions, including $Zn^{2+}$ and $Co^{2+}$, and in several solvents: ethanol, water, and dimethylformamide (DMF). This technique represents a bottom-up growth method for encapsulation of AuNPs with ZIF crystals for which shell thickness can be controlled and monitored during growth. By demonstrating ZIF growth through direct heating of the substrate on the single particle level rather than of the bulk solution, we open the door for controllable engineering and bottom-up assembly of nanoscale objects from molecular building blocks.

## 3.2 RESULTS

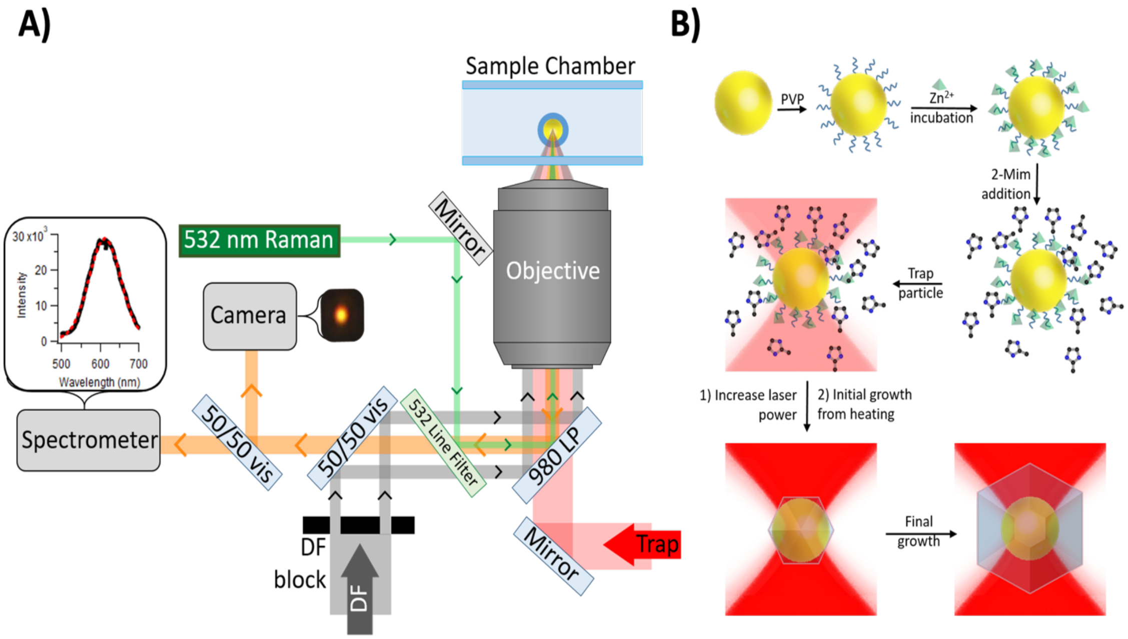
A)
B)
Sample Chamber
532 nm Raman
Mirror
Objective
Camera
30 x10$^3$
20
10
0
Intensity
500
600
700
Wavelength (nm)
Spectrometer
50/50 vis
50/50 vis
532 Line Filter
980 LP
Mirror
Trap
DF block
DF
PVP
Zn$^{2+}$ incubation
2-Mim addition
Trap particle
1) Increase laser power
2) Initial growth from heating
Final growth

**Figure 3-1 A)** Schematic of OT built in an inverted microscope configuration, including DF spectroscopy imaging. Red represents our trapping laser. Gray represents the DF illumination (white light). Green is the input Raman excitation laser (532 nm). Orange is the light scattered back by the nanoparticles. At the objective focus is an optically trapped AuNP coated in a ZIF shell. Insets show a representative plasmon scattering spectra and the associated DF images of the particle. Diagram not to scale. **B)** Mechanism describing encapsulation of optically trapped AuNPs by ZIF-8 to form single-particle, core@shell structures. PVP = polyvinylpyrollidone, 2-Mim = 2-methylimidazole. Diagram not to scale.

We perform experiments using a homebuilt optical tweezer microscope retrofitted with both darkfield (DF) and Raman spectroscopy imaging capabilities.[21] **Figure 3-1**A shows a schematic of the optical trapping instrument used in these experiments. Trapping in the sample chamber is achieved with a 1064 nm continuous wave (CW) laser, coupled with a white light annular beam as the DF illumination source. Raman measurements are performed using a 532 nm excitation beam coupled into the DF illumination path. Backscattered light from the particle is collected simultaneously in both a camera and spectrometer, allowing real time tracking of changes to particle optical properties.[21,26] The trapping laser is used to isolate and manipulate individual AuNPs in the solution. DF illumination enables us to visualize and measure the scattering spectra of the trapped particles. Raman excitation allowed us to chemically fingerprint the material on the surface of the NP. This instrument was discussed in more detail in our previous work. [21]

**Figure 3-1**B is a schematic of the growth process used to generate ZIF nanoshells on AuNPs (Au@ZIF), adapted from known encapsulation procedures.[2,8] Prior to measurements, AuNPs are coated in a polyvinylpyrollidone (PVP) polymer for passivation in organic solvents (e.g. ethanol, DMF) and chelation of metal ions to preferentially nucleate the growth of ZIFs on the surface.[1,2,8,27] PVP enhances affinity of the AuNP for coordination-polymer spheres through interactions between the pyrrolidone rings and the zinc atoms in the ZIF crystal.[28,29] The particle solution is then combined with the chosen ZIF components, such as 2-Mim and zinc nitrate salt ($Zn(NO_3)_2$), after which it is injected into a sealed microscope chamber and positioned at the focus of the optical trapping microscope objective. We rely on DF spectroscopy and optical trapping force signatures to reliably trap only single AuNPs, approximately 10 μm above the glass coverslip surface inside the chamber.[21] Once the particle is trapped, the laser power is increased to 50 mW or higher, causing the trapped AuNP to heat up as we and others have shown previously.[21,22,24]

## 3.3 GROWTH OF ZIF

Darkfield illumination is used to locate particles, which are then directed towards the trapping laser position by adjusting the nanopositioning stage position. Upon trapping, we begin collecting spectra at 100 ms acquisition per scan over the spectral range of 496.184 nm – 702.815 nm. Spectra are collected continuously until the particle becomes unstable in the trap and is ejected or 500 seconds has passed. We attribute the ejection to an increased scattering cross section due to growth of the crystal on the AuNP, resulting in an increased repulsive force from the trapping beam. This procedure can be repeated within the same sample cell for at least two hours. At longer times, we observe free

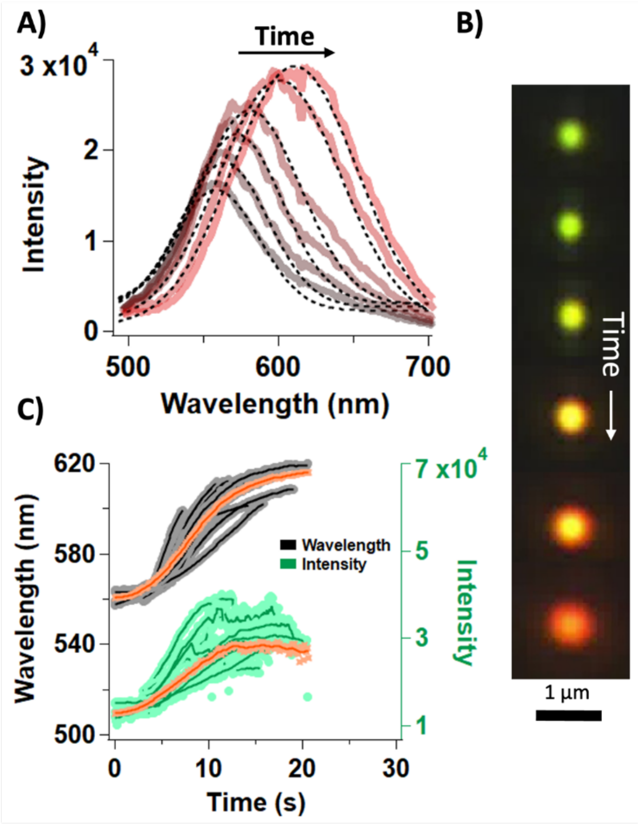

**Figure 3-2** **A**) DF spectra collected following heating of an optically trapped, 80 nm AuNP in ethanol in the presence of ZIF-8 precursors. The gray curve is measured immediately after laser power increase which precipitates heating and the red curve is measured 15 seconds later, with a few intermediate spectra also shown. Gaussian fits to the spectra are plotted in dashed black **B**) Camera images corresponding to the spectra in 2A. **C**) Intensity (green, right axis) and peak wavelength (black, left axis) as extracted from Gaussian fits to the raw spectra plotted against time elapsed since heating onset. Data corresponding to 18 individual AuNP is plotted here and is representative of the full data set collected in ethanol. Data corresponding to curves in 2A is highlighted in orange.

floating ZIF crystals interfering with measurements. In the case of higher precursor concentrations (**Figure 3-5**), small ZIF crystals form in the background and interfered with experiments.

ZIF-8, which is grown from 2-Mim and $Zn(NO_3)_2$ as shown in **Figure 3-1**B, has been extensively characterized and serves as a proof-of-concept for the growth technique presented here. **Figure 3-2**A shows six representative DF spectra of the same optically trapped, 80 nm diameter, AuNP. The spectra are each a 100 ms scan collected at various times within 25 seconds after the onset of heating in the trap. In this case, growth occurs in the presence of ZIF-8 precursors at a concentration of 1 mM 2-Mim and 0.33 mM $Zn^{2+}$. The curves in **Figure 3-2**A are drawn from a larger dataset of spectra collected for each particle during growth at a rate of 10 Hz, with 100 ms acquisition times, shown in the **Figure 3-4**. The initial spectrum (black) in **Figure 3-2**A, taken immediately after the particle becomes trapped and heated, peaks at 560 nm as measured by a Gaussian fit (dashed lines), which is consistent with expectations for the scattering spectra of a bare 80 nm AuNP, indicating no growth prior to measurements. Subsequent spectra peak positions shift towards longer wavelengths and higher amplitudes. **Figure 3-2**B shows camera images captured simultaneously with the six spectra in **Figure 3-2**A, demonstrating the color change. No color change is observed on other particles flowing freely in solution in the same chamber. We also observe a broadening of the spectra in **Figure 3-1**A after the onset of heating, suggesting a deposition of material on the surface which leads to energy transfer from the nanoparticle to the surface layer and a damping of the plasmon response.

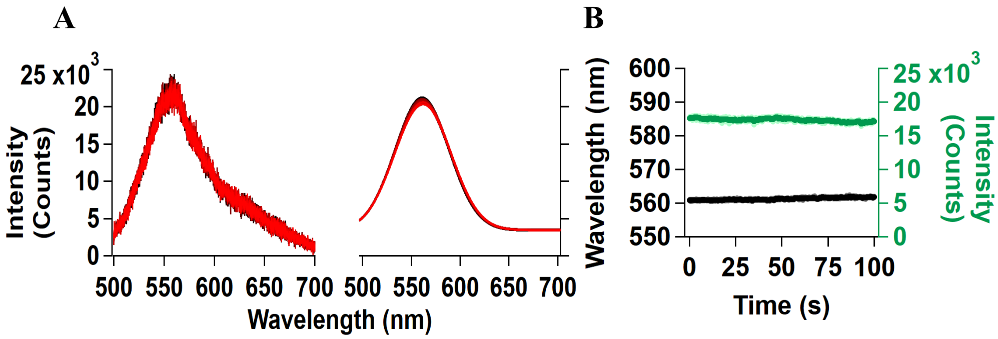

**Figure 3-3 A)** Control measurement DF spectra collected following heating of an optically trapped, 80 nm AuNP in the presence of 2-methylimidazole dispersed in ethanol. **B)** Plot of the peak wavelengths (left, back) and associated intensities (right, green) against time.

We attribute variations in spectra to differences in the number, and location, of crystal nucleation sites on the surface of an AuNP, as well as small variations in growth rates resulting in imperfect spheres.

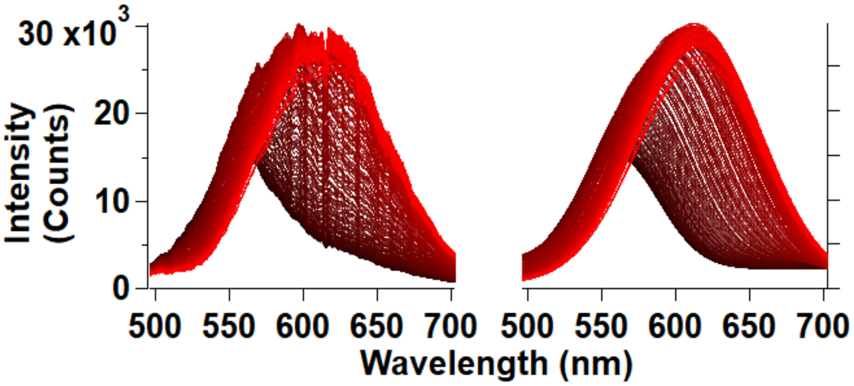

**Figure 3-4** Plots of a full time sequence for the data presented in Figure 2A and 2C where dark curves represent the initial spectra and red represents the final spectra. Left is the raw data collected by the spectrometer, and the right is the Gaussian fits to those same lines.

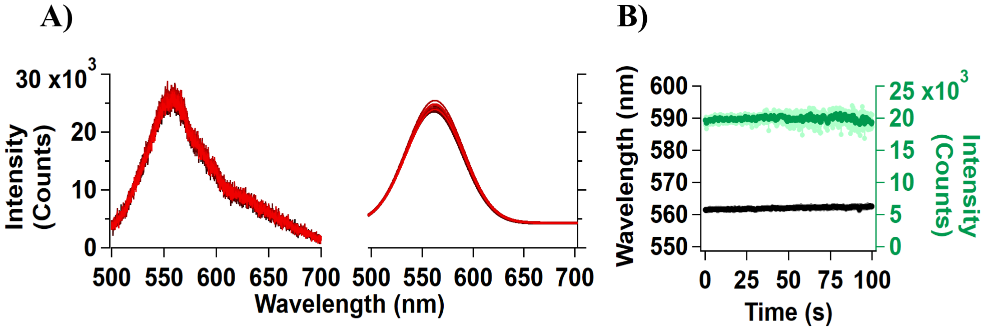

**Figure 3-6** **A)** Control measurement DF spectra collected following heating of an optically trapped, 80 nm AuNP in the presence of in $Zn(NO_3)_2$ ethanol. **B)** Plot of the peak wavelengths (left, back) and associated intensities (right, green) against time.

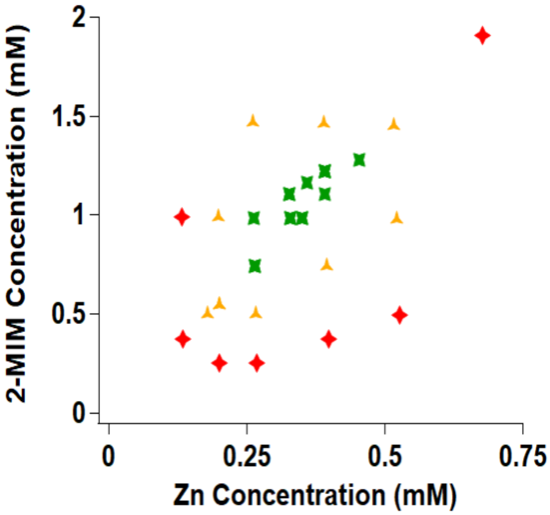

**Figure 3-5** Plot of the $Zn^{2+}$ and 2-MIM concentrations used in experiments. Found the best use concentration ratio of the two precursors to be 3:1, Mim:Zn. Green points represent concentrations that yielded steady and reproducible growth of ZIF-8 crystals on the surface of the gold. Yellow points represent concentrations that either resulted in growth that was restrictively slow or had small ZIF-8 crystals form in the solution background. Red represents concentrations where either no growth was observed, or an excessive number of ZIF-8 crystals grew in the background.

To capture the evolution of DF spectra, we fit the curves in **Figure 3-2**A and **Figure 3-4** with a Gaussian function. In **Figure 3-2**C we plot the peak wavelength (black) and intensity (green) against time elapsed for 18 individual AuNPs trapped and heated at time 0 in the presence of ZIF-8 precursors. The end of the traces marks the point when the particle falls out of the trap. We observe that both wavelength and intensity increase sharply within ~5 seconds of heating onset and approach an asymptote within 25 seconds, indicating no further changes after this time. No similar change of the DF spectra was detected when one or more of the ZIF-8 precursors was missing from the solution, as show in **Figure 3-6** and **Figure 3-3**. Growth on trapped particles was achieved in a narrow range of concentrations of the precursor materials as shown in **Figure 3-5**. Once growth on one particle was complete, it was released from the trap and another particle captured to repeat the growth protocol.

### *3.3.1 CHOOSING PRECURSOR CONCENTRATIONS*

**Figure 3-5** shows various concentration pairs of ZIF-8 precursors in the final mixture used to initiate growth. We determined that the optimal ratio of 2-Mim:$Zn^{2+}$ in these experiments is approximately 3:1. The concentrations in the final mixture used throughout the main manuscript is 1 mM:0.33 mM (2-Mim:$Zn^{2+}$). Our 3:1 ratio agrees with a previously reported encapsulation procedure,[32] but differs from the 1:1 ratio found in procedures for bulk ZIF-8 crystal growth.[81] All other ZIF crystals were grown using the same 1 mM:0.33 mM concentration and ratio of imidazole derivative to metal ions. In water, there is also a concentration of ~10 mM TEA in the final reaction mixture as suggested by Khan et al.[82]

## 3.4 RAMAN SPECTRA COLLECTION

Raman spectra are collected while the ZIF crystal is growing on the AuNP surface. A particle is guided into the trap, followed by introducing the Raman excitation beam, which has been aligned to match the trap focal position. Raman measurement are

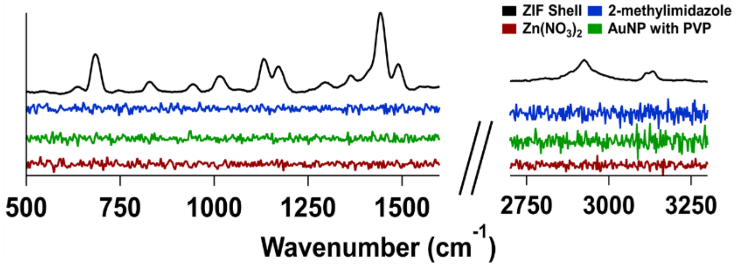

**Figure 3-7** Raman measurement using a 532 nm excitation beam, with a 1 min acquisition time, performed on a single, optically-trapped, 80 nm AuNP in the presence of PVP polymer (green), 2-Mim (blue), Zn(NO$_3$)$_2$ salt (red), and a ZIF-8 crystal grown on the surface (black). A fully labeled ZIF Raman scattering spectra is presented in **Figure 3-8**.

performed using a 532 nm excitation beam, with a 1 min acquisition time, on a single, optically-trapped, 80 nm AuNP during crystal growth. A long exposure time is necessary because the Raman excitation power must be kept low (<50 mW before objective) so as not to destabilize trapped nanoparticle, and because only a quarter of the signal is reaching the spectrometer due to the presence of two 50/50 splitters. Long-pass Raman line filter is used to filter out the excitation beam (Semrock part #BLP01-532R-25). This filter prevents detection of signal below 540 nm (~400 cm$^{-1}$ shift from excitation). Zn-N stretches are expected to be between 150 – 300 cm$^{-1}$, so we are unable to detect them in the current system.[83,84]

**Figure 3-7** shows a Raman spectrum (black) of a trapped particle, with both the 2-Mim and the Zn precursor present, acquired over one minute after crystal growth was initiated. Peak positions agree well with literature reports for ZIF-8 crystal Raman shifts.[7,18] Control experiments performed on optically trapped bare AuNPs (not shown), AuNPs with polymer functionalization (green), AuNPs in the presence of only Zn$^{2+}$ precursor (red), and AuNPs in the presence of only the imidazole precursor (blue), showed no detectable signal as evident in **Figure 3-7**. These results indicate that the observed Raman signal is due to a crystal shell grown at the surface of the AuNP, rather than from free floating precursor molecules.

## 3.5 PLASMON RESONANCE SPECTRA

Spectra are analyzed in IgorPro using custom written code. A Gaussian curve is fit to the spectra in order to determine a peak wavelength and intensity. In part A of **Figure 3-10** to **Figure 3-13**, the left plot in the raw spectra measurement, and the right is the Gaussian fits for that data. These figures demonstrate that growth is achieved in a variety of solvents. Spectra are collected sequentially at 10 Hz at 100 ms acquisition times over the spectral range of 496.184 nm – 702.815 nm.

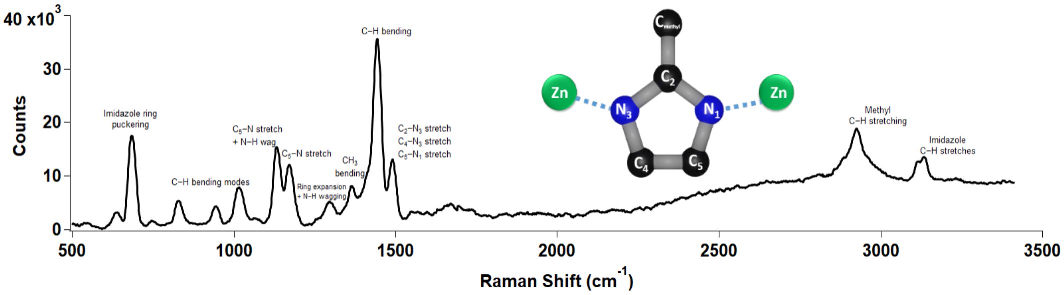

**Figure 3-8** Raman spectra of ZIF-8 grown in the optical trap. Peaks identified by comparison to reported values.[5,6] Inset cartoon shows the organic linker, 2-Mim, bound to $Zn^{2+}$ metal ions as would be found in the ZIF-8 crystal.

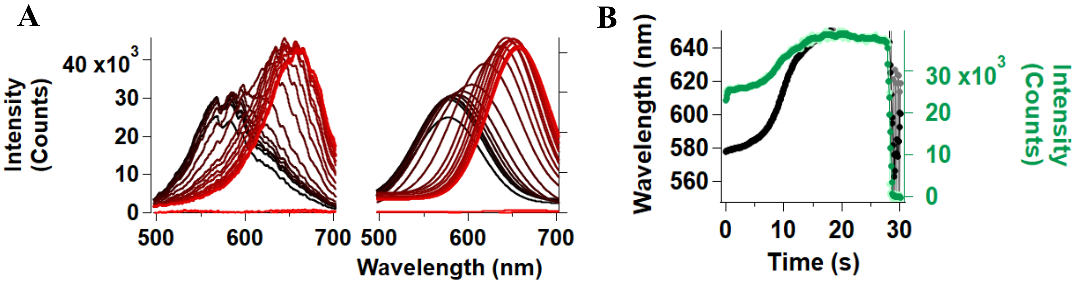

**Figure 3-9 A)** DF spectra collected following heating of an optically trapped, 80 nm AuNP in the presence of ZIF-8 precursors, 2-methylimidazole and $Zn(NO_3)_2$ in DMF **B)** Plot of the peak wavelengths (left, back) and associated intensities (right, green) against time.

Raman signal is due to a crystal shell grown at the surface of the AuNP, rather than from free floating precursor molecules.

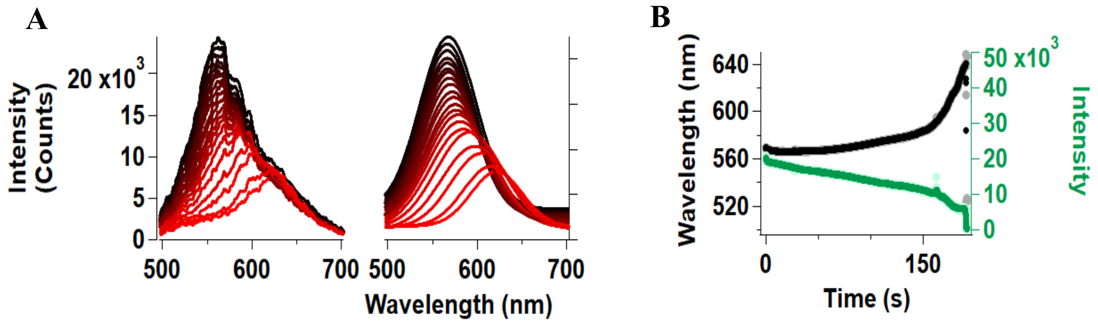

**Figure 3-10 A)** DF spectra collected following heating of an optically trapped, 80 nm AuNP in the presence of ZIF-8 precursors, 2-methylimidazole and Zn$(NO_3)_2$ in DMF exhibiting decreasing intensity. **B)** Plot of the peak wavelengths (left, back) and associated intensities (right, green) against time.

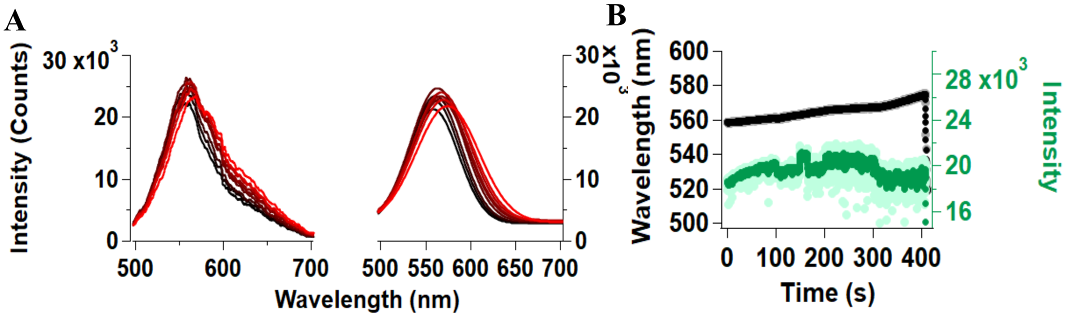

**Figure 3-11 A)** DF spectra collected following heating of an optically trapped, 80 nm AuNP in the presence of ZIF-67 precursors (Co$(NO_3)_2$ and 2-methylimidazole) in ethanol. **B)** Plot of the peak wavelengths (left, back) and associated intensities (right, green) against time.

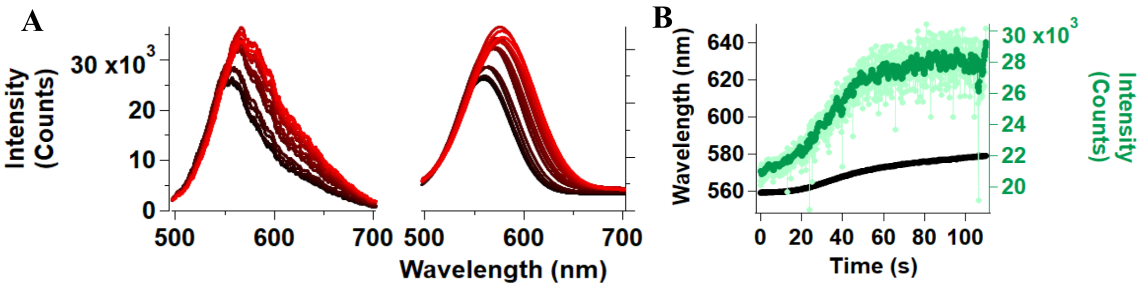

**Figure 3-12 A)** DF spectra collected following heating of an optically trapped, 80 nm AuNP in the presence of Co$(NO_3)_2$ and 4-tertbutylimidazole in water **B)** Plot of the peak wavelengths (left, back) and associated intensities (right, green) against time.

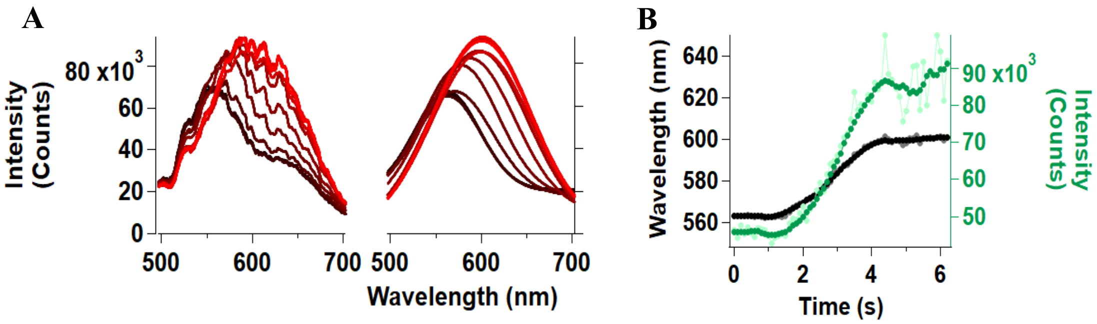

**Figure 3-13 A)** DF spectra collected following heating of an optically trapped, 80 nm AuNP in the presence of ZIF-8 precursors, 2-methylimidazole and $Zn(NO_3)_2$ in water. **B)** Plot of the peak wavelengths (left, back) and associated intensities (right, green) against time.

The red shifting of the DF spectra observed in **Figure 3-2** for the particle is consistent with encapsulation of nanoparticles with ZIF structures.[1,2] The growth of the crystal around the AuNP replaces the solvent, such as ethanol with a refractive index of n=1.35 for 1064 nm light,[30] to create an environment with a new refractive index. As a result, the plasmon resonance of the composite particle detected in the far field red shifts relative to a bare AuNP. While all experiments presented in our main figures are performed in ethanol with $Zn^{2+}$ metal ions, we also achieve ZIF-8 growth in water and dimethylformamide (DMF) and find a similar red shifting trend regardless of solvent used (shown in **Figure 3-9-Figure 3-13**). Additionally, we demonstrated successful growth of ZIF crystals using $Co^{2+}$ metal ions which also show a redshift (shown in **Figure 3-12** and **Figure 3-11**). To characterize the density and porosity of the ZIF shells grown here, we model the scattering cross sections of Au@ZIF composite particles in MATLAB using the MNPBEM17 package designed for simulating plasmonic nanoparticle-light interactions.[31] The model parameters use data from McPeak et al. for the wavelength dependent refractive indices of gold across the visible spectrum,[32] ethanol as the solvent ($n_{560}$=1.36),[30] and an adjustable refractive index for the growing ZIF shell. Prior measurements of ZIF-8 crystal refractive indices range from 1.28, to 2.6.[1,5,19,33–36] Cookney et al. reports indices ranging from 1.54-1.58 in their high density ZIF-8 crystals, which are grown using a layer by layer growth method.[19] **Error! Reference source not found.**A shows modelled scattering cross sections for an 80 nm AuNP with increasing crystal shell thickness with a refractive index of n=1.58, following the indices presented by Cookney et al.[19] We observe that a modelled shell thickness of 200 nm or greater produced broad scattering profiles, without a clear resonance peak (**Error! Reference source not found.**A and **Figure 3-14**).

## 3.6 Loss of Distinct Peak

Calculated the scattering cross sections of core@shell Au@ZIF particles using MATLAB package MNPBEM17.[85] As the shell thickness is increased, the scattering

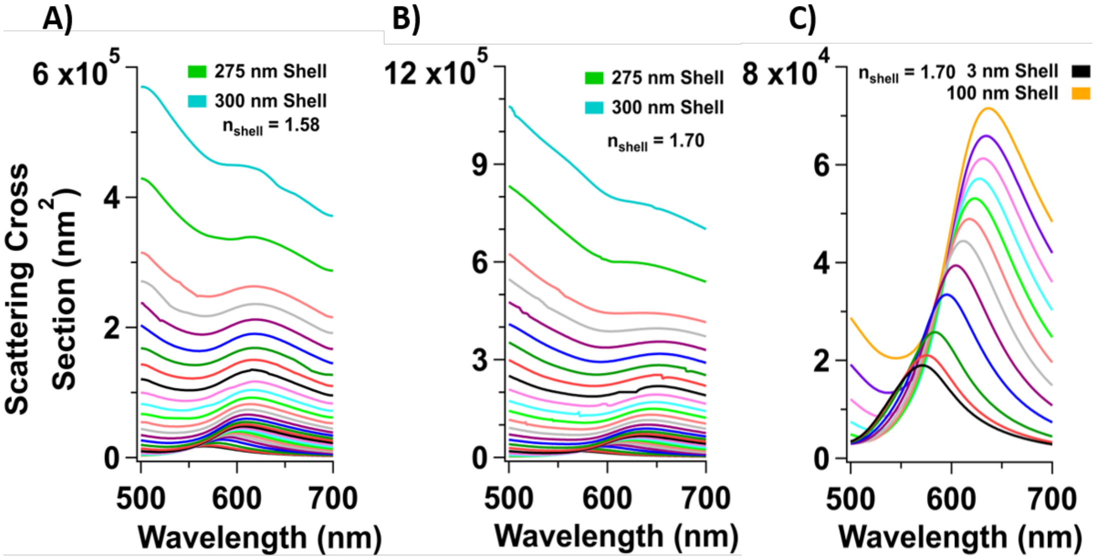

**Figure 3-14** Model calculations of the scattering cross section of an 80 nm AuNP in ethanol for different thickness ZIF shells. **A)** Calculation shell with refractive index n=1.58 as listed by Cookney et al. **B)** Calculation shell with refractive index n=1.70 to agree with measured data. **C)** A zoom in of **B** to emphasize the difference in peak shape between thin shell scattering and thick shell scattering.

resonance peak is predicted to broaden and red-shift. For thin shells (<100 nm) there is a clear peak that fits well to a Gaussian. For intermediate thicknesses (>100 nm, <250 nm) the peak begins to broaden significantly and lose the distinct Gaussian peak profile. For the thickest shells (>250 nm) the resonance peak has significantly diminished and has almost completely disappeared in the higher index calculation shown in **Figure 3-14**A and **Figure 3-14**B respectively. **Figure 3-14**C is a zoom in of **Figure 3-14**B on the thinnest shells to emphasize the difference in scattering profile between the thickest and thinnest shells we modelled.

This is distinct from our experimental measurements, as shown in in Figure 2A. Furthermore, our model (**Error! Reference source not found.**A) shows that the magnitude of the calculated scattering cross section, which is proportional to the measured signal intensity, increases monotonically with shell thickness. In contrast, the experimental data in **Figure 3-2**B plateaus after an initial growth period. These results together suggest that shell growth will not reach 200 nm in thickness.

We use our model to estimate the refractive index of the grown ZIF nanoshells. Figure 4B shows modelled data of the expected peak wavelength for different ZIF shell refractive indices. As expected, the peak red shifts with increasing shell thickness, and then begins to plateau for thicknesses above 100 nm. A double exponential fit line is used to describe the modeled wavelength data. We observe good agreement with experimental measurements only with higher index values. It should be noted that for thin shell thickness, small changes to the shell result in large changes in wavelength as shown in **Error! Reference source not found.**B. This illustrates that observed deviations in wavelength would result from very minute changes in the ZIF crystal thickness. Consulting **Figure 3-2**B, we identify n=1.58, as providing a reasonable fit to our data. These results strongly suggest that the ZIFs grown in our experiments are high density crystals which are distinct from products of bulk-synthesis growth characterized by lower refractive index values of n≈1.4.[19,25]

## 3.7 HISTOGRAMS OF CRYSTAL GROWTH

Final 3% of the data points for each particle prior to ejection from the trap is binned to determine an average final wavelength. Colors here match up to the colors used in the main manuscript: 2-Mim (green), 4-TBim (orange), Bim (purple), and 6-BBim (blue). Left plots the histogram for final wavelengths. The right is the histogram for final intensities. Solid curves are Gaussian fits to the histograms.

To demonstrate that this procedure for growing high quality Au@ZIF structures is general and applicable to other ZIF variants, we repeat the single NP ZIF growth procedure illustrated in **Figure 3-1**B in the presence of 2-Mim and three alternative imidazole derivatives, which are shown in **Figure 3-15**A alongside 2-Mim (green): 4-TBim (orange), Bim (purple), and 6-BBim (blue). In **Figure 3-15**B and **Figure 3-15**C we show representative scattering spectra and intensity trajectories, respectively, of a single trapped AuNP recorded in the presence of each molecular precursor and $Zn^{2+}$ at 50 mW of laser power. In all cases, we observe a red shift of the scattering spectra and an increase in intensity followed by the signal plateauing. However, the final asymptote values of wavelength and intensity vary somewhat between the ZIFS. For example, we find that, on

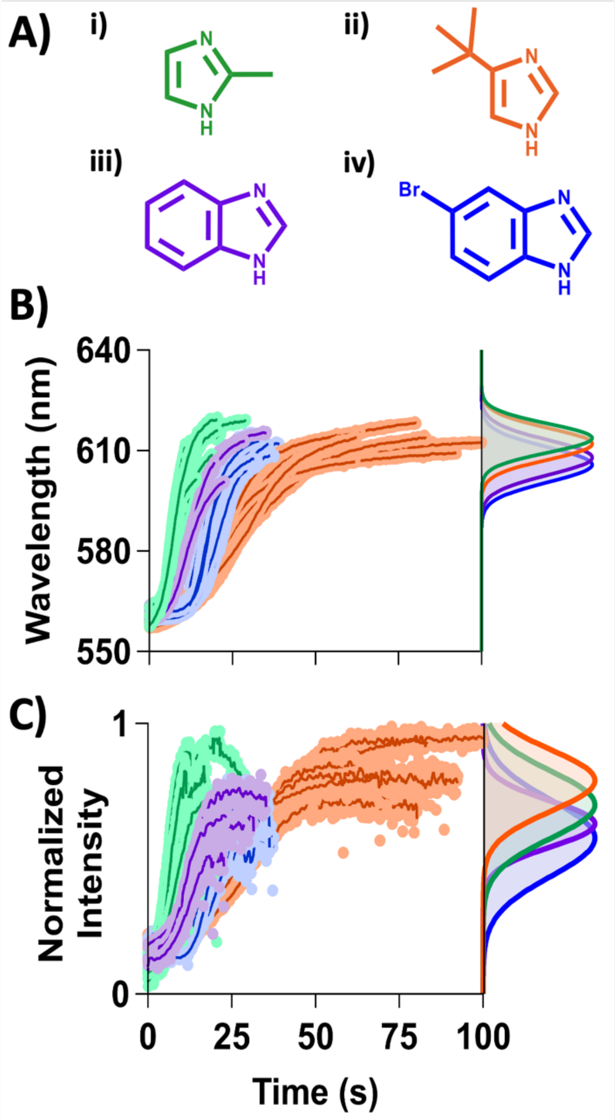

**Figure 3-15** **A)** Chemical structure of the different imidazole compounds used to grow ZIF crystals. (i) 2-Mim, (ii) 4-TBim, (iii) Bim, and (iv) 6-BBim. **(B)** Plot of the peak wavelength **(C)** and intensity against time after laser power increase. Color corresponds to the precursor used and are illustrated in (A). On right are Gaussian fits to histograms of the last 3% of the plotted data for each particle. The histograms for both wavelength and intensity are presented in **Figure 3-17**.

average, crystals grown from the substituted imidazole variants 2-Mim, and 4-TBim both reach scattering wavelength of ~615 nm, and the ZIFs grown with the large Bim and the variant 6-BBim reach lower values of ~605 nm. These patterns imply a lower refractive index with larger organic precursors, indicating a lower density crystal, and thus positive correlation between the size of the organic linker and the size of the pores in a MOF.[5,37] Our results here are consistent with prior measurements showing that the pore size in ZIF-11 (Bim) is 26% larger than that in ZIF-8 (2-Mim) crystals, as well as having a 19% decrease in metal ion density per unit volume.[16]

To our knowledge, the ZIF grown with 4-TBim, has not been reported previously.[38] Our measurements here are the first to probe its growth dynamics and porosity relative to other ZIFs. In the case of ZIF-8, most particles grow within the first 20 seconds of being exposed to the trapping laser. The more sterically hindered 4-TBim grows slowest, saturating within 75 seconds. The tertbutyl group is a large steric group, and our data suggests that it is reduces the rate of crystal growth, but minimally impacts its optical properties in comparison to 2-Mim. Shells grown using 4-Tbim reach a final wavelength that is similar to that of ZIF-8, although it takes longer to plateau. From these observations, we conclude that the crystal has a similar density to ZIF-8, but a slower growth rate.

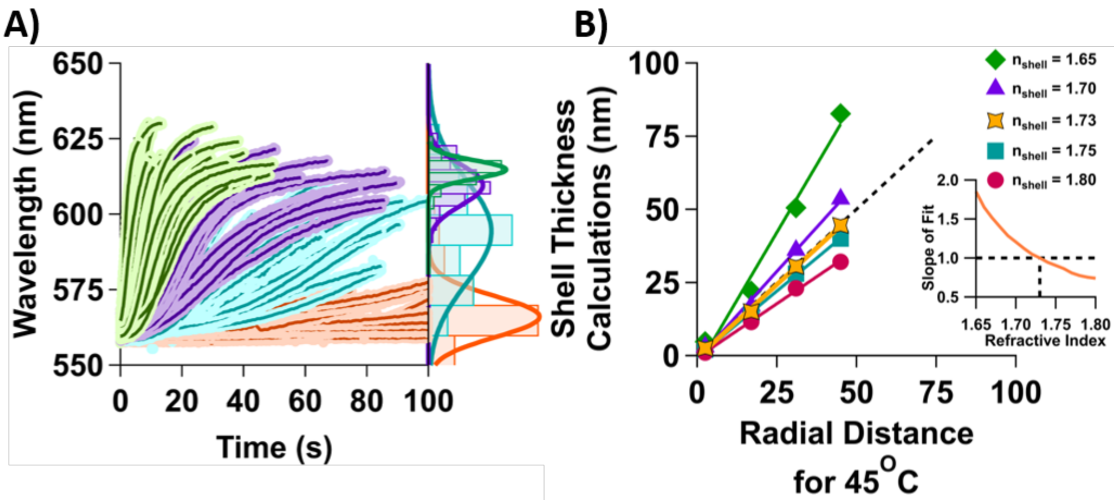

**Figure 3-16** **A)** *Left*: Testing the growth of 4-TBim on an 80 nm AuNP at different trapping laser powers. 30 mW (orange), 40 mW (blue), 50 mW (purple), and 60 mW (green). *Right*: Gaussian fits for histogram of the final wavelength achieved during growth illustrating average final wavelengths 30 mW (568 nm), 40 mW (595 nm), 50 mW (611 nm), and 60 mW (622 nm). Histograms are of the last 3% of data from each particle. **B)** Plotting the shell thickness predicted from plasmon scattering cross section calculations against the radial distance that the particle is predicted to be above 45 ºC. Inset plots the slope of each fit line against its corresponding refractive index to illustrate which refractive index shell agrees best with our expectation. This occurs at n ≈ 1.7.

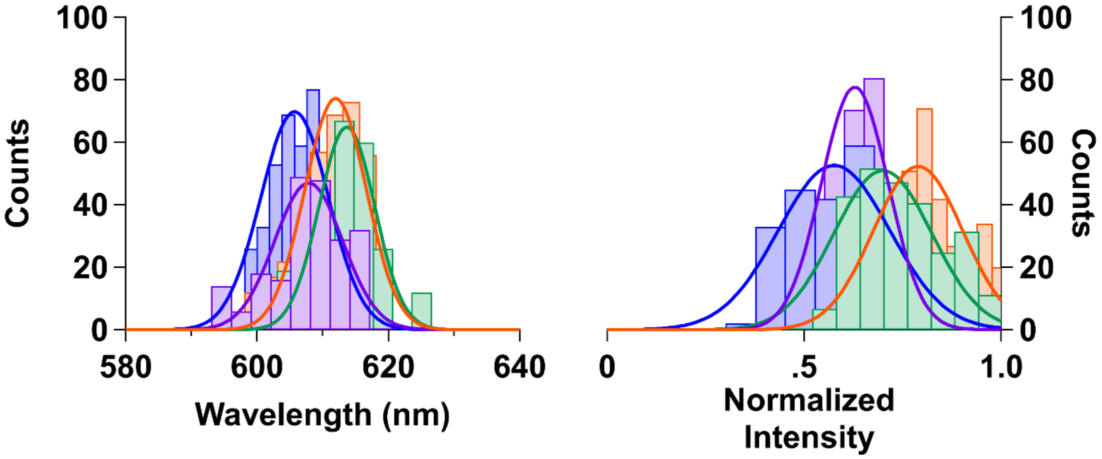

**Figure 3-17** *left*) Histogram of the max wavelengths measured during growth. *right*) Histogram of the max intensities measured during growth.

The slower growth rate of 4-Tbim offers additional experimental control to examine dynamics and properties of crystal growth with changing laser power. **Figure 3-16**A presents experimental results for growth of 4-Tbim ZIF crystals when held in the optical trap at different trapping laser powers: 30 mW, 40 mW, 50 mW, and 60 mW of trapping laser power. We can see a clear dependence on the trapping laser power of both the rate of growth and the final peak scattering wavelength. For 30 mW of power the average scattering signal shifted by only ~10 nm in 100 seconds, indicating little to no growth. As the power increased, the growth accelerated, and the final saturation wavelength red shifted. At our highest power, 60 mW, we can see that growth saturates within ~10 seconds at a final wavelength of 622 nm.

## 3.8 HEATING OF GOLD NANOPARTICLES

We model the temperature near the surface of an optically trapped AuNP as previously reported.[7,54] The results are reproduced here in **Figure 3-18**. Briefly, we determine an absorption cross section for an 80 nm AuNP and calculate the local temperature as a function of distance from particle surface when it is placed in a uniform electro-magnetic field of varying intensities. The identity of the solvent, in particular its thermal conductivity, determines the temperature profiles and average temperatures around the particle. Here, we model heating in ethanol to correspond to our experimental conditions.

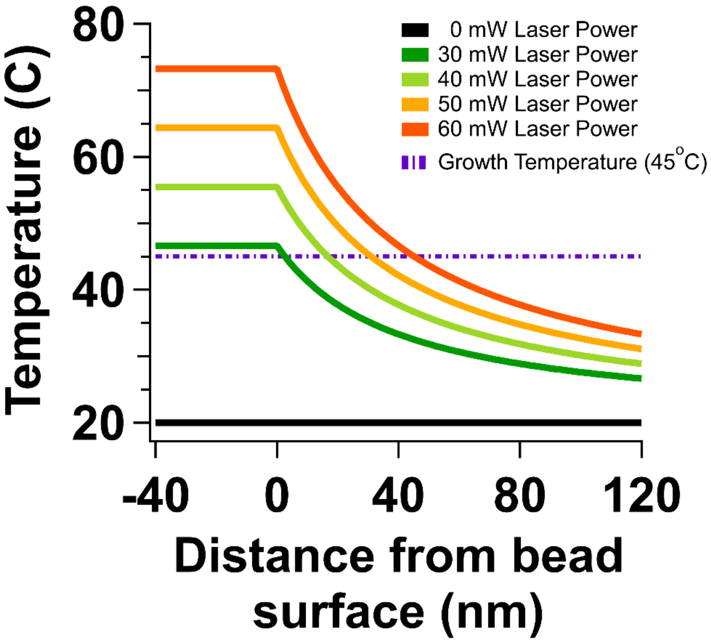

**Figure 3-18** Showing the temperature decays for temperatures associated with powers used in figure 6 of main paper. Calculation for an 80 nm diameter AuNP in a sharply focused optical trap, located 200 nm above the focal plane in ethanol as the solvent. Black line represents room temperature, or a 0 mW trap. Purple dashed line is 45 °C which we claim to be the cut-off temperature for driving growth with this technique.

This dependence on power suggests that the growth is self-limited by the maximum temperature at the surface of the AuNP. Using heating models for the temperature near a nanoparticle surface,[21,22] we estimate shell thickness in post processing analysis. We and others have shown previously that the surface temperature of the AuNP and the rate of temperature decay into the solution scales with trapping laser power (**Figure 3-18**).[21,22] At 30 mW of trapping laser power, the AuNP surface temperature reaches 46.5 °C, decaying to 45 °C within ~3 nm, while at 50 mW the surface reaches 64 °C, decaying to 45 °C within 31 nm. Experimentally, we observe almost no growth at 30 mW, suggesting that ~45 °C is the threshold condition for ZIF growth, which is similar to temperatures used in previously reported encapsulation procedures.[2,8] As the trapping power is increased, the region around the particle where temperatures exceed 45 °C extends to further radial distances (**Figure 3-18**), allowing for thicker ZIF shell growth. We can estimate the thickness of the ZIF shells grown at each power setting by comparing the average measured asymptotic wavelength to our scattering cross section model shown in **Figure 3-14**B. In **Figure 3-16**B, we plot this extrapolated thickness from the model in **Figure 3-14** against the radial extent of the regions corresponding to $T \geq 45$ °C. The y=x line is indicated in dashes. These results for 4-TBim confirm the growth of high-density crystals with $n \approx 1.7$, which is significantly higher than for ZIF crystals grown in bulk synthesis. Importantly, this is the first report of a ZIF grown from this 4-TBim precursor and our results here indicate that its shell thickness can be finely tuned by surface temperature via laser power modulation.

## 3.9 CONCLUSION

In this work, we demonstrate a new technique for controllably growing high density ZIF crystals on the surface of a single isolated AuNP and characterize ZIF material properties and growth dynamics using purely optical techniques. We first show that optically trapping an AuNP in the presence of ZIF precursors will result in significant and reproducible changes to the particle plasmon scattering spectra. Our observations imply that a new material is displacing the solvent near the surface of the AuNP. We perform a Raman scattering measurement, in tandem with growth, in the presence of 2-Mim and $Zn(NO_3)_2$ precursors, and confirm that a ZIF-8 crystal encapsulates the trapped AuNP under these conditions. We then successfully grow crystals using different imidazole derivatives of varying molecular size: 2-Mim, 4-TBim, Bim, and 6-BBim. ZIF shells grown from these compounds follow the expected trend of larger molecule yielding less dense crystals, as confirmed by the relative red shifts of their scattering spectra. In all cases, the grown crystals exhibit a markedly higher refractive index ($n \approx 1.7$) than in crystals grown using bulk methods, indicating that we achieve higher density ZIFs using our directed single particle heating method. Significantly, the ZIF grown using 4-TBim has not been reported previously. Here, we find that shell thickness can be reliably controlled by adjusting the incident laser power of the trapped Au NP.

The technique of localized heating for directed ZIF growth developed here raises the prospect of achieving custom designed particle shapes and surface morphologies for applications such as SERS substrate preparation, gas sequestration, and catalytic site design. While the yield in these experiments is limited to a single particle at a time, the fine-tuned control demonstrated here suggests that we could design and build custom nanoscale to mesoscale structures from individual particles as building blocks. We demonstrate controlled growth of distinct materials using four different organic linkers combined with two different metal ion centers in three different solvent environments. These successes suggest that this technique can be expanded to accommodate any MOF for which temperature can drive growth. Further experiments are needed to determine the range of possible substrate materials (gold, silver, aluminum, etc.) and other MOF nanoshells materials.

## 3.10 EXPERIMENTAL

### *3.10.1 Materials*

Gold nanoparticles (80 nm, AuNPs) are obtained from Nanopartz (#AC11-80-CIT-DIH-100-1). Polyvinylpyrolidone (PVP)(#PVP40-50G), zinc nitrate hexahydrate (#228737-100G), 2-methylimidazole (2-Mim)(#M50850-100G), benzimidazole (Bim) (#194123-5G), 6-bromobenzimidazole (6-BBim)(#702188-1G), 4-tertbutylimidazole (4-TBim)(#CBR01595-1G), ethanol (#1117270500), dimethylformamide (DMF)(#D4551-250ML), and water (#W4502-1L) are obtained from Millipore Sigma. Glass slides (#260202) and coverslips (#260341) are obtained from Ted Pella.

## 3.11 PROCEDURE

### *3.11.1 PREPARATION OF PRECURSOR SOLUTION*

Precursor solutions are prepared based on previous literature procedures.[32,86] For growth in ethanol—the condition primarily used in this manuscript—we prepared 25 mM $Zn(NO_3)_2{\cdot}6H_2O$ (0.0372 g, $1.25 \times 10^{-4}$ mol) solution in 5 mL of ethanol, and 50 mM 2-Mim (0.0205 g, $2.5 \times 10^{-4}$ mol) solution in 5 mL of ethanol. In water experiments, triethylamine was added to the 2-Mim precursor solution at a concentration of 0.25 M to help drive the reaction.[87]

### *3.11.2 FUNCTIONALIZING AUNPS WITH PVP*

AuNPs are coated with PVP by adapting a previously reported procedure.[86] Briefly, gold nanoparticles are dispersed in 19.5 mL of ethanol and 500 μL of a 25 mg/mL PVP solution is added to the mixture. The solution is left to stir under room temperature for 24 hours. This process replaces citrate stabilizer on the AuNPs with PVP molecules. Sample is centrifuged at 7500 rpm for 15 minutes, and then decanted. The following wash is then performed 3 times: (i) disperse AuNPs in 1 mL of ethanol; (ii) sonicate sample for 30 seconds and vortexe for 30 seconds, until no visible clumps remain; (iii) centrifuged7 minutes at 9000 rpm and remove supernatant; (iv) after final wash, disperse AuNPs in the desired solvent. Storing in water results in the longest shelf life, of at least 3 months. In other solvents (e.g. ethanol and DMF), we observe NPs sticking to the edge of the tube and non-dispersible clumps falling out of solution after a few weeks.

### *3.11.3 COMBING GOLD AND PRECURSORS*

PVP AuNPs is dispersed in 100 mL of solvent and $Zn^{2+}$ precursor solution is added and vortexed for 10 seconds to combine. The solution is left to sit for 5 minutes. PVP acts as a chelating agent and helps retain $Zn^{2+}$ ions near the surface. Attempts to grow ZIF without PVP were unsuccessful. 2-Mim solution is added to mixture. The solution is vortexed for 10 seconds to combine mixture. Growth of ZIF nanoshells can be performed immediately after addition of 2-Mim.

### *3.11.4 SAMPLE PREPARATION*

After the mixture is prepared, 50 µL of solution are injected into a sample chamber made up of a glass coverslip adhered to a glass slide with parafilm. Slide is placed in the optical tweezer instrument above an NA=1.45 oil immersion objective. Schematic of instrument shown in **Figure 3-1**A.

# Chapter 4: SINGLE ENTITY DARK-FIELD AND FORCE SPECTROSCOPY MEASUREMENTS OF NANOPARTICLE DIMERS REVEAL TRANSITIONS FROM THE CLASSICAL TO THE QUANTUM REGIME

## 4.1 INTRODUCTION

Optical trapping (OT) allows isolation of single metallic nanoparticles or nanostructures in solution and analysis their behavior away from surfaces or defects. As shown in the previous chapters, single nanostructures can be manipulated in 3D with nanometer resolution, selectively heated and tracked via force and optical spectroscopy.

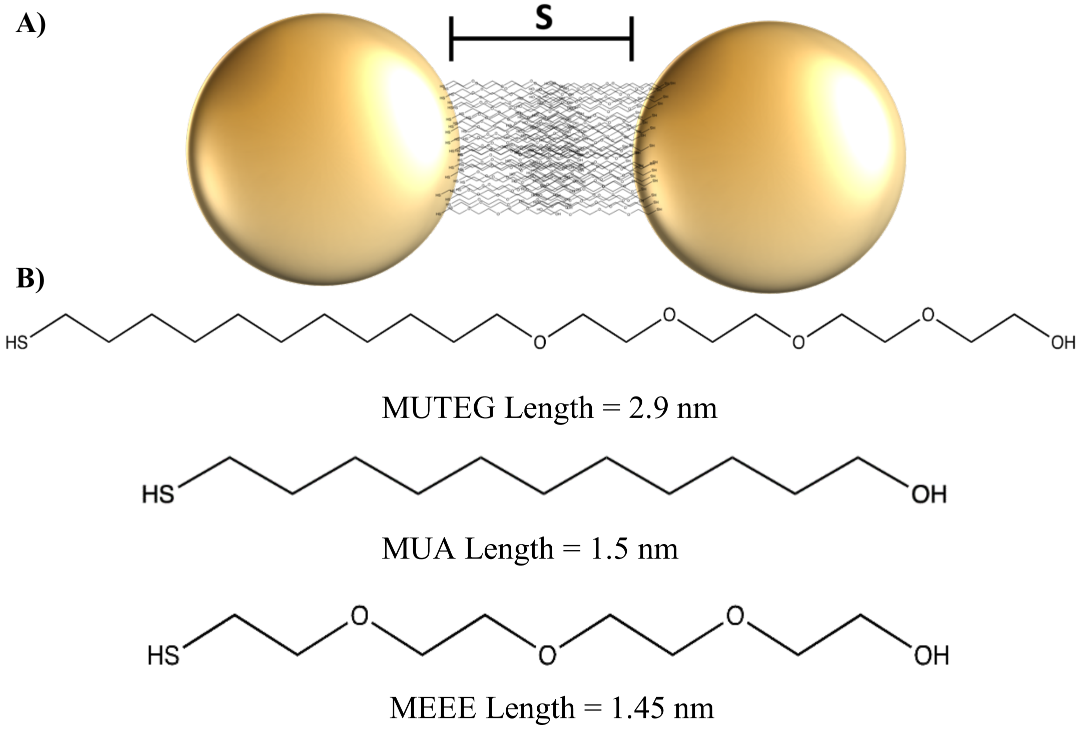

**Figure 4-1** A) Basic nanoparticle dimer system. Two gold nanoparticles are separated by a distance s and linked together by short polymer chains. B) Structures of the molecules used to dimerize gold nanoparticles. From top to bottom, (11-mercaptoundecyl) tetra(ethylene glycol) (MUTEG), 11-mercaptoundecanol (MUA) and , 2-{2-[2-(2-mercaptoethoxy) ethoxy]ethoxy}ethanol) (MEEE)

Here, we leverage these tools, to experimentally manipulate and study the dynamics and structure-property relationships of gold nanoparticle (AuNP) dimers. **Figure 4-1**A illustrates a basic AuNP dimer system used here with some separation, *s*, between spherical nanoparticles (NPs). WE investigate the distinct properties of AuNP dimers formed eith three different hydrocarbon chains, shown in **Figure 4-1** B. The hydrocarbon chains are functionalized with a terminal thiol to adhere to, and form a monolayer on, the gold surface. The polymer strands on separate particles interact with each other to form dimers.[88] We confirm that AuNP dimers orient their long axis parallel to the trapping laser polarization, allowing for selective spectra along various axes of the dimer. [89–91] This 3D control allows us to quantify dimer LSPR and to apply the plasmon ruler equation to study the distribution of inter-particle distances created with different hydrocarbon chains. We find that by tuning intermolecular interactions, we can manipulate the average inter-particle separation, s. Furthermore, we find that heating the individual dimers, results in gradual separation and final decoupling of the dimer into the constituent monomers. This unique dynamic control allows us to not only identify and distinguish the classical plasmon coupling regime from the quantum charge transfer plasmon, but to also observe the evolution of dimer structures between these distinct states as the inter-particle distance grows. These techniques and results are particularly relevant for applications requiring precise control over nanoparticle spacing, such as in the development of nanoscale sensors and devices.

## 4.2 RESULTS AND DISCUSSION

The optical trapping instrument used in these experiments has been previously described in detail.[54,55] In brief, the optical trap consists of an inverted optical microscope coupled with DF microscopy and spectroscopy to manipulate and characterize metallic NPs. Backscattered light is simultaneously collected by a camera to monitor the contents of the trap and by a spectrometer to determine the exact plasmon scattering spectra of the trapped nanostructure.

Dimers are prepared from 45 nm AuNPs according to published protocols, using a short monothiol hydrocarbon chain, 11-mercaptoundecanol (MUA), shown in **Figure 4-1**.[88] The dimers are easily differentiable from single nanoparticles by their plasmon scattering resonance recorded using darkfield spectroscopy performed simultaneously with trapping. The scattering resonance along the longitudinal access of the dimer is red shifted relative to the original monomer resonance by an amount that depends on the separation distance between the two spherical AuNPs.[43,88,92–95] Here, we quantify the red shift , $\Delta\lambda$, relative to the monomer resonance, $\lambda_0$, for individual dimers suspended in solution with an OT coupled with polarized white-light illumination. The relative polarization angle between the trapping laser and the white-light illumination can be controlled in our instrument as shown in **Figure 4-2**A(i) and B(i). Like nanorods, we find that trapped dimers orient along the direction of the trap polarization and can be made to rotate relative to the white-light excitation.[89,91] When the excitation illumination is oriented along the short, or long, axis of the dimer, the observed scattering maximum corresponds to the resonance peak of a single spherical AuNP or to a dimer signature, respectively. **Figure 4-2**A and B, part i) show the polarization of the DF illumination (white) relative to the polarization of the trapping laser (red) and to the dimer orientation. Part ii) shows camera stills of the same optically trapped NP when the DF polarization is oriented perpendicular

(A) or parallel (B) to the white light laser. The green and red color in the two images corresponds to the transverse plasmon mode peak centered 550 nm and the longitudinal plasmon mode at ~660 nm in this case, as determined by a double Lorentzian fit to the spectra taken at distinct angles Θ. These are shown in **Figure 4-2**C, where we demonstrate the change in scattering signal as the polarization of the DF illumination relative to the

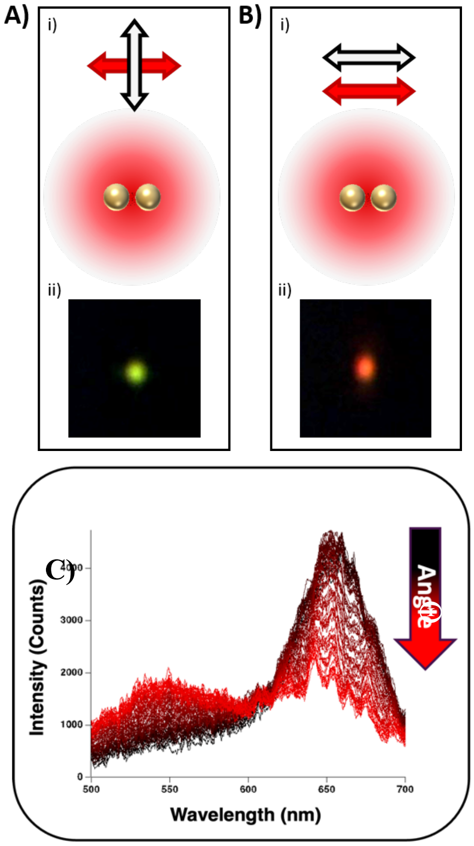

**Figure 4-2: A)** Shows the transverse plasmon of our optically trapped AuNP dimers. i) Illustration of the DF polarization relative to trapping laser. Transverse plasmon activated when illumination perpendicular to trapping laser. Top-down illustration of the trapped dimer orientated parallel to the laser polarization. ii) Image captured of an optically trapped dimer under conditions described in i). **B)** Shows the longitudinal plasmon of our optically trapped dimers. i) Illustration of the DF polarization relative to trapping laser. Longitudinal plasmon activated when illumination parallel to trapping laser. ii) Top-down illustration of the trapped dimer orientated parallel to the laser polarization. iii) Image captured of an optically trapped dimer under conditions described in i) and ii). **C)** Polarization dependent scattering spectra of a single dimer. Going from black to red, we rotate the polarization of the DF illumination to go from parallel with the longitudinal axis (0°) to perpendicular with the longitudinal axis.

trapping laser is rotated gradually from $0^{o}$ to $90^{o}$, as defined by **Figure 4-2**A and B, respectively. In the $90^{o}$ geometry, the monomer signature is nearly completely absent, and a single Lorentzian peak provides a good fit for quantifying dimer resonance. We conclude, that by manipulating the polarization of the DF illumination, we can probe all angles of the dimer in space.

### *4.2.1 QUANTIFYING DIMER SEPARATIONS PREPARED USING DISTINCT MOLECULAR LINKERS*

To infer a dimer geometry from the measured LSPR, we use the plasmon ruler equation, which is an established model for extrapolating the separation between two nanoparticles from the measured plasmon resonance wavelength shifts.[94,96,97] **Figure 4-3Figure 4-3** A) Modelled scattering cross sections of a dimer where each curves represents a different particle separation. As the dominant peak blue shifts, the separation between the particles is increasing. B) The peak positions of the modelled curves from A. C) Experimental data of dimer peaks collected using three different linking molecules. Green is MUTEG, orange in MEEE, and purple is MUAA shows modelled scattering cross sections of an NP dimer consisting of two 45 nm diameter spherical AuNPs with separations ranging from 0 nm to 22.5 nm calculated using the MNPBEM17 toolbox for the simulation of metallic nanoparticles in Matlab.[98] We define plane wave, simulating the DF illumination, as parallel to the longitudinal axis of the AuNP dimer. The wavelength of light was varied in 3 nm steps from 500 nm to 800 nm to cover a range relevant for a gold nanoparticle plasmon resonance. We use the peak wavelengths determined in our model for different particle separations to generate a plasmon ruler equation following previously

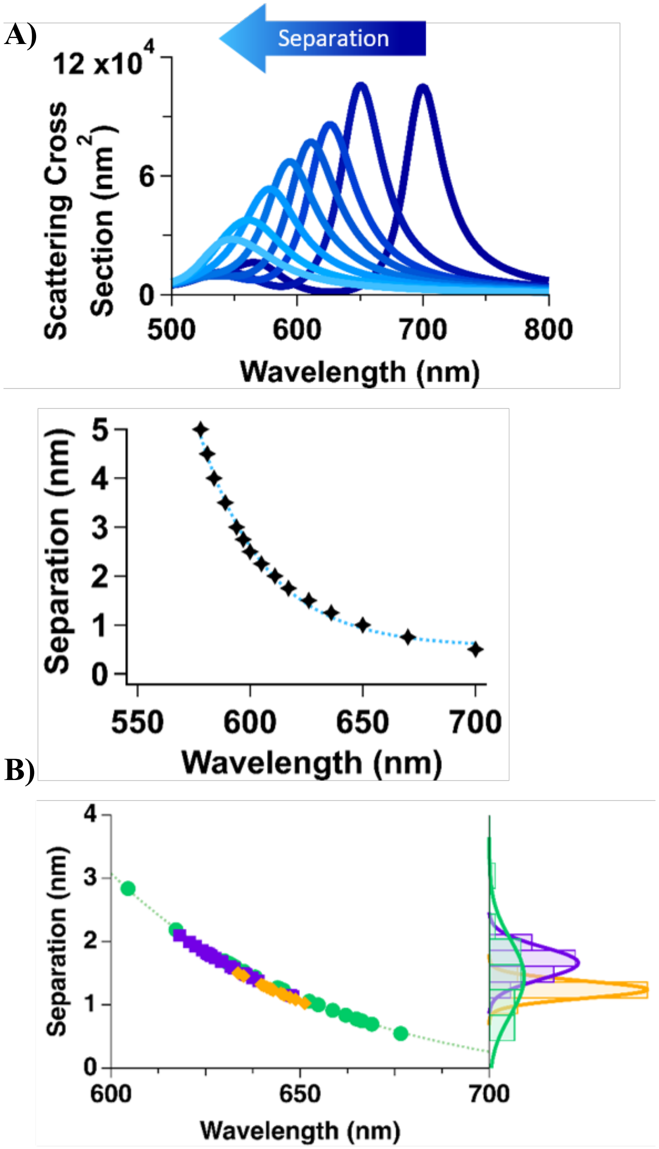

**Figure 4-3** A) Modelled scattering cross sections of a dimer where each curves represents a different particle separation. As the dominant peak blue shifts, the separation between the particles is increasing. B) The peak positions of the modelled curves from A. C) Experimental data of dimer peaks collected using three different linking molecules. Green is MUTEG, orange in MEEE, and purple is MUA.

reported procedures.[99,100] By comparing the plasmon resonance of a spherical AuNP monomer to the longitudinal plasmon mode of the AuNP dimer, we are able to plot the ratio of the difference between the two resonance peaks (Δλ) over the monomer resonance wavelength ($\lambda_o$). **Figure 4-3 A)** Modelled scattering cross sections of a dimer where each curves represents a different particle separation. As the dominant peak blue shifts, the separation between the particles is increasing. **B)** The peak positions of the modelled curves from A. **C)** Experimental data of dimer peaks collected using three different linking molecules. Green is MUTEG, orange in MEEE, and purple is MUAB shows the ratios found using our model plotted against particle separation. By fitting an exponential to the simulation data we produce the formula

$$\frac{\Delta\lambda}{\lambda_0} \approx 0.037 + 0.249e^{-0.523s}$$

where $\lambda_o$ is the plasmon resonance of a 45 nm diameter AuNP monomer, Δλ is the difference between the longitudinal axis resonance and the single monomer resonance ($\lambda_o$), and $s$ is the separation distance in nanometers between the two AuNPs. [99,100] The exponential fits well for separations between 1-10 nm but deviates from the modelled values outside this range as consistent with previous reports.[93,99,101,102] Specifically, at separations above ~10 nm (~25 % of particle diameter), the dimer spectra become indistinguishable from the monomers and Δλ→0. Importantly, on the other extreme, at very close separations quantum effects dominate and the plasmon ruler equation no longer applies.[102–104]

To vary the inter-particle distance in solution, we prepare dimers with three different linking molecules illustrated in **Figure 4-1** B: 11-mercaptoundecanol (MUA) as before, but also with (11-mercaptoundecyl) tetra(ethylene glycol) (MUTEG), and 2-{2-[2-

(2-mercaptoethoxy) ethoxy]ethoxy}ethanol) (MEEE). **Figure 4-3**C (right) shows a histogram of measured plasmon spectra of at least 16 distinct dimers prepared with each polymer. We compare these measured dimer resonances to the plasmon resonance of the AuNP monomer to obtain a value for $\frac{\Delta\lambda}{\lambda_0}$ and use the plasmon ruler formula to extract the inter-particle separations, as shown in **Figure 4-3**C. We find that the three polymers result in dimer with distinct separation profiles. Dimers linked with MEEE show the tightest spread of LSPR corresponding to separations narrowly centered on 1.25 nm. MUTEG linked dimers show the widest range of separations, centered at 1.44 nm but spanning from as short as 0.55 nm to as long as 2.8 nm. MUA has an intermediate spread in separations, but the longest average wavelength, centered at 1.67 nm.

These differences in separation cannot be attributed to differences in polymer length alone. For example, MUA and MEEE are chains with the same number of atoms and differ only in their atomic composition. Instead, we observe that the oxygen containing MEEE molecule tends to have short separations, while the primarily carbon MUA molecules have a reltively longer separations. PEG chains, such as MEEE, are known to passivate and not interact strongly with the gold surface.[105] We conclude that the measured difference in interaparticle separations of MEE and MUA-linked dimers found here is due to the varying strength of intermolecular forces (IMFs) between individual molecules. The MUTEG molecule is twice the length of the other two molecules, and we osberve that it has the broadest range of separations as expected given the greater number of conformations it can adopt in solution, such as bending back on itself. The strong IMFs between individual MUTEG polymers can result in dimers with short separations, while other NUTEG linked dimers maintain longer separations due to the fully extended MUTEG linkers in the inter-particle gap.

### *4.2.2 Controlling Dimer Separation Distance through Heating*

In **Figure 4-4**A we present a subset of data collected from a single optically trapped AuNP dimer linked by MUTEG while the trapping laser power is increased at a rate of ~10 mW/second. The spectra are collected at a rate of 48 frames per second (20 ms acquisition time). In **Figure 4-4**B, we plot the peak resonance of the longitudinal plasmon mode (black points) determined by fitting a double Lorentzian to the spectra. We apply our plasmon ruler equation to the measured peak wavelength to calculate the separations (blue points). We have previously shown that AuNP heat up when trapped in water using higher laser power, as shown in **Figure 3-18**. [7,54] Here, we observe that upon reaching a certain power threshold (e.g. approximately 300 mW for MUTEG bound NPs) the longitudinal dimer resonance undergoes a rapid blue shift, indicating an onset of separation between the

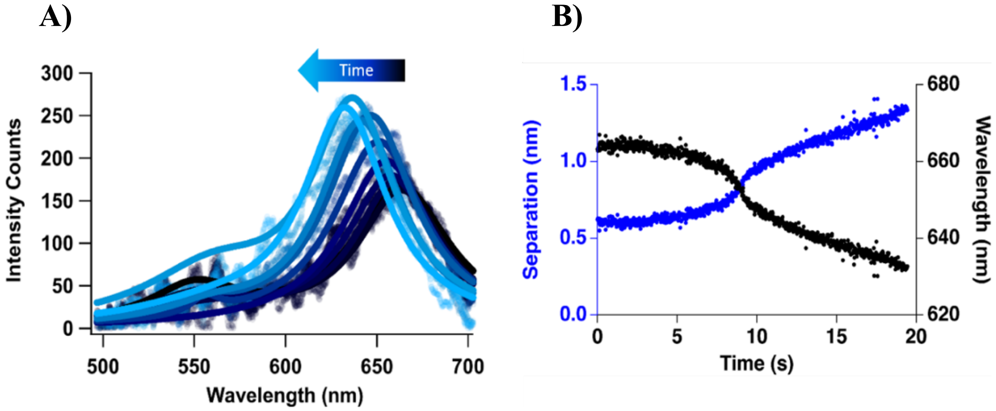

**Figure 4-4** A) Experimentally measured scattering spectra of an optically trapped gold nanoparticle. Time is increasing as we go from the darkest curve in the back to the light blue curve in the front. Measurements were collected over a period of 20 seconds with 25 ms acquisition times. B) The black curve shows the peak wavelengths found by fitting a double Lorentzian curve to the measured spectra on the left. The blue curve shows the calculated separations determined from those measured peak wavelength values.

dimerized NPs. [5,19] These results are consistent with a “melting” process beyond a temperature threshold, which results in release of intermolecular forces between the linking molecules. In the specific dimer shown in **Figure 4-4** we observe an overall wavelength shift from 670 nm to 635 nm, which corresponds to an increase in NP separation distance from 0.6 nm to 1.4 nm. After separation occurs, the spectrum reverts to the monomer resonance signature (not shown), indicating that the heating process does not damage the NPs. The separation of dimers through heating implemented here, affords unprecedented control in real-time over inter-particle separations. We observe, for example, that the separation process can be halted at an intermediate distance before a final rupture occurs by reducing trapping power to maintain the newly established separation.

We leverage this control over dimer distances to study the dynamics of dimer separations during heating and to probe the plasmon response. Several example MUTEG dimer spectra recorded during heating are shown in **Figure 4-4** and **Figure 4-5**A-C. The most common evolution of the dimer LSPR we observe is represented in **Figure 4-4**A and **Figure 4-5**A. In this case, the initial spectrum contains a dominant peak near 650 nm, which we attribute to the longitudinal plasmon mode, which gradually blue shifts until the monomer resonance at ~550 is established, indicating a continuous elongation of interparticle separation, s, and a final rupture into the constituent monomers. We note that 650 nm resonance corresponds to ~1 nm in inter-particle separation. A similar phenomenon is observed in the dimer in **Figure 4-5**B, where the dimer spectrum continuously decreases and blue-shifts during the heating processes. Here, however, the starting resonance below

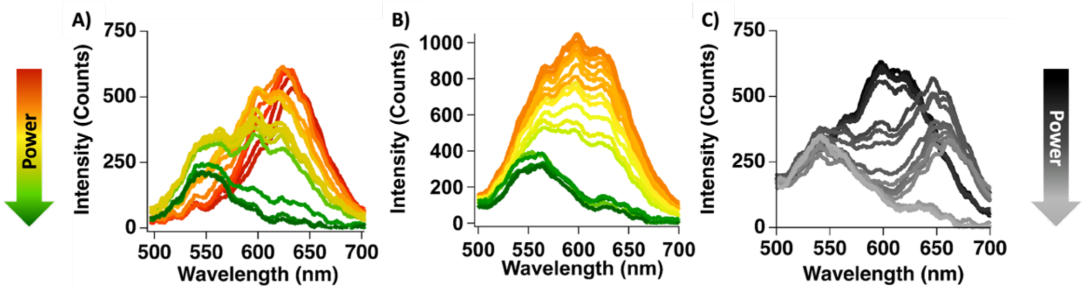

**Figure 4-5** Each plot represents a single optically trapped gold nanoparticle dimer as the laser power is gradually increased. Scans were collected at 20 Hz with 50 ms acquisition times. A) shows a case where the spectra originally peaked at 600 nm, redshifted towards 650 nm, and then fell apart. B) Shows an example where the peak started centered at 600 nm and gradually decayed down to the monomer resonance. C) Shows a case where the resonance originally peaked at 640 nm and gradually blue shifted until separating into the monomers

650 nm corresponds to a longer distance of >1 nm between the nanoparticles in the dimer, which grows until the point that the dimer linkage breaks.

A markedly distinct behavior occurs in the dimer spectra shown in **Figure 4-5**. Here, the initial peak resonance is at 595 nm, which is similar to the initial resonance in **Figure 4-5**B. However, as heating begins, the peak first red shifts to 650 nm (~0.5 nm separation) before blue-shifting to 550 nm. This final resonance at 550 nm indicates that separation into monomers occurred in this case, as in other dimer examples. However, the dynamics as modeled by the plasmon ruler equation, indicate a closing of the inter-particle gap during heating, which is inconsistent with the dimer rupture we observe. A dominant peak that is blue shifted relative to the classically expected longitudinal plasmon peak has previously been attributed to a charge transfer plasmon (CTP).[102,104,106] This plasmon mode begins to appear when NPs are less than 1 nm apart and becomes dominant over other modes below 0.5 nm separation.[102] The spectrum in **Figure 4-5**C is consistent with a CTP that dominates the dimer spectrum at shorter inter-particle separations. As the dimer is heated and the AuNP monomers begin to separate, the quantum CTP is suppressed and a classically predicted dimer spectrum is established, with a dimer separation of >0.5 nm. Further heating leads to a full rupture into monomers. By following the dynamics of spectral changes during dimer melting, we are able to distinguish between the classical regime and the quantum CTP, which are characterized by similar spectral signatures.

## 4.3 CONCLUSION

We have demonstrated the ability to use an optical tweezer coupled with a darkfield spectrometer to isolate individual AuNP dimers and to determine the inter-particle separation. Our approach allows for 3D manipulation of the dimer structure, including rotation of the long axis relative to illumination polarization. By applying a plasmon ruler equation to spectroscopic measurements of the plasmon scattering spectra of nanoparticle dimer, we are able to resolve sub-nanometer changes in dimer separation. Statistically significant measurements on many dimers in solution show a variation in separation lengths achieved by using distinct polymer tethers. Importantly, we show that we can separate a dimer into its constituent monomers by increasing trapping laser power past a molecule-dependent threshold. By collecting spectra simultaneously as we increase laser power, we observe dimer separation in real time and can correlate it to the plasmon response. These measurements allow us to distinguish between the classical LSPR shifts due to inter-particle distance increase and the quantum CTP regime which occurs at the shortest separations. Critically, the spectral signature of the CTP is similar to the classical response of a dimer with a large inter-particle distance. Our unique OT-based spectrometer allows unprecedented insight into dimer dynamics not observed until now.

This ability to controllably manipulate inter-particle separations and study spectral signatures of distinct structures opens up vast possibilities for research in nanophotonics, nanoelectronics, and biosensing. For instance, understanding and controlling the interaction dynamics between nanoparticles in dimers can lead to the development of sensors and SERS substrates for detecting biological molecules or recognizing changes in environmental conditions at the nanoscale. Furthermore, this approach contributes to the broader field of quantum plasmonics by providing a quantitative tool for exploring the effects of nanoparticle arrangement and environment on their optical properties.

# JOURNAL ABBREVIATIONS

| | |
|---|---|
| Advanced Materials | Adv. Mater. |
| Analytical Chemistry | Anal. Chem. |
| Analytical Chemistry | Anal. Chem. |
| Annual Review of Biophysics | Annu. Rev. Biophys |
| Annual Review of Biophysics & Biomolecular Structure | Annu. Rev. Biophys. Biomol. Struct. |
| Applied Physics Letters | Appl. Phys. Lett. |
| Applied Spectroscopy | Appl. Spectrosc. |
| Arabian Journal of Chemistry | Arab. J. Chem |
| Biophysical Journal | Biophys. J |
| Chemical Communications | Chem. Commun. |
| Chemical Physics Letters | Chem. Phys. Lett. |
| Chemical Science | Chem. Sci. |
| Chemical Society Reviews | Chem. Soc. Rev. |
| ChemRXiv Nanoscience | ChemRxiv Nanosci. |
| Computer Physics Communications | Comput. Phys. Commun. |
| European Physical Journal Plus | Eur. Phys. J. Plus |
| Journal of Chemical Physics | J. Chem. Phys. |

| | |
|---|---|
| Journal of Colloid Interface Science | J. Colloid Interface Sci. |
| Journal of Material Chemistry C | J. Mater. Chem. C |
| Journal of Modern Optics | J. Mod. Opt. |
| Journal of Nanomaterials | J. Nanomat. |
| Journal of Physical Chemistry A | J. Phys. Chem. A |
| Journal of Physical Chemistry C | J. Phys. Chem. C |
| Journal of Physical Chemistry Letters | J. Phys. Chem. Lett. |
| Journal of Physics B: Atomic, Molecular and Optical Physics | J. Phys. B At. Mol. Opt. Phys. |
| Letters to Nature | Lett. to Nat. |
| Light: Science and Applications | Light Sci. Appl. |
| Materials Today Nano | Mater. Today Nano |
| Microscope Research and Technique | Microsc. Res. Tech. |
| Nano Letters | Nano Lett. |
| Nature Chemistry | Nat. Chem. |
| Nature Communications | Nat. Commun. |
| Nature Methods | Nat Methods |
| Nature Reviews Methods Primers | Nat. Rev. Methods Prim. |
| Optics & Laser Technologies | Opt. Laser Technol. |

| | |
|---|---|
| Optics Express | Opt. Express |
| Optics Letters | Opt. Lett. |
| Physical Chemistry Chemical Physics | Phys. Chem. Chem. Phys. |
| Physical Review A | Phys. Rev. A |
| Physical Review Letters | Phys. Rev. Lett |
| Physical Reviews E | Phys. Rev. E |
| Proceedings of the National Academy of Sciences | PNAS |
| Review of Scientific Instruments | Rev. Sci. Instrum. |
| Reviews of Modern Physics | Rev. Mod. Phys. |
| RSC Advances | RSC Adv. |
| Scientific Advances | Sci. Adv. |

# REFERENCES

(1) Ashkin, A. Acceleration and Trapping of Particles by Radiation Pressure. *Phys Rev Lett* **1970**, *24* (4), 156–159. https://doi.org/10.1103/PhysRevLett.24.156.

(2) Ashkin, A.; Dziedzic, J. M. Optical Levitation by Radiation Pressure. *Appl Phys Lett* **1971**, *19* (8), 283–285. https://doi.org/10.1063/1.1653919.

(3) Ashkin, A.; Dziedzic, J. M.; Bjorkholm, J. E.; Chu, S. Observation of a Single-Beam Gradient Force Optical Trap for Dielectric Particles. *Opt Lett* **1986**, *11* (5), 288. https://doi.org/10.1364/OL.11.000288.

(4) Ashkin, A.; Dziedzic, J. M.; Yamanet, T. Optical Trapping and Manipulation of Single Cells Using Infrared Laser Beams. *Letters to Nature* **1987**, *330*, 769–771.

(5) Ashkin, A.; Dziedzic, J. Optical Trapping and Manipulation of Viruses and Bacteria. *Science (1979)* **1987**, *235* (4795), 1517–1520. https://doi.org/10.1126/science.3547653.

(6) Svoboda, K.; Block, S. M. Optical Trapping of Metallic Rayleigh Particles. *Opt Lett* **1994**, *19* (13), 930–932. https://doi.org/10.1364/OL.19.000930.

(7) Seol, Y.; Carpenter, A. E.; Perkins, T. T. Gold Nanoparticles: Enhanced Optical Trapping and Sensitivity Coupled with Significant Heating. *Opt Lett* **2006**, *31* (16), 2429–2431. https://doi.org/10.1364/OL.31.002429.

(8) Abbondanzieri, E. A.; Greenleaf, W. J.; Shaevitz, J. W.; Landick, R.; Block, S. M. Direct Observation of Base-Pair Stepping by RNA Polymerase. *Nature* **2005**, *438*, 460–465. https://doi.org/10.1038/nature04268.

(9) Chemla, Y. R. Revealing the Base Pair Stepping Dynamics of Nucleic Acid Motor Proteins with Optical Traps. *Physical Chemistry Chemical Physics* **2010**, *12* (13), 3080. https://doi.org/10.1039/b920234j.

(10) Perkins, T. T. Ångström-Precision Optical Traps and Applications. *Annu Rev Biophys* **2014**, *43* (1), 279–302. https://doi.org/10.1146/annurev-biophys-042910-155223.

(11) Gordon, R. Biosensing with Nanoaperture Optical Tweezers. *Opt Laser Technol* **2019**, *109*, 328–335. https://doi.org/10.1016/j.optlastec.2018.07.019.

(12) Comstock, M. J.; Ha, T.; Chemla, Y. R. Ultrahigh-Resolution Optical Trap with Single-Fluorophore Sensitivity. *Nat Methods* **2011**, *8* (4), 335–340. https://doi.org/10.1038/nmeth.1574.

(13) Svoboda, K.; Schmidt, C. F.; Schnapp, B. J.; Block, S. M. Direct Observation of Kinesin Stepping by Optical Trapping Interferometry. *Nature* **1993**, *365*, 721–727. https://doi.org/10.1038/365721a0.

(14) Ueberholz, B.; Kuhr, S.; Frese, D.; Meschede, D.; Gomer, V. Counting Cold Collisions. *J. Phys. B: At. Mol. Opt. Phys* **2000**, *33*.

(15) Liu, L. R.; Hood, J. D.; Yu, Y.; Zhang, J. T.; Hutzler, N. R.; Rosenband, T.; Ni, K.-K. *Building One Molecule from a Reservoir of Two Atoms*; 2018; Vol. 360.

(16) Black, J. W.; Kamenetska, M.; Ganim, Z. An Optical Tweezers Platform for Single Molecule Force Spectroscopy in Organic Solvents. *Nano Lett* **2017**, *17* (11), 6598–6605. https://doi.org/10.1021/acs.nanolett.7b02413.

(17) Parobek, A.; Black, J. W.; Kamenetska, M.; Ganim, Z. Force-Detected Nanoscale Absorption Spectroscopy in Water at Room Temperature Using an Optical Trap. *Journal of Chemical Physics* **2018**, *148* (14). https://doi.org/Artn 144201 10.1063/1.5017853.

(18) Jones, P. H.; Marago, O. M.; Volpe, G. Crash Course on Optical Tweezers. In *Optical Tweezers: Principles and Applications*; University Printing House: Cambridge, UK, 2015; pp 4–6.

(19) Skelton Spesyvtseva, S. E.; Dholakia, K. Trapping in a Material World. *ACS Photonics* **2016**, *3*, 719–736. https://doi.org/10.1021/acsphotonics.6b00023.

(20) Pfeifer, R. N. C.; Nieminen, T. A.; Heckenberg, N. R.; Rubinsztein-Dunlop, H. Colloquium: Momentum of an Electromagnetic Wave in Dielectric Media. *Rev Mod Phys* **2007**, *79* (4), 1197–1216. https://doi.org/10.1103/RevModPhys.79.1197.

(21) Gordon, J. P. Radiation Forces and Momenta in Dielectric Media. *Phys Rev A (Coll Park)* **1973**, *8* (1), 14–21.

(22) Qiu, Y.; Kuang, C.; Liu, X.; Tang, L. Single-Molecule Surface-Enhanced Raman Spectroscopy. *Sensors* **2022**, *22*, 4889. https://doi.org/10.3390/s22134889.

(23) Simone, G.; Van De Donk, O. Short Chain Thiols Induce Better Plasmon Resonance Sensitivity in Au(111). *J Mater Chem C Mater* **2019**, *7* (44), 13803–13810. https://doi.org/10.1039/c9tc04030g.

(24) Zeng, S.; Baillargeat, D.; Ho, H. P.; Yong, K. T. Nanomaterials Enhanced Surface Plasmon Resonance for Biological and Chemical Sensing Applications. *Chem Soc Rev* **2014**, *43* (10), 3426–3452. https://doi.org/10.1039/c3cs60479a.

(25) Zuloaga, J.; Prodan, E.; Nordlander, P. Quantum Description of the Plasmon Resonances of a Nanoparticle Dimer. *Nano Lett* **2009**, *9* (2), 887–891. https://doi.org/10.1021/NL803811G/SUPPL_FILE/NL803811G_SI_001.PDF.

(26) Fan, X.; Zheng, W.; Singh, D. J. Light Scattering and Surface Plasmons on Small Spherical Particles. *Light Sci Appl* **2014**, *3* (6), e179–e179. https://doi.org/10.1038/lsa.2014.60.

(27) Chen, T.; Pourmand, M.; Feizpour, A.; Cushman, B.; Reinhard, B. M. Tailoring Plasmon Coupling in Self-Assembled One-Dimensional Au Nanoparticle Chains through Simultaneous Control of Size and Gap Separation. *Journal of Physical Chemistry Letters* **2013**, *4* (13), 2147–2152.

https://doi.org/10.1021/JZ401066G/SUPPL_FILE/JZ401066G_SI_001.PDF.

(28) Pazos-Perez, N.; Guerrini, L.; Alvarez-Puebla, R. A. Plasmon Tunability of Gold Nanostars at the Tip Apexes. *ACS Omega* **2018**, *3* (12), 17173–17179. https://doi.org/10.1021/ACSOMEGA.8B02686/SUPPL_FILE/AO8B02686_SI_001.PDF.

(29) Christopher, P.; Xin, H.; Linic, S. Visible-Light-Enhanced Catalytic Oxidation Reactions on Plasmonic Silver Nanostructures. *Nat Chem* **2011**, *3*, 467–472. https://doi.org/10.1038/NCHEM.1032.

(30) Tian, T.; Xu, J.; Abdolazizi, A.; Ji, C.; Hou, J.; Riley, D. J.; Yan, C.; Ryan, M. P.; Xie, F.; Petit, C. A Monolithic Gold Nanoparticle@metal-Organic Framework Composite as CO2 Photoreduction Catalyst. *Mater Today Nano* **2023**, *21*, 100293. https://doi.org/10.1016/J.MTNANO.2022.100293.

(31) Zheng, G.; De Marchi, S.; López-Puente, V.; Sentosun, K.; Polavarapu, L.; Pérez-Juste, I.; Hill, E. H.; Bals, S.; Liz-Marzán, L. M.; Pastoriza-Santos, I.; Pérez-Juste, J. Encapsulation of Single Plasmonic Nanoparticles within ZIF-8 and SERS Analysis of the MOF Flexibility. *Small* **2016**, *12* (9), 3935–3943. https://doi.org/10.1002/smll.201600947.

(32) Chen, Q. Q.; Hou, R. N.; Zhu, Y. Z.; Wang, X. T.; Zhang, H.; Zhang, Y. J.; Zhang, L.; Tian, Z. Q.; Li, J. F. Au@ZIF-8 Core-Shell Nanoparticles as a SERS Substrate for Volatile Organic Compound Gas Detection. *Anal Chem* **2021**, *93* (19), 7188–7195.

https://doi.org/10.1021/ACS.ANALCHEM.0C05432/ASSET/IMAGES/LARGE/AC0C05432_0007.JPEG.

(33) Kabb, C. P.; Carmean, R. N.; Sumerlin, B. S. Probing the Surface-Localized Hyperthermia of Gold Nanoparticles in a Microwave Field Using Polymeric Thermometers. *Chem Sci* **2015**, *6* (10), 5662–5669. https://doi.org/10.1039/C5SC01535A.

(34) Setoura, K.; Werner, D.; Hashimoto, S. Optical Scattering Spectral Thermometry and Refractometry of a Single Gold Nanoparticle under CW Laser Excitation. *Journal of Physical Chemistry C* **2012**, *116* (29), 15458–15466. https://doi.org/10.1021/jp304271d.

(35) Hosseini Jebeli, S. A.; West, C. A.; Lee, S. A.; Goldwyn, H. J.; Bilchak, C. R.; Fakhraai, Z.; Willets, K. A.; Link, S.; Masiello, D. J. Wavelength-Dependent Photothermal Imaging Probes Nanoscale Temperature Differences among Subdiffraction Coupled Plasmonic Nanorods. *Nano Lett* **2021**, *21* (12), 5386–5393. https://doi.org/10.1021/ACS.NANOLETT.1C01740/ASSET/IMAGES/LARGE/NL1C01740_0005.JPEG.

(36) Jollans, T.; Orrit, M. Explosive, Oscillatory, and Leidenfrost Boiling at the Nanoscale. *Phys Rev E* **2019**, *99* (6), 063110. https://doi.org/10.1103/PhysRevE.99.063110.

(37) Ni, W.; Ba, H.; Lutich, A. A.; Jäckel, F.; Feldmann, J. Enhancing Single-Nanoparticle Surface-Chemistry by Plasmonic Overheating in an Optical Trap. *Nano Lett* **2012**, *12* (9), 4647–4650. https://doi.org/10.1021/nl301937j.

(38) Merabia, S.; Keblinski, P.; Joly, L.; Lewis, L. J.; Barrat, J.-L. Critical Heat Flux around Strongly Heated Nanoparticles. *Phys Rev E* **2009**, *79*, 021404. https://doi.org/10.1103/PhysRevE.79.021404.

(39) Jones, P. H.; Maragò, O. M.; Volpe, G. Spectroscopy. In *Optical Tweezers: Principles and Applications*; Cambridge University Press: Cambridge UK, 2015; pp 395–405.

(40) Neuman, K. C.; Nagy, A. Single-Molecule Force Spectroscopy: Optical Tweezers, Magnetic Tweezers and Atomic Force Microscopy. *Nat Methods* **2008**, *5* (6), 491–505. https://doi.org/10.1038/nmeth.1218.

(41) Neuman, K. C.; Block, S. M. Optical Trapping. *Review of Scientific Instruments* **2004**, *75* (9), 2787–2809. https://doi.org/10.1063/1.1785844.

(42) Ueno, H.; Nishikawa, S.; Iino, R.; Tabata, K. V.; Sakakihara, S.; Yanagida, T.; Noji, H. Simple Dark-Field Microscopy with Nanometer Spatial Precision and Microsecond Temporal Resolution. *Biophys J* **2010**. https://doi.org/10.1016/j.bpj.2010.01.011.

(43) Prikulis, J.; Svedberg, F.; Ka, M.; Enger, J.; Ramser, K.; Gokso, M.; Hanstorp, D. Optical Spectroscopy of Single Trapped Metal Nanoparticles in Solution. *Nano Lett* **2004**, *4* (1), 115–118. https://doi.org/10.1021/nl0349606.

(44) Mukamel, S. *Principles of Nonlinear Optical Spectroscopy*; Lapp, M., Nishizawa, J., Snavely, B. B., Stark, H., Tam, A. C., Wilson, T., Eds.; Oxford University Press: New York, NY, 1995.

(45) Thurn, R.; Kiefer, W. Raman-Microsampling Technique Applying Optical Levitation by Radiation Pressure. *Appl Spectrosc* **1984**, *38* (1).

(46) Ajito, K.; Torimitsu, K. Laser Trapping and Raman Spectroscopy of Single Cellular Organelles in the Nanometer Range. In *Lab on a Chip*; Royal Society of Chemistry, 2002; Vol. 2, pp 11–14. https://doi.org/10.1039/b108744b.

(47) C., G.; Shetty, S.; Bharati, S.; Chidangil, S.; Bankapur, A. Optical Trapping and Micro-Raman Spectroscopy of Functional Red Blood Cells Using Vortex Beam for Cell Membrane Studies. *Anal Chem* **2021**, *93* (13), 5484–5493. https://doi.org/10.1021/ACS.ANALCHEM.0C05204.

(48) Parlatan, U.; Başar, G.; Başar, G. Sorting of Micron-Sized Particles Using Holographic Optical Raman Tweezers in Aqueous Medium. *J Mod Opt* **2019**, *66* (2), 228–234. https://doi.org/10.1080/09500340.2018.1515378.

(49) Gillibert, R.; Magazzù, A.; Callegari, A.; Bronte-Ciriza, D.; Foti, A.; Grazia Donato, M.; Maragò, O. M.; Volpe, G.; Lamy de La Chapelle, M.; Lagarde, F.; Gucciardi, P. G. Raman Tweezers for Tire and Road Wear Micro-and Nanoparticles Analysis. *Chem Rxiv Nanoscience* **2021**.

(50) Penders, J.; Pence, I. J.; Horgan, C. C.; Bergholt, M. S.; Wood, C. S.; Najer, A.; Kauscher, U.; Nagelkerke, A.; Stevens, M. M. Single Particle Automated

Raman Trapping Analysis. *Nat Commun* **2018**, *9*, 4256. https://doi.org/10.1038/s41467-018-06397-6.

(51) Mrad, R.; Kruglik, S. G.; Brahim, N. Ben; Chaâ, R. Ben; Negrerie, M. Raman Tweezers Microspectroscopy of Functionalized 4.2 Nm Diameter CdSe Nanocrystals in Water Reveals Changed Ligand Vibrational Modes by a Metal Cation. *J. Phys. Chem. C* **2019**, *123*, 24912–24918. https://doi.org/10.1021/acs.jpcc.9b06756.

(52) Tamma, V. A.; Beecher, L. M.; Shumaker-Parry, J. S.; WIckramasinghe, H. K. Detecting Stimulated Raman Responses of Molecules in Plasmonic Gap Using Photon Induced Forces. *Opt Express* **2018**, *26* (24), 31439–31453.

(53) Dai, X.; Fu, W.; Chi, H.; Mesias, V. S. D.; Zhu, H.; Leung, C. W.; Liu, W.; Huang, J. Optical Tweezers-Controlled Hotspot for Sensitive and Reproducible Surface-Enhanced Raman Spectroscopy Characterization of Native Protein Structures. *Nat Commun* **2021**, *12* (1), 1292. https://doi.org/10.1038/s41467-021-21543-3.

(54) Jackson, D. J.; Dawes, B. A.; Kamenetska, M. Simultaneous Force and Darkfield Measurements Reveal Solvent-Dependent Axial Control of Optically Trapped Gold Nanoparticles. *J. Phys. Chem. Lett* **2023**, *14* (11), 2830–2836. https://doi.org/10.1021/acs.jpclett.3c00088.

(55) Jackson, D.; Rose, M.; Kamenetska, M. Tunable Growth of a Single High-Density ZIF Nanoshell on a Gold Nanoparticle Isolated in an Optical Trap. *Nanoscale* **2024**. https://doi.org/10.1039/d3nr05316d.

(56) Bustamante, C. J.; Chemla, Y. R.; Liu, S.; Wang, M. D. Optical Tweezers in Single-Molecule Biophysics. *Nature Reviews Methods Primers* **2021**, *1*, 25. https://doi.org/10.1038/s43586-021-00021-6.

(57) Zaltron, A.; Merano, M.; Mistura, G.; Sada, C.; Seno, F. Optical Tweezers in Single-Molecule Experiments. *Eur. Phys. J. Plus* **2020**, *135*, 896. https://doi.org/10.1140/epjp/s13360-020-00907-6.

(58) Yu, Q.; Chen, Y.-N.; Black, J. W.; Ganim, Z. Zinc Oxide @ Silica Core/Shell Microspheres for Single-Molecule Force Microscopy in Aqueous and Non-Aqueous Solvents. *The Journal of Physical Chemistry C* **2020**, *124*, 5789–5795. https://doi.org/10.1021/acs.jpcc.9b11923.

(59) Yusof, M. F. M.; Ayop, S. K.; Supian, F. L.; Juahir, Y. Optical Trapping of Organic Solvents in the Form of Microdroplets in Water. *Chem Phys Lett* **2020**, *749*, 137407. https://doi.org/10.1016/j.cplett.2020.137407.

(60) Nowak, D.; Morrison, W.; Kumar Wickramasinghe, H.; Jahng, J.; Potma, E.; Wan, L.; Ruiz, R.; Albrecht, T. R.; Schmidt, K.; Frommer, J.; Sanders, D. P.; Park, S. Nanoscale Chemical Imaging by Photoinduced Force Microscopy. *Scientific Advances* **2016**, *2*, e1501571. https://doi.org/10.1126/sciadv.1501571.

(61) O'callahan, B. T.; Yan, J.; Menges, F.; Muller, E. A.; Raschke, M. B. Photoinduced Tip−Sample Forces for Chemical Nanoimaging and Spectroscopy. *Nano Lett* **2018**, 5499–5505. https://doi.org/10.1021/acs.nanolett.8b01899.

(62) Parobek, A.; Black, J. W.; Kamenetska, M.; Ganim, Z. Force-Detected Nanoscale Absorption Spectroscopy in Water at Room Temperature Using an Optical Trap. *Journal of Chemical Physics* **2018**, *148* (14). https://doi.org/Artn 144201 10.1063/1.5017853.

(63) Urban, A. S.; Carretero-Palacios, S.; Lutich, A. A.; Lohmüller, T.; Feldmann, J.; Jäckel, F. Optical Trapping and Manipulation of Plasmonic Nanoparticles: Fundamentals, Applications, and Perspectives. *Nanoscale* **2014**, *6* (9), 4458. https://doi.org/10.1039/c3nr06617g.

(64) Hansen, P. M.; Bhatia, V. K.; Harrit, N.; Oddershede, L. Expanding the Optical Trapping Range of Gold Nanoparticles. *Nano Lett* **2005**, *5* (10), 1937–1942. https://doi.org/10.1021/nl051289r.

(65) Dienerowitz, M.; Mazilu, M.; Dholakia, K. Optical Manipulation of Nanoparticles: A Review. *J Nanophotonics* **2008**, *2* (1), 021875. https://doi.org/10.1117/1.2992045.

(66) Rajapaksa, I.; Uenal, K.; Wickramasinghe, H. K. Image Force Microscopy of Molecular Resonance: A Microscope Principle. *Appl Phys Lett* **2010**. https://doi.org/10.1063/1.3480608.

(67) Jahng, J.; Fishman, D. A.; Park, S.; Nowak, D. B.; Morrison, W. A.; Kumar Wickramasinghe, ǁ H; Potma, E. O. Linear and Nonlinear Optical Spectroscopy at the Nanoscale with Photoinduced Force Microscopy. **2015**. https://doi.org/10.1021/acs.accounts.5b00327.

(68) Pearce, K.; Wang, F.; Reece, P. J. Dark-Field Optical Tweezers for Nanometrology of Metallic Nanoparticles. *Opt Express* **2011**, *19* (25), 25559–25569. https://doi.org/10.1557/mrs2005.100.

(69) Tolić-Nørrelykke, S. F.; Schäffer, E.; Howard, J.; Pavone, F. S.; Jülicher, F.; Flyvbjerg, H. Calibration of Optical Tweezers with Positional Detection in the Back Focal Plane. *Review of Scientific Instruments* **2006**, *77* (10). https://doi.org/10.1063/1.2356852.

(70) Lee, Y. J.; Schade, N. B.; Sun, L.; Fan, J. A.; Bae, D. R.; Mariscal, M. M.; Lee, G.; Capasso, F.; Sacanna, S.; Manoharan, V. N.; Yi, G. R. Ultrasmooth, Highly Spherical Monocrystalline Gold Particles for Precision Plasmonics. *ACS Nano* **2013**, *7* (12), 11064–11070. https://doi.org/10.1021/nn404765w.

(71) Tcherniak, A.; Dominguez-Medina, S.; Chang, W. S.; Swanglap, P.; Slaughter, L. S.; Landes, C. F.; Link, S. One-Photon Plasmon Luminescence and Its Application to Correlation Spectroscopy as a Probe for Rotational and Translational Dynamics of Gold Nanorods. *Journal of Physical Chemistry C* **2011**, *115* (32), 15938–15949. https://doi.org/10.1021/JP206203S/SUPPL_FILE/JP206203S_SI_001.PDF.

(72) Nugent-Glandorf, L.; Perkins, T. T. Measuring 0.1-Nm Motion in 1 Ms in an Optical Microscope with Differential Back-Focal-Plane Detection. *Opt Lett* **2004**, *29* (22), 2611–2613.

(73) Pesce, G.; Jones, P. H.; Maragò, O. M.; Volpe, G. Optical Tweezers: Theory and Practice. *The European Physical Journal Plus* **2020**, *135*, 949. https://doi.org/10.1140/EPJP/S13360-020-00843-5.

(74) Bass, M.; Kar, A. Laser–Materials Interactions. In *Encyclopedia of Physical Science and Technology*; Academic Press, 2003; pp 247–265. https://doi.org/10.1016/B0-12-227410-5/00361-6.

(75) Pralle, A.; Prummer, M.; Florin, E.-L.; Stelzer, E. H. K.; Horber, J. K. H. Three-Dimensional High-Resolution Particle Tracking for Optical Tweezers by Forward Scattered Light. *Microsc Res Tech* **1999**, *386* (November 1998), 378–386.

(76) Svoboda, K.; Block, S. M. Biological Application of Optical Forces. *Annu. Rev. Biophys. Biomol. Struct.* **1994**, *23*, 247–285.

(77) Jones, P. H.; Maragò, O. M.; Volpe, G. *Optical Tweezers: Principles and Applications*; Cambridge University Press, 2015.

(78) Jones, P. H.; Maragò, O. M.; Volpe, G. *Optical Tweezers: Principles and Applications*; Cambridge University Press, 2015.

(79) Lee, Y.-J.; Schade, N. B.; Sun, L.; Fan, J. A.; Bae, D. R.; Mariscal, M. M.; Lee, G.; Capasso, F.; Sacanna, S.; Manoharan, V. N.; Yi, G.-R. Ultrasmooth, Highly Spherical Monocrystalline Gold Particles for Precision Plasmonics. *ACS Nano* **2013**, *7* (12), 11064–11070. https://doi.org/10.1021/nn404765w.

(80) Nanopartz. *Gold nanoparticles for nanotechnology*. https://www.nanopartz.com/.

(81) Park, K. S.; Ni, Z.; Cô, A. P.; Choi, J. Y.; Huang, R.; Uribe-Romo, F. J.; Chae, H. K.; O'keeffe, M.; Yaghi, O. M. Exceptional Chemical and Thermal Stability of Zeolitic Imidazolate Frameworks. *PNAS* **2006**, *103* (27), 10186–10191. https://doi.org/https://doi.org/10.1073/pnas.0602439103.

(82) Khan, I. U.; Othman, M. H. D.; Jilani, A.; Ismail, A. F.; Hashim, H.; Jaafar, J.; Rahman, M. A.; Rehman, G. U. Economical, Environmental Friendly Synthesis, Characterization for the Production of Zeolitic Imidazolate Framework-8 (ZIF-8) Nanoparticles with Enhanced CO2 Adsorption. *Arabian Journal of Chemistry* **2018**, *11* (7), 1072–1083. https://doi.org/10.1016/J.ARABJC.2018.07.012.

(83) Kumari, G.; Jayaramulu, K.; Maji, T. K.; Narayana, C. Temperature Induced Structural Transformations and Gas Adsorption in the Zeolitic Imidazolate Framework ZIF-8: A Raman Study. *Journal of Physical Chemistry A* **2013**, *117* (43), 11006–11012. https://doi.org/https://doi.org/10.1021/jp407792a.

(84) Gugin, N.; Jose Villajos, A.; Feldmann, I.; Emmerling, F. Mix and Wait – a Relaxed Way for Synthesizing ZIF-8. *RSC Adv* **2022**, *12*, 8940–8944. https://doi.org/10.1039/d2ra00740a.

(85) Hohenester, U.; Trügler, A. MNPBEM – A Matlab Toolbox for the Simulation of Plasmonic Nanoparticles. *Comput Phys Commun* **2012**, *183* (2), 370–381. https://doi.org/10.1016/J.CPC.2011.09.009.

(86) Chen, L.; Peng, Y.; Wang, H.; Gu, Z.; Duan, C. Synthesis of Au@ZIF-8 Single- or Multi-Core–Shell Structures for Photocatalysis. *Chemical*

*Communications* **2014**, *50* (63), 8651–8654. https://doi.org/10.1039/C4CC02818J.

(87) Khan, I. U.; Othman, M. H. D.; Jilani, A.; Ismail, A. F.; Hashim, H.; Jaafar, J.; Rahman, M. A.; Rehman, G. U. Economical, Environmental Friendly Synthesis, Characterization for the Production of Zeolitic Imidazolate Framework-8 (ZIF-8) Nanoparticles with Enhanced CO2 Adsorption. *Arabian Journal of Chemistry* **2018**, *11* (7), 1072–1083. https://doi.org/10.1016/J.ARABJC.2018.07.012.

(88) Huang, D.; Byers, C. P.; Wang, L. Y.; Hoggard, A.; Hoener, B.; Dominguez-Medina, S.; Chen, S.; Chang, W. S.; Landes, C. F.; Link, S. Photoluminescence of a Plasmonic Molecule. *ACS Nano* **2015**, *9* (7), 7072–7079. https://doi.org/10.1021/ACSNANO.5B01634/SUPPL_FILE/NN5B01634_SI_001.PDF.

(89) Kermani, H.; Rohrbach, A. Orientation-Control of Two Plasmonically Coupled Nanoparticles in an Optical Trap. *ACS Photonics* **2018**, *5* (11), 4660–4667. https://doi.org/10.1021/acsphotonics.8b01145.

(90) Blattmann, M.; Rohrbach, A. Plasmonic Coupling Dynamics of Silver Nanoparticles in an Optical Trap. *Nano Lett* **2015**, *15*, 7816–7821. https://doi.org/10.1021/acs.nanolett.5b02532.

(91) Pelton, M.; Liu, M.; Kim, H. Y.; Smith, G.; Guyot-Sionnest, P.; Scherer, N. F. Optical Trapping and Alignment of Single Gold Nanorods by Using

Plasmon Resonances. *Opt Lett* **2006**, *31* (13), 2075–2077. https://doi.org/10.1364/OL.31.002075.

(92) McMahon, J. M.; Henry, A. I.; Wustholz, K. L.; Natan, M. J.; Freeman, R. G.; Van Duyne, R. P.; Schatz, G. C. Gold Nanoparticle Dimer Plasmonics: Finite Element Method Calculations of the Electromagnetic Enhancement to Surface-Enhanced Raman Spectroscopy. *Anal Bioanal Chem* **2009**, *394* (7), 1819–1825. https://doi.org/10.1007/s00216-009-2738-4.

(93) Teperik, T. V.; Nordlander, P.; Aizpurua, J.; Borisov, A. G. Quantum Effects and Nonlocality in Strongly Coupled Plasmonic Nanowire Dimers. *Opt Express* **2013**, *21* (22), 27306. https://doi.org/10.1364/OE.21.027306.

(94) Sönnichsen, C.; Reinhard, B. M.; Liphardt, J.; Alivisatos, A. P. A Molecular Ruler Based on Plasmon Coupling of Single Gold and Silver Nanoparticles. *Nat Biotechnol* **2005**, *23* (6), 741–745. https://doi.org/10.1038/nbt1100.

(95) Chen, T.; Pourmand, M.; Feizpour, A.; Cushman, B.; Reinhard, B. M. Tailoring Plasmon Coupling in Self-Assembled One-Dimensional Au Nanoparticle Chains through Simultaneous Control of Size and Gap Separation. *Journal of Physical Chemistry Letters* **2013**, *4* (13), 2147–2152. https://doi.org/10.1021/JZ401066G/SUPPL_FILE/JZ401066G_SI_001.PDF.

(96) Reinhard, B. M.; Siu, M.; Agarwal, H.; Alivisatos, A. P.; Liphardt, J. Calibration of Dynamic Molecular Rulers Based on Plasmon Coupling

between Gold Nanoparticles. *Nano Lett* **2005**, *5* (11), 2246–2252. https://doi.org/10.1021/nl051592s.

(97) Reinhard, B. M.; Sheikholeslami, S.; Mastroianni, A.; Alivisatos, A. P.; Liphardt, J. Use of Plasmon Coupling to Reveal the Dynamics of DNA Bending and Cleavage by Single EcoRV Restriction Enzymes. *Proc Natl Acad Sci U S A* **2007**, *104* (8), 2667–2672. https://doi.org/10.1073/pnas.0607826104.

(98) Hohenester, U.; Trügler, A. MNPBEM – A Matlab Toolbox for the Simulation of Plasmonic Nanoparticles. *Comput Phys Commun* **2012**, *183* (2), 370–381. https://doi.org/10.1016/J.CPC.2011.09.009.

(99) Lerch, S.; Reinhard, B. M. Quantum Plasmonics: Optical Monitoring of DNA-Mediated Charge Transfer in Plasmon Rulers. *Advanced Materials* **2016**, *28* (10), 2030–2036. https://doi.org/10.1002/adma.201503885.

(100) Jain, P. K.; Huang, W.; El-Sayed, M. A. On the Universal Scaling Behavior of the Distance Decay of Plasmon Coupling in Metal Nanoparticle Pairs: A Plasmon Ruler Equation. *Nano Lett* **2007**, *7* (7), 2080–2088. https://doi.org/10.1021/nl071008a.

(101) Romero, I.; Aizpurua, J.; Bryant, G. W.; García De Abajo, F. J. Plasmons in Nearly Touching Metallic Nanoparticles: Singular Response in the Limit of Touching Dimers. *Opt Express* **2006**, *14* (21), 9988. https://doi.org/10.1364/oe.14.009988.

(102) Cha, H.; Lee, D.; Yoon, J. H.; Yoon, S. Plasmon Coupling between Silver Nanoparticles: Transition from the Classical to the Quantum Regime. *J Colloid Interface Sci* **2016**, *464*, 18–24. https://doi.org/10.1016/J.JCIS.2015.11.009.

(103) Yoon, J. H.; Selbach, F.; Schumacher, L.; Jose, J.; Schlücker, S. Surface Plasmon Coupling in Dimers of Gold Nanoparticles: Experiment and Theory for Ideal (Spherical) and Nonideal (Faceted) Building Blocks. *ACS Photonics* **2019**, *6* (3), 642–648. https://doi.org/10.1021/acsphotonics.8b01424.

(104) Lerch, S.; Reinhard, B. M. Quantum Plasmonics: Optical Monitoring of DNA-Mediated Charge Transfer in Plasmon Rulers. *Advanced Materials* **2016**, *28* (10), 2030–2036. https://doi.org/10.1002/adma.201503885.

(105) Stiufiuc, R.; Iacovita, C.; Nicoara, R.; Stiufiuc, G.; Florea, A.; Achim, M.; Lucaciu, C. M. One-Step Synthesis of PEGylated Gold Nanoparticles with Tunable Surface Charge. *J Nanomater* **2013**, *2013*. https://doi.org/10.1155/2013/146031.

(106) Cirri, A.; Silakov, A.; Jensen, L.; Lear, B. J. Chain Length and Solvent Control over the Electronic Properties of Alkanethiolate-Protected Gold Nanoparticles at the Molecule-to-Metal Transition. *J Am Chem Soc* **2016**, *138* (49), 15987–15993. https://doi.org/10.1021/jacs.6b09586.

# CURRICULUM VITAE

## Education

*PhD in Physical Chemistry | Boston University, Boston, MA, USA | Completion May 15, 2024*

- *Thesis*: "Advancements in Optical Trapping and Spectroscopic Analysis of Gold Nanoparticle Composites in Organic Environments"
- *Advisor*: Maria Kamenetska | Assistant Professor of Chemistry, Physics, and Material Science and Engineering
- *Coursework*: Statistical Mechanics, Quantum Mechanics, Molecular Quantum Chemistry, Nanomaterials and Optical Characterization, Nanostructure Optics, Principles of Linear and Nonlinear Spectroscopy

*B.S. in Chemistry | Union College, Schenectady, NY, USA | Graduated June 2017*

- *Advisors*: Joanne D. Kehlbeck and Michael E. Hagerman
- *Coursework*: Completed rigorous coursework covering General Chemistry, Organic Chemistry, Inorganic Chemistry, Nanoscience, Analytical Chemistry, Biochemistry, and Physical Chemistry.

## Honors and Awards

*BUNano Fellowship | Boston University, Boston, MA | Sept. 2018 – Aug. 2019*

- Engaged in cutting-edge, cross-disciplinary research under the guidance of leading nanoscience and nanotechnology experts, focusing on the development and application of nanoscale materials for innovative solutions in physical chemistry.
- Mentored high school students through CITYLabs outreach program, inspiring and cultivating their interest in STEM fields by simplifying complex scientific concepts and demonstrating practical applications of nanotechnology.

*Edward R. Kane (1940) Endowed Chemistry Fund | Union College, Schenectady, NY | Summer 2015 & 2016*

- Enabled continued focused research of renewable energy materials during the academic off-season expanding upon in-semester research.

## Research Experience

*Kamenetska Lab | Boston University Chemistry, Boston, MA | Sept. 2017 – May 2024*

- Research Overview: Developed an innovative technique for optical trapping of gold nanoparticles in organic solvents. Spearheaded the construction and improvement of high-precision optical trapping instrument. Key successes include the optical trapping of gold nanoparticles in high-refractive-index solvents, detailed analysis of solvent-dependent trapping dynamics, and the novel application of nanoparticle heating to drive the tunable growth of crystalline nanoshells.

- *Programming Languages*: Advanced experience with scientific software including ***LabVIEW*** for equipment control, ***SolidWorks*** for mechanical design, ***IGOR Pro*** and ***MATLAB*** for data analysis, Princeton Instruments ***Lightfield*** software for control of spectrometer, ***Blender*** to generate animations to present scientific concepts, and ***LaTeX*** for document preparation. High level of experience using all ***Microsoft programs*** (e.g. Office, PowerPoint, Outlook).
- *Specific Instrumentation*: Optical tweezer, NMR, fluorimeter, UV-vis spectrometer, Raman spectrometer, SEM, FT-IR, AFM, and LUMICKS C-trap.

*Kehlbeck and Hagerman Labs | Union College, Schenectady, NY | Sept. 2014 – June 2017*

- *Research Overview*: Conducted extensive research on the synthesis of inorganic quantum dots and custom organic ligands for next-generation solar panel technologies. Gained proficiency in maintaining an oxygen-free environment for high-temperature syntheses in organic solvents.

## Teaching Experience

*Teaching Fellow | Boston University Chemistry, Boston, MA*

- Principles of Organic and Biochemistry Discussion | Jan. 2024 – May 2024
- Principles of General Chemistry Lab | Oct. 2023 – Dec. 2023
- Intensive General Chemistry with Quantitative Analysis Lab | Sept. 2020 – Dec. 2020

- Intensive General Chemistry with Quantitative Analysis Lab | Sept. 2017 – May 2018

*Writing Fellow | Boston University Chemistry, Boston, MA*

- Intensive General Chemistry with Quantitative Analysis | Sept. 2021 – May 2022

*Organic Chemistry Tutor | Union College, Schenectady, NY | Sept. 2014 – June 2017*

## Work Experience

*Chemical Stock Room Attendant | Union College, Schenectady, NY | Sept. 2014 – June 2017*

*Outreach Coordinator Chemistry Club | Union College, Schenectady, NY | Apr. 2014 – Apr. 2016*

## Publications

- **Jackson**, Chung, Kamenetska. Spectroscopically Characterizing Gold Nanoparticle Dimers in an Optical Trap and Determining Nanoparticle Separation by Plasmon Ruler Equation. *In preparation* **2024**.
- **Jackson**, Rose, Kamenetska. Tunable Growth of a Single High-Density ZIF Nanoshell on a Gold Nanoparticle Isolated in an Optical Trap. *Nanoscale* **2024**, 16, 2591 – 2598.

- **Jackson**, Dawes, Kamenetska. Simultaneous Force and Darkfield Measurements Reveal Solvent-Dependent Axial Control of Optically Trapped Gold Nanoparticles. *J. Phys. Chem. Lett.* **2023**, *14*, 2830 – 2836.

## Presentations

*Noble Metal Nanoparticles Gordon Research Conference | Spring 2022 (Poster) | Mt. Holyoke College*

- **Daniel Jackson** and Maria Kamenetska. *Optical Trapping of Gold Nanoparticles in Non-aqueous Environments*.

*American Chemical Society National Meeting | Spring 2022 (Oral) | San Diego, CA*

- **Daniel Jackson** and Maria Kamenetska. *Probing chemical environments with optically trapped plasmonic nanoparticles.*

*American Chemical Society National Meeting | Fall 2021 (Virtual Oral) | Atlanta, GA*

- **Daniel Jackson** and Maria Kamenetska. *Plasmonically enhanced single molecule characterization in organic media using an optical tweezer*.

*Boston University Spectroscopy Seminar | Fall 2019 (Oral) | Boston, MA*

- **Daniel Jackson** and Maria Kamenetska. *Characterizing Single Molecule and Nanoparticle Dynamics by Force Detection in an Optical Tweezer*.

*American Chemical Society National Meeting | Fall 2018 (Oral) | Boston, MA*

- **Daniel Jackson** and Maria Kamenetska. *High-resolution single molecule force spectroscopy using carbon nanotubes in an optical tweezer*.

*American Chemical Society National Meeting | Spring 2017 (Poster) | San Francisco, CA*

- **Daniel J. Jackson**, Michael E. Hagerman, Joanne D. Kehlbeck. *Nanotethering to cadmium selenide for solar applications.*

*American Chemical Society National Meeting | Spring 2016 (Poster) | San Diego, CA*

- Andrew S. Tysoe, Kim A. Bolduc, **Daniel J. Jackson**, Joanne D. Kehlbeck, Michael E. Hagerman. *Exploring amine nanotethers: New routes to functionalized CdSe nanoparticles*.